Thesis

Safety Considerations for Developing an H2ICE for Aviation Applications

Lina Hosking

Technische Universiteit Delft

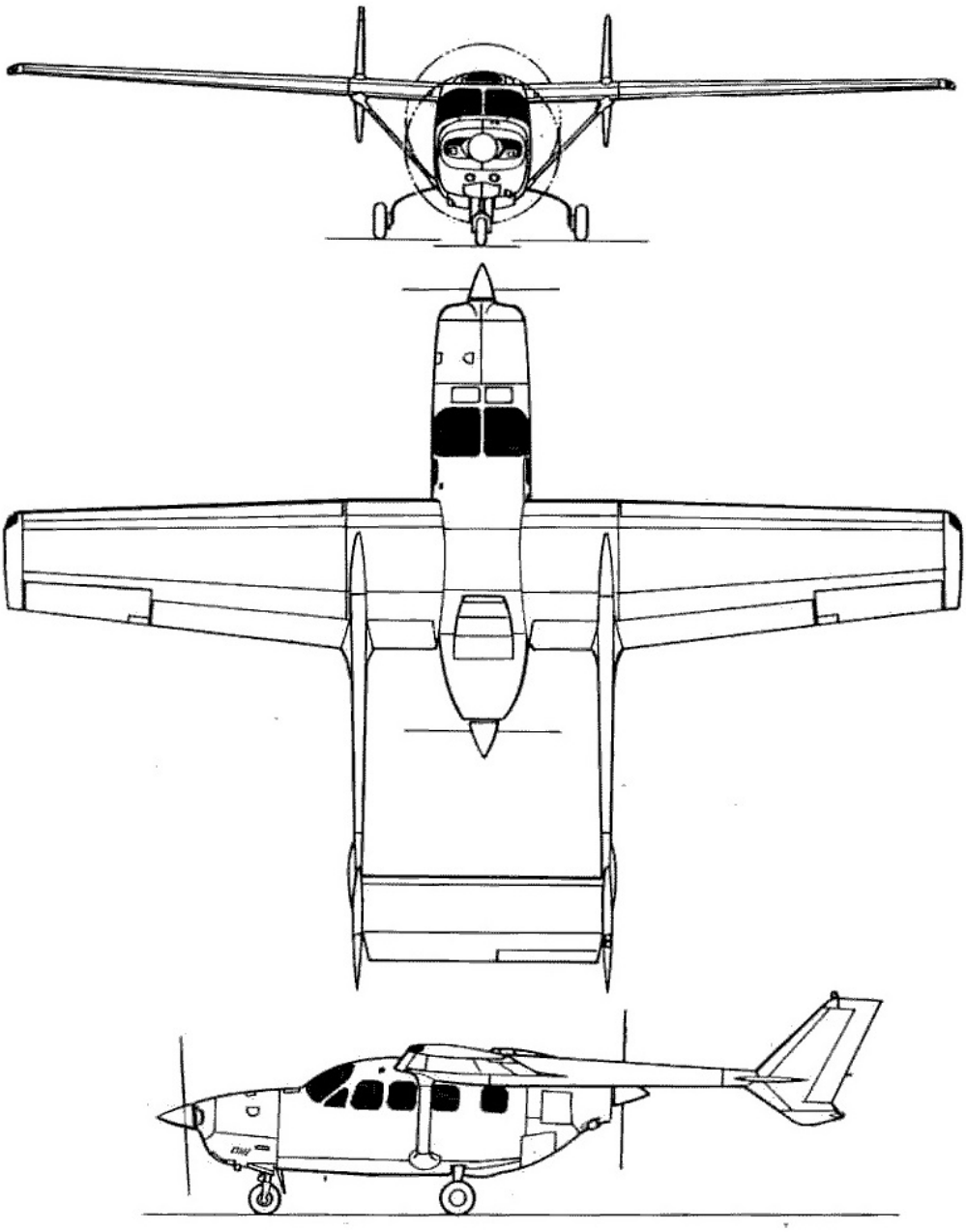

TU Delft Delft University of Technology

Challenge the future

THESIS

SAFETY CONSIDERATIONS FOR DEVELOPING AN H2ICE FOR AVIATION APPLICATIONS

by

Lina Hosking

at the Delft University of Technology.

Supervisor:	Ir. J.A. Melkert
	Prof.dr.ir. L.L.M. Veldhuis
Advisors:	V. Klein

Figure on front page from https://drawingdatabase.com/cessna-skymaster/

TU Delft Delft University of Technology

ACKNOWLEDGEMENTS

First and foremost, I would like to express my gratitude to ir. Joris Melkert, Prof.dr.ir Leo Veldhuis and Victor Klein, for providing this learning opportunity, steering the project in the right direction and providing knowledge and guidance where needed.

I would like to thank ir. Michiel Schuurman for his professional advice during some challenging times during this thesis. Furthermore, I am grateful to have gotten acquainted with dr. Dario Lopez Pintor, who has given me great insight into some of the technical challenges.

This thesis could not have been completed without the emotional support of my family, friends and roommates. I am extremely grateful for their sympathetic ear. Additionally, they were also involved in assuring the quality of this work.

CONTENTS

LIST OF SYMBOLS AND ABBREVIATIONS

Symbols

$\bar{S}_p$	Average piston velocity	m/s
$\bar{w}$	Average cylinder gas velocity	m/s
β	Arrhenius rate coefficient β	-
$\dot{\omega}$	Chemical production rate	kg/s
η_v	Profile propeller efficiency	-
γ	Specific heat ratio	-
λ	Gas conductivity	W/(m K)
μ	Viscosity	Pa s
ϕ	Equivalence ratio	-
ρ	Density	kg/m^3
σ	Stoichiometric molar ratio	-
θ	Crank angle	°
A	Area	m^2
a	Heat transfer coefficient a	-
A_a	Arrhenius rate coefficient A	-
$a_{1,2,3,4,5,6,7}$	NASA polynomial coefficients	-
b	Heat transfer coefficient b	-
b_W	Wiebe parameter b	-
c	Heat transfer coefficient c	-
C_D	Drag coefficient	-
C_L	Lift coefficient	-
C_p	Heat capacity at constant pressure	J/(kg K)
C_v	Heat capacity at constant volume	J/(kg K)
C_{11}	Woschni heat transfer coefficient C11	-
C_{12}	Woschni heat transfer coefficient C12	-
C_2	Woschni heat transfer coefficient C2	cm/(s K)
CR	Compression ratio	-
D	Bore	m
d	Height	m
E_a	Activation energy	J/mol
H	Enthalpy	J
h	Specific enthalpy	J/kg
h_c	Conductive heat transfer coefficient	W/(m^2 K)
k_+	Forward rate constant	-
k_-	Reverse rate constant	-
K_c	Equilibrium constant	-
L	Characteristic length	m
L_A	Crank arm radius	m
L_C	Connecting rod length	m
m	Mass	kg
Mm	Molar mass	g/mol
N	Engine speed	RPM
n	Amount of species	mol
n_W	Wiebe parameter n	-
Nu	Nusselt number	-
P	Power	W
p	Pressure	Pa
P_{shaft}	Shaft power	W
Pr	Prandtl number	-

Q	Heat	J
Q_v	Water flow	m^3/h
R	Universal gas constant	J/(mol K)
R_C	Connecting rod to crank arm ratio	-
r_{prop}	Propeller radius	m
Re	Reynolds number	-
S	Entropy	J/K
S_T	Sutherland's temperature	K
T	Temperature	K
T_f	Thrust	N
T_q	Torque	Nm
V	Volume	m^3
v	Velocity	m/s
V_0	Cylinder volume	m^3
V_{clear}	Clearance volume	m^3
v_{swirl}	Swirl velocity	m/s
W	Work	J
W_b	Wiebe function	-
W_{AC}	Weight	N
x_r	Residual gas fraction	-
Y	Species	-

Abbreviations

aBDC	After Bottom Dead Centre
aTDC	After Top Dead Centre
bBDC	Before Bottom Dead Centre
BDC	Bottom Dead Centre
bTDC	Before Top Dead Centre
CHT	Cylinder Head Temperature
DEAC	Dutch Electric Aviation Centre
DI	Direct Injection
ECU	Electronic Control Unit
EGT	Exhaust Gas Temperature
EVC	Exhaust Valve Closed
EVO	Exhaust Valve Open
H2FC	Hydrogen Fuel Cell
H2ICE	Hydrogen Internal Combustion Engine
IMEP	Indicated Mean Effective Pressure
IVC	Inlet Valve Closed
NDIR	Non Dispersive Infrared
PFI	Port Fuel Injection
TDC	Top Dead Centre
TEL	Tetraethyllead
uHC	Unburnt hydrocarbons

Subscripts

0	Reference or start value
b	Burnt zone
$cool$	Cooling flow
cyl	Cylinder
eng	Engine
exh	Exhaust
in	Inflowing mass
j	Timestep
$loss$	Losses
ST	Spark timing
u	Unburnt zone
w	Wall

EXECUTIVE SUMMARY

For the aviation industry to sustain its growth while adhering to the Paris Agreement, the emissions per flight must be reduced. One way to achieve this, is by shifting from fossil fuels to renewable fuels, such as hydrogen. The goal of the project, of which this thesis is a part, is to modify one of the engines of a Cessna Skymaster to operate on hydrogen. As a proof of concept, the modification is first applied to a Lycoming IO-360-A1B6 engine. This thesis focuses on the first steps towards the design and construction of a test set-up, and the analysis of the risk of catastrophic failure of the engine due to an increase in pressure and/or temperature.

When using Avgas, one of the standard fuels used in general aviation, 3.1 kg CO_2 is emitted per kg fuel consumed. In addition, CO, unburnt hydrocarbons, NO_x and lead is emitted. When using hydrogen, H_2O and NO_x is emitted. There are two ways of utilising hydrogen to propel an aircraft: as fuel for a fuel cell combined with an electric motor, or through direct combustion in for example a piston engine. The latter is cheaper, allows for bi-fuel operation, and is regarded an important link in the transition towards a hydrogen economy. Using hydrogen instead of Avgas has advantages and disadvantages. Hydrogen has a low tendency to knock (multiple ignition sites causing multiple shock waves to move through the combustion chamber), and has a low minimum energy of ignition. This makes hydrogen prone to premature ignition, especially in the presence of platinum, which is a catalyst for hydrogen combustion. Due to hydrogen's low density, storage is a challenge, as well as fuel introduction into the engine. When using a carburettor, the volumetric efficiency is reduced significantly. Direct injection gives the best fuel economy. Due to the lack of evaporative cooling upon injection and the low quenching distance, the temperatures inside the cylinders are expected to increase. Cooling must thus be promoted. Due to the high flame velocity and low ignition delay of hydrogen, the spark timing must be retarded and high forces are expected in the combustion chamber.

The modification to hydrogen is applied to a Lycoming IO-360-A1B6 engine. This is a four cylinder, four-stroke engine, equipped with a port fuel injection system. The engine has a compression ratio of 8.7, is air cooled and is naturally aspirated. It has a rated engine speed of 2700 RPM and a rated power of 150 kW.

The basis of this thesis is the design of a test set-up. A Safety Analysis is a crucial part in the design of a test set-up, and for this Safety Analysis the risks associated with testing must be evaluated. One of these risks is engine failure due to high pressures and/or temperatures inside the engine. Two research questions are posed, one focused on the design of the test set-up and one focused on the modelling of the pressure and temperature inside the cylinders of the engine. The research questions are as follows:

How can the Lycoming IO-360-A1B6 engine be tested in a safe and effective manner?

What is the effect of the transition to hydrogen on the pressure and temperature inside the cylinders of the Lycoming IO-360-A1B6 engine?

The test set-up consists of two parts: the test cell and the control room, both are 20 ft containers placed apart from one another to comply with safety regulations. The engine is suspended on a test stand, capable of withstanding the forces and torques imposed by the engine. Safety regulations are in place to protect the persons involved in testing, and safe handling of the chemicals must be ensured. Additionally, two documents have to be drafted before testing can take place, the Safety Analysis document and the Explosion Safety document.

For testing, full electronic control over the engine is desired. Therefore, an Electronic Control Unit has been purchased. Additionally, a number of sensors and systems need (re)placing, such as the injection system and the ignition system. The Lycoming IO-360-A1B6 engine is originally equipped with a port fuel injection system. A new port fuel injection system and a direct injection system will be installed. A new, electronically controllable ignition system will be installed as well. To measure the performance of the engine, experimental equipment is acquired. The emissions of the engine will be measured using a 5 gas analyser and the power will be measured using an eddy current dynamometer.

To assess the difference in power, peak pressure and peak temperature between the engine operating on Avgas and on hydrogen, Chemkin is used to model the engine. Chemkin uses a two-zone model to model the

combustion chamber, consisting of an unburnt zone and a burnt zone. The mass flow between the unburnt zone and the burnt zone is governed by the Wiebe function. Equilibrium kinetics, conservation of energy and the ideal gas law are used to model the combustion. Convective heat transfer with the Woschni heat transfer correlation governing the heat transfer coefficient is used to model the heat transfer.

To verify the working of Chemkin and gain better understanding of the important parameters, a sensitivity analysis is performed. Results show that the compression ratio, connecting rod length, inlet valve closed angle, inlet valve open angle, all heat transfer parameters (except heat transfer parameter b) and the Wiebe function parameters have a small impact on the power. The bore, stroke, connecting rod length, inlet valve closed angle, inlet valve opened angle, engine speed and all heat transfer parameters have a small influence on the peak pressure. The only parameter significantly influencing the peak temperature is the equivalence ratio.

To obtain an accurate risk analysis, experimental validation of Chemkin is necessary. However, to perform experimental validation, an accurate risk analysis is necessary. Preliminary predictions are made to base the risk analysis on, and the uncertainty of these predictions is incorporated into the risk analysis. To account for the assumptions, the equivalence ratio, burn duration, pressure before compression and Sutherland's temperature are modified. To account for the differences between Avgas and hydrogen, the temperature before compression, equivalence ratio, heat transfer parameters, Wiebe parameters and Sutherland's temperature are modified. Predictions are made for the Lycoming IO-360-A1B6 engine at 75% power rating, for both port fuel injection and direct injection.

The predictions give a power for Avgas of around 23.5 kW, where a power of 28 kW is expected based on the actual power of the engine. The deviation is most likely caused by an overestimation of the burn duration. For hydrogen, a power of 18.1 kW is found for port fuel injection and a power of 27 kW is found for direct injection. These values comply with values found in literature. The large difference can be explained by the larger volumetric efficiency for direct injection. Additionally, a peak pressure of 55.77 atm is found for hydrogen direct injection, almost double the peak pressure for Avgas. These results are preliminary, as the model is not validated. Additionally, the change in pressure occurs very suddenly for hydrogen combustion, which could signify rough operation and possible engine failure.

The safety margins of the engine allow for an increase in pressure and temperature inside the cylinders. However, the exact implications are unknown at this point. Therefore, a new simulation should be performed for the engine operating on Avgas, while developing more power. To mitigate the risk, engine cooling can be promoted by changing the cooling fins, decreasing the temperature of the cooling air, changing the cooling medium or increasing the heat transfer to the oil. The peak pressure can be decreased by introducing multi-injection, although adverse effects are expected and should be further researched.

To increase the accuracy of the risk analysis, experimental validation for Avgas can be performed. In a later phase of the project, validation for hydrogen can also be performed to allow for the use of Chemkin for different applications, such as engine mapping. The effect of the fuel introduction strategy and the homogeneity on the results should be assessed. By running the engine without heat release, the effects of the ideal gas law, the heat transfer and the gas exchange and friction loss on the results are to be assessed. The amount of blowby is to be measured and the Wiebe function is to be optimised.

As this thesis is a preliminary research, the main conclusions are recommendations for future research. The design of the test set-up must be completed and to ensure safe testing, the Safety Analysis and Explosion Safety documents need to be drafted. The ignition and injection system need replacement to gain electronic control, the ECU software must be configured and the cooling system for the eddy current dynamometer must be designed.

The risk of catastrophic failure due to an increase in pressure and/or temperature is deemed low at this point, although a final simulation should be performed to find a definitive answer. The accuracy of the risk analysis can be increased by performing experimental validation for Avgas. The effect of the increase in gas temperature on the temperature of the engine structure should be further researched. The next step in this project is further research into other high impact events, to gain larger understanding of the risks associated with testing and to obtain permits for the test set-up.

1
INTRODUCTION

According to the International Civil Aviation Organisation, *"the air transport industry is expanding and the future of aviation is a bright one"* [1]. However, with an average annual growth of 4.3% over the next 20 years, an increase in emissions is expected. In the Paris Agreement, an agreement was made to ensure the global temperature rise does not reach 2 degrees Celsius above pre-industrial levels. To reach this goal, carbon emissions must be reduced and climate neutrality must be reached [2]. For the aviation industry to sustain its growth, the emissions per flight must be reduced. Currently, many methods to reach this goal are under investigation, including aerodynamic optimisation, alternative forms of propulsion and logistics optimisation.

The goal of the project, of which this thesis is a part, is to modify one of the engines of a Cessna Skymaster owned by the Dutch Electrical Aviation Centre (DEAC) to operate on hydrogen. As a transition towards hydrogen is not without risk to the engine, first a proof of concept will be performed with another engine, a Lycoming IO-360-A1B6 engine. The project shall be performed in cooperation with another graduate student from the faculty of Aerospace Engineering (W. Frijters [3]) and with students and staff from Deltion College Zwolle. This thesis is divided into two parts. In the first part, the first steps in enabling the transition of the Lycoming engine to hydrogen are taken. Within the scope of this thesis, this mainly consists of the design of the test set-up. An important component in the design is the safety of the test set-up. To obtain permits and be allowed to test the engine, a safety analysis must be performed and the probability and impact of certain risks must be evaluated. One of these risks is catastrophic failure of the engine, due to an increase in internal pressure and/or temperature of the engine. In the second part of this thesis, a scientific research into the implications of the transition to hydrogen on the power, peak internal pressure and peak internal temperature of the engine is performed.

This project is not the first of its kind. Multiple car manufacturers have designed, built and tested vehicles with a hydrogen piston engine, although none are currently commercially available [4]. The majority use a port fuel injection system and similar thermal efficiencies as for gasoline port fuel injection engines are found [5]. Most hydrogen piston engines developed by car manufacturers (such as Ford with the P2000 and BMW with the Hydrogen 7) as well as engines developed for research are water cooled [4] [6]. Experimental research mainly focuses on the efficiency, power and emissions of hydrogen piston engines, and a dedicated fuel injection system is usually designed [5] [6] [7].

In Chapter 2, the motivation for this project as well as theoretical background is given. In Chapter 3 the problem statement and research questions to be answered are further elaborated upon. Then, in Part I, the answers to the first research question are found and documented. Chapter 4 details the design of the test set-up, the safety considerations and the instrumentation of the engine. Chapter 5 gives the main takeaways of this chapter. In Part II the modelling of the engine and the second research question are considered. Chapter 6 gives the theoretical background behind the modelling software used, Chemkin, as well as the assumptions made by the program. Chemkin is verified with a sensitivity analysis in Chapter 7. Preliminary predictions for the pressure and temperature inside the cylinders are performed in Chapter 8, and preliminary conclusions are formed on the risk of catastrophic failure. Validation experiments are proposed in Chapter 9, and finally Chapter 10 gives the concluding remarks and recommendations for the second part of this thesis.

2
THEORETICAL BACKGROUND

To understand the full extent of the issue at hand, Avgas, hydrogen and piston engines must be researched. Section 2.1 gives the relevant characteristics of Avgas, as well as the reasons why its use must be discontinued. Section 2.2 details why hydrogen is a good replacement for Avgas, and why research into direct combustion of hydrogen is useful. Section 2.3 gives theoretical background into piston engines, and Section 2.4 addresses some of the challenges associated with the transition to hydrogen. Finally, the characteristics of the engine used in the project are given in Section 2.5.

2.1. WHY STOP USING AVGAS?

Avgas is a liquid hydrocarbon fuel obtained from fossil sources. The composition varies and typically consists of 4-8% alkanes, 2-5% alkenes, 3-7% cycloalkanes, 1-4% cycloalkenes and 20-50% aromatics [8, p.107]. Tetraethyllead (TEL) is added to the fuel to increase the octane number. Historically, lead was added to all petrol. From 1976 onwards, lead was removed from petrol due to the adverse health effects associated with lead ingestion [9]. As aircraft engines need a high octane number, Avgas still contains lead.

When using Avgas, 3.1 kg CO_2 is emitted per kg of fuel consumed. The fuel has an octane number of 99.5 (compared to 95 and 98 for motor gasoline available in the Netherlands) and contains 0.56 - 0.85 g lead per liter (depending on whether regular or low lead Avgas is used) [10, p.80]. The energy content of Avgas is 43.5 MJ/kg [11]. In addition to CO_2, which is a product of the complete combustion of Avgas, incomplete combustion leads to CO and unburnt hydrocarbon (uHC) emissions. With increased power setting, CO emissions are relatively constant and uHC emissions are decreased. NO_x emissions increase with increasing combustion temperature. With increased power setting, NO_x emissions are increased up to cruise power, after which they decrease. A final emission species to take into account are particulates (soot). With increased power settings, particulate emissions remain relatively constant [10, p.15].

Avgas is a fossil fuel, releasing carbon from the long-term carbon cycle and contributing to global warming. In addition, the use of Avgas leads to the contamination of air, water and food crops with lead, leading to adverse health effects. To comply with the Paris Agreement and contribute towards a more sustainable future with higher air and water quality, the use of Avgas (and other fossil fuels) should be decreased and ultimately outlawed.

2.2. WHY START USING HYDROGEN?

Hydrogen is the most abundant molecule on Earth. It can be obtained either through natural gas steam reforming, using (mostly) fossil natural gas and steam, or electrolysis, using water and electricity. Hydrogen has an energy content of 120.1 MJ/kg and its combustion products are H_2O and NO_x. The high energy density and the lack of carbon emissions are what make hydrogen an attractive alternative for Avgas and other hydrocarbon fuels.

There are two main ways to use hydrogen as a propulsion source: direct hydrogen combustion in for example an Internal Combustion Engine (H2ICE) (typically a piston engine) or oxidation of hydrogen in a fuel cell (H2FC) combined with an electric motor. H2FCs have better fuel economy, but H2ICEs are currently cheaper and allow for bi-fuel operation [12]. The introduction of H2ICEs allows for a gradual introduction of hydrogen infrastructure, starting the momentum for the transition towards a hydrogen economy. Furthermore, as general aviation aircraft have a long lifespan (with for example the DEAC Cessna Skymaster being built in 1972 [13]), changing the technology inside the aircraft is a long and tedious process. Retrofitting existing aircraft with an engine operating on hydrogen can prove a useful solution to decrease emissions in the industry. To understand the challenges associated with hydrogen internal combustion, first the fundamentals of the piston engine must be discussed.

2.3. How Do Piston Engines Work?

Piston engines exist with many variations, the theoretical background will focus only on the mechanisms in the Lycoming IO-360-A1B6 engine. This engine is a four cylinder engine with each engine cycle consisting of four strokes, each stroke consisting of 180°. In Figure 2.1 (adapted from W.W. Pulkabrek [14, p.26]) a schematic overview of the working of a four stroke engine is given. The cycle starts at top dead centre (TDC) with the firing of the spark plug with both the inlet and exhaust valve closed, followed by the power stroke. Once the piston reaches bottom dead centre (BDC) the exhaust valve is opened and the exhaust gases are pushed out in the exhaust stroke. After the piston reaches TDC, the exhaust valve is closed and the inlet valve is opened and fresh gas mixture is pulled in: the inlet stroke. At BDC the inlet valve is closed and the gas mixture is compressed in the following compression stroke. The chemical power is converted to mechanical power through the crankshaft and heat which is absorbed by the cylinder.

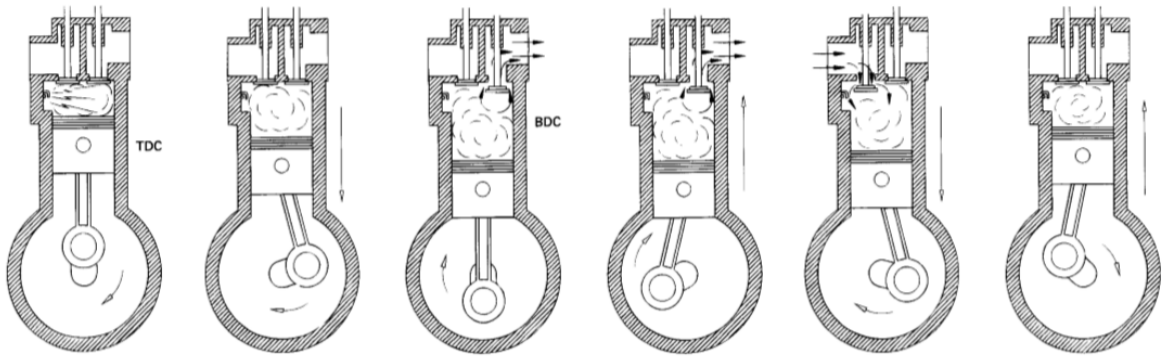

Figure 2.1: Schematic overview of a four stroke engine (adapted from [14, p.26]).

Fuel can be added to the ingested air in multiple ways. The Lycoming IO-360-A1B6 engine uses a carburettor, where fuel is mixed with the incoming air in the carburettor. During the inlet stroke the fuel-air mixture is drawn into the combustion chamber. The fuel-air mixture is ignited using a spark plug. The timing of the valves is related to the crankshaft rotation. The timing of the spark plug is determined with a camshaft sensor, which monitors the location of the camshaft in the combustion cycle. In Figure 2.2 (adapted from [15]) a schematic overview is given of the timing of a gasoline engine. The inlet valves usually start to open between 25 and 10° before TDC (bTDC), and are fully opened at TDC after the exhaust stroke. The inlet valve is closed again about 40-50° after BDC (aBDC), and is thus opened for the entire inlet stroke. With the inlet valve only closing after BDC, this means that during the compression stroke some air is pushed back into the inlet manifold.

When a direct injection mechanism is used, injection starts around 15° bTDC and ends 5° after TDC (aTDC). Ignition occurs between 30 and 10° bTDC, depending on the fuel delivery strategy and the injection timing. The exhaust valve opens around 60-40° before BDC (bBDC) during the power stroke and is closed again at 8-10° aTDC. There is a brief window in which both the inlet and the exhaust valve are opened, leading to exhaust gas being fed back into the inlet and then drawn back into the cylinder, decreasing the power output of the engine [14].

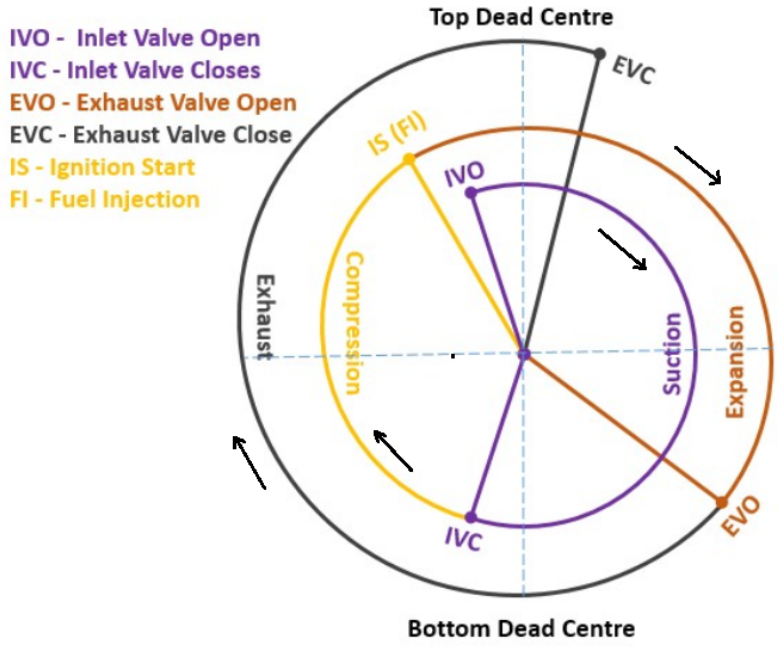

Figure 2.2: Schematic overview of the timing of a four stroke engine (adapted from [15]).

The heat formed during combustion is absorbed by the cylinder walls, heating up the whole engine. The exterior of each cylinder is covered in cooling fins, optimising cooling through forced convection. The inlet and exhaust valves are fragile components when it comes to temperature, and it must be ensured that the valves and the valve seat fit perfectly to ensure heat transfer from the valves to the cylinder. The piston head also absorbs heat and is cooled by splashing lubricant on the bottom of the piston head. The lubrication oil is stored in the crankcase below the piston and is also used to lubricate the engine. As the piston moves, there is a small clearance between the piston and the cylinder. Fuel, air and exhaust gases can seep past the piston into the crankcase, a phenomenon known as blowby. Increasing the compression ratio of the engine increases the power output, according to Equation 2.1, with an increase in work over a constant amount of time leading to an increase in power. Here, W is the work, p is the pressure and V is the volume.

$$W = \int p dV \tag{2.1}$$

An increase in compression ratio however, also increases the tendency to knock. Knock occurs when the temperature of the fuel increases above the autoignition temperature (for example due to compression). The fuel ignites at multiple fronts and multiple pressure waves travel through the combustion chamber, leading to a 'knocking' sound and potentially damaging the engine. The tendency to knock is a fuel property and is expressed with the octane number, where a high octane number means the fuel has low tendency to knock.

2.4. Hydrogen Properties in a Piston Engine

Hydrogen has a high octane number of 130+ [16, p.21] compared to Avgas with 100. Hydrogen thus has a lower tendency to knock and hence higher pressure ratios can be used to increase the power output. However, hydrogen also has a (very) low minimum energy of ignition of 0.02 mJ compared to 0.24 mJ for gasoline [17]. In addition, platinum is a catalyst for hydrogen combustion. The presence of local hot spots as well as platinum components (as found in spark plugs) must be avoided, as these might lead to premature ignition.

Hydrogen has low density, which means high volumes of hydrogen must be stored and used. There are multiple methods to store hydrogen: cryogenic (below 20 K), compressed (at a pressure of up to 700 bar), or a combination hereof. The high volume also means that not all fuel introduction strategies are suitable. In Section 2.3 the carburettor was already briefly discussed. When using a carburettor and when using manifold injection, the fuel is mixed with the air before entering the combustion chamber. The volume of the

hydrogen displaces some of the volume of the air, eventually leading to a smaller amount of the combustable mixture entering the combustion chamber, leading to a low volumetric efficiency. In addition, using a carburettor gives no control over the fuel-air mixture in the individual cylinders. With port fuel injection, the fuel is injected into the inlet manifold when the inlet valve is opened, giving a higher volumetric efficiency. A final strategy is to use direct injection, where fuel is directly injected into the combustion chamber (at high pressure) just before ignition. This leads to the highest volumetric efficiency. Flashback (where the flame enters the intake manifold) is also eliminated, but placing the injector inside the combustion chamber does introduce a hot spot and the injector must be able to withstand the high temperatures inside the combustion chamber.

In an engine fueled with liquid fuel, evaporative cooling takes place as the fuel evaporates. As hydrogen is already in a gaseous state, this cooling does not take place. In addition, hydrogen can be operated at higher temperatures due to the higher autoignition temperature. Due to the high octane number, the compression ratio can be increased to increase power output. Keeping in mind that hydrogen has a low quenching distance and thus there is a small distance between the flames and the cylinder wall [18], this could lead to high temperatures inside the intake manifold, the combustion chamber walls and the exhaust manifold.

Cooling of the Lycoming IO-360-A1B6 engine is achieved using three methods. The first is oil cooling. Lubrication oil is splashed on the bottom of the piston head, promoting convection through the piston head and cooling the combustion chamber. The lubrication oil is stored in the crankcase, and due to blowby (leakage of hydrogen past the piston) a build up of hydrogen may occur in the crankcase. To mitigate the risk of combustion in the crankcase, the crankcase must be ventilated. As lubrication oil easily evaporates into hydrogen [19], oil levels diminish rapidly as the crankcase is ventilated. Either a different type of lubricant must be chosen or the lubrication oil must be topped up regularly.

The second method of cooling is air cooling. The exterior of the cylinders is covered in cooling fins, which can be seen in Figure 2.3 [20]. As the aircraft flies, air is forced past the cooling fins, cooling the engine by means of forced convection.

The third way to cool the cylinder is by promoting conduction through the cylinder itself by perfectly aligning all components. This is especially important for the valves, as here the temperature reaches high values. One way to promote cooling in the exhaust valve is by using a hollow stem valve, filled with liquid sodium. The sodium near the hot valve foot vaporises and rises to the top of the valve, toward the cool end of the valve. Here the vaporised sodium condenses. Due to the phase change, there is a large transfer of energy, increasing the effective heat conduction and thus cooling the valve [14, p.325].

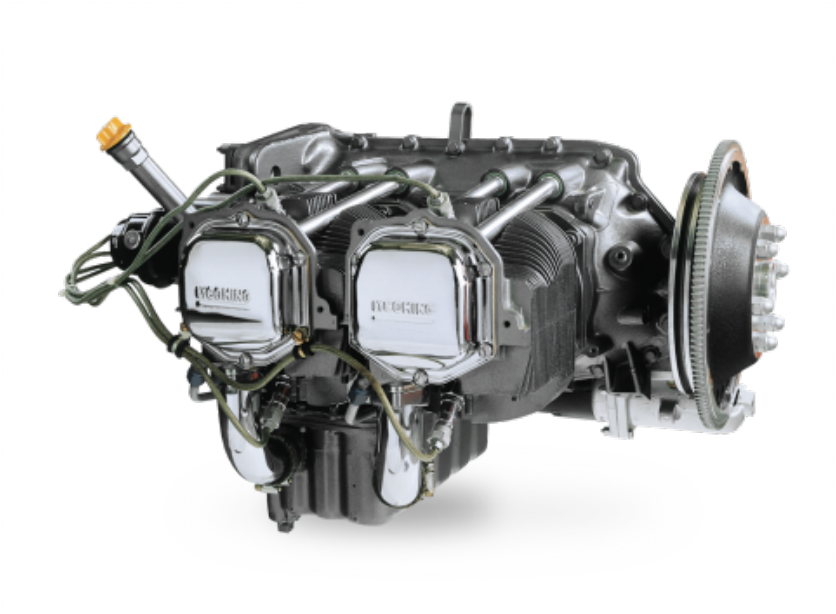

Figure 2.3: Photo of the Lycoming IO-360-A1B6 engine showing the cooling fins [20].

Hydrogen has a high flame velocity compared to Avgas [17]. This high flame velocity leads to almost constant volume combustion and thus increases the efficiency of the engine, as well as the torque output. However, this high flame velocity also leads to high forces inside the combustion chamber. The components inside the combustion chamber must be able to withstand these high forces.

In addition to high flame velocity, hydrogen has low ignition delay. This means that combustion initiates rapidly after spark plug ignition. To obtain a quantification of the required spark timing, a comparison can be made with natural gas. B. Nagalingam et al. ([21]) suggests an average of 20° retardation of spark plug ignition timing for hydrogen compared to natural gas, while for natural gas an advanced spark plug ignition timing of 2-10° is suggested compared to a gasoline fueled engine [22, p.220]. A quick calculation gives a retardation of 10-18° for hydrogen compared to gasoline.

2.5. THE ENGINE

An illustration of the Lycoming IO-360-A1B6 engine has been given in Figure 2.3. It is a four stroke engine with four cylinders, equipped with a port fuel injection system. The engine has a compression ratio of 8.7, is air cooled and is naturally aspirated. It has a rated engine speed of 2700 RPM and a rated power of 150 kW. The engine is used in a large range of aircraft, among which some Cessna aircraft.

3
PROBLEM STATEMENT

In this thesis, the first steps towards the modification of the engine to hydrogen are taken. These first steps are taken in cooperation with another graduate student from the faculty of Aerospace Engineering and other students and staff from Deltion College Zwolle.

A general plan is agreed upon, which consists of the following parts:

- Design of the test set-up;
- Construction of the test set-up;
- Testing of the Lycoming IO-360-A1B6 engine on Avgas and validation of the test set-up;
- Initial modification to the Lycoming IO-360-A1B6 engine to gain full control over the engine;
- Testing of the partially modified Lycoming IO-360-A1B6 engine to validate the modifications;
- Modification of the Lycoming IO-360-A1B6 engine to operate on hydrogen;
- Testing of the modified Lycoming IO-360-A1B6 engine operating on hydrogen.

For the scope of this thesis, only the first step is addressed: the design of the test set-up. A research question is posed:

How can the Lycoming IO-360-A1B6 engine be tested in a safe and effective manner?

This research question can be divided into several sub-questions, which are divided between the two thesis students.

1. What equipment must be acquired and/or designed to be able to test the Lycoming IO-360-A1B6 engine?
2. What should the lay-out of the test set-up look like?
3. How can the Lycoming IO-360-A1B6 engine safely be placed in the test set-up for testing?
4. What safety precautions must be taken to ensure safe operation of the test set-up?
5. How should the engine be modified to gain electronic control over the engine?

The first two sub-questions are answered by the other graduate student working on this project, and only a brief overview of the results will be given in this report. The fourth sub-question about the safety of the test set-up requires an extensive evaluation of the risks during testing. For some events, the probability and impact of these events might be straightforward, but for others they are not. To assess the probability and impact of certain events, an in depth research must be performed.

Several high impact events could occur during testing, which are listed below.

- Engine failure due to knock;
- Engine failure due to high forces;
- Engine failure due to high temperatures;
- Engine failure due to vibrations;
- Flashback into the hydrogen tank and subsequent detonation;
- A hydrogen leak and subsequent detonation;
- Combustion in the engine crankcase.

The risk of flashback into the hydrogen tank and combustion in the engine crankcase can easily be mitigated during the design phase by using a direct injection system and ventilating the crankcase. An in depth research of the consequences of a hydrogen leak is performed by the other thesis student. Knock is strongly related to ignition delay [23], and it is decided to leave this topic to a third graduate student, who will (among other things) study the ignition delay mapping for the Electronic Control Unit (ECU). At this point in the project, vibrations modelling is not feasible, which leaves the forces and temperature inside the combustion chamber.

The conditions inside the cylinder during hydrogen combustion can be related to the conditions inside the cylinder during Avgas combustion. Conclusions can be formed on the change in forces and engine temperature, and the implications on the operating conditions of the engine. This leads to the following research question.

What is the effect of the transition to hydrogen on the pressure and temperature inside the cylinders of the Lycoming IO-360-A1B6 engine?

This research question can again be divided into several sub-questions.

1. Which tool is appropriate for modelling the pressure and temperature inside the cylinder?
2. What is required to ensure accurate results from this tool?
3. What preliminary predictions can be made regarding the pressure and temperature when changing from Avgas to hydrogen?
4. What is the risk of catastrophic failure due to an increase in pressure and/or temperature inside the cylinders of the engine?
5. How can the risk of catastrophic failure be mitigated?

I

ENGINE TESTING

4
ENGINE TEST SET-UP

Before testing can start, the test set-up must be designed and constructed. As mentioned before, the project is not performed alone, but in cooperation with another student from the faculty of Aerospace Engineering. The test set-up is designed by the abovementioned student and Section 4.1 gives a brief overview of the design of this test set-up. In Section 4.2 the design of the engine stand is discussed, after which the safety regulations are elaborated upon in Section 4.3. In Section 4.4 the alterations necessary to gain electronic control of the engine are discussed and Section 4.5 gives an overview of the acquired instrumentation.

4.1. TEST SET-UP EQUIPMENT AND DESIGN

The test set-up consists of two parts: the test cell and the control cell. Both the test cell and the control cell are 20 ft containers, placed apart from one another to adhere to safety regulations. The control cell contains the components necessary to control the engine, such as computers and computer screens, but also storage, tables and chairs.

The test cell itself contains the engine, the engine is connected to the test equipment and an exhaust pipe. The engine is air cooled from the top of the engine, and ventilators are placed in the test cell wall to ventilate the test cell. A humidifier is placed inside the test cell to regulate the humidity. Ideally an exhaust hood is placed above the engine to ventilate any hydrogen that might lead from the engine or fuel tank. As the engine must be cooled from the top, this is not possible. The consequences hereof are still under investigation. Cameras, leak sensors and a special camera to detect hydrogen flames are placed inside the test cell. A more extensive overview is given by W. Frijters [3].

4.2. ENGINE TEST STAND

The engine cannot just be placed on the floor of the test cell, but must be suspended in a test stand. This test stand must be small enough to fit in the test cell, strong enough to withstand the gravitational and vibrational loads and the torque induced by the engine, and designed in such a manner that easy access to the engine is provided. Furthermore, the test stand must be able to be removed from the test cell.

The dimensions of the test cell are 6.1 m in length, 2.44 m in width and 2.59 m in height. The dimensions of the engine that the test stand must support are 0.78 m in length, 0.87 m in width and 0.49 m in height. The engine has a mass of 151 kg and a rated power of 150 kW, which, together with the rated rotational speed of 2700 RPM leads to a torque of 527.5 Nm. The test stand is designed, based on practical experience, rather than an extensive computation of the loads in each component. In Figure 4.1 a technical drawing of the test stand can be found. The test stand can be removed from the test cell either by using the wheels placed under the ends of the test stand, or by placing the forks of a fork lift inside the rectangular beams and lifting the test stand. When in operation, cables which are attached to the floor are pulled over the base of the test stand and connected to the floor by means of a hook. The test stand is then lifted using the four feet attached to the sides of the test stand, lifting the wheels of the floor and securing the test stand in place.

The engine is attached to the test stand with eight beams, configured in such a way that the load is spread. These beams are connected to a Dynafocal engine mount ring, which is in turn connected to the engine.

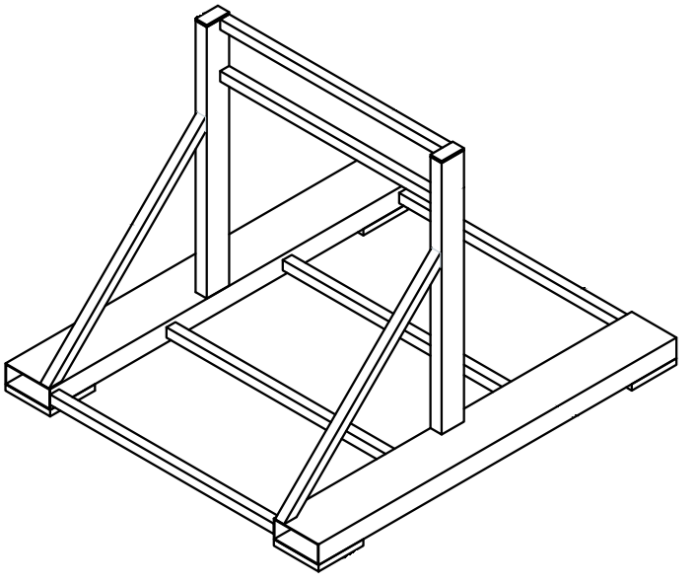

Figure 4.1: Schematic overview of the engine test stand.

4.3. Safety Regulations

To ensure the safety of the persons involved in testing and the environment, safety regulations need to be adhered to. These safety regulations can be divided into three categories: safety regulations regarding the lay-out and construction of the test cell, safety regulations regarding the chemicals used inside the test cell and safety regulations regarding documents that need to be drafted to ensure safe operation.

4.3.1. Safety of the Test Cell

There are three preset safety considerations to keep in mind for the test cell: PGS 15, occupational health and safety legislation, and local permits and regulations.

The occupational health and safety legislation [24] is put in place to protect the persons working in, on and around the test cell. The ventilation system must always be ready for operation, and contaminated air may not be circulated into a space where this contamination is not present. Hazardous materials must contain the official name, relevant dangerous components, pictograms, signal words and hazard indications, and a Safety Data Sheet must be present. Employees must be warned optically or acoustically in the case of an explosion hazard, and emergency lighting or personal lighting must be present. Smoking, eating and drinking inside the test cell is prohibited.

When performing maintenance, a log must be kept. Maintenance may only be performed when the machine is no longer under pressure and/or carrying voltage, which must be ensured with a lock-out tag-out procedure. If moving parts form a hazard, screens must be placed to prevent injury, while minimally reducing visibility and functionality. The controls must be placed outside the danger zone and the machine must be able to switch off using these controls. There must also be an emergency kill switch. Instructions must be provided on the working of the machine. If there are consequences for persons not directly involved in the project, safety documents must be provided to them.

All persons involved in testing must have access to personal protective equipment, suitable for the projected risks (such as skin and eye contact with Avgas) without causing risks. When a sound level of 80 dB(A) or higher is measured, hearing protection must be available, while for a sound level of 85 dB(A) or higher, wearing the hearing protection is mandatory. Sound levels inside the ear may not exceed 87 dB(A). Restrictions also exist for vibrations, with a limit at 1.15 m/s^2 for 8 hours a day. Instructions must be given on the risks, measures and signals of damage.

PGS 15 gives instructions on working with and storage of hazardous materials, such as Avgas and hydrogen. Avgas is generally stored in drums, while hydrogen is stored in gas cylinders. These drums and gas cylinders must be protected from falling. There are two types of storage facilities: open and closed facilities. Closed

facilities must be ventilated, while open facilities must have draining and fire proof flooring. The Safety Data Sheets for the materials must be present, as well as instructions in the case of a leak or incident. Any contaminated rain water (for example due to a leak) may not enter the sewage system. No smoking is allowed within 2 m of the storage facility and per 200 m^2 of storage area, a fire extinguisher with at least 5 kg or L extinguishing agent must be present. The storage facility should not be accessible to unauthorised persons and an emergency response worker must be present. Gas cylinders must be placed at 5 m from other buildings when not placed in a fire proof cabinet, which reduces to 1 m for fire proof cabinets with a 30 minute delay. For Avgas drums this is 10 m without a fire proof cabinet and 5 m for fire proof cabinets with a 30 minute delay. Finally, the amount of gas cylinders/drums in the test cell is restricted to the necessary amount for one day of operation plus one reserve.

It is currently unclear where the test cell will be placed, which means local permits and regulations cannot be taken into account at this stage.

4.3.2. Safety of the Chemicals

Two main chemicals are used in the test cell: Avgas and hydrogen. Although in this thesis hydrogen will not be used yet, the implications of the safety regulations on the design of the test cell must be researched and implemented to make the test cell suitable for both Avgas and hydrogen. An overview is given of the information in the Safety Data Sheets relevant to the design and operation of the test cell.

According to the Safety Data Sheet as provided by Shell Trading Canada [25], Avgas is a blue liquid with a boiling range of 25-170°C. Its flash point is below -40°C, which means vaporisation occurs during normal operation. When handling Avgas, safety glasses and chemical resistant gloves and boots must be worn. In addition, non-sparking tools must be used and all equipment must be explosion proof and earthed, to prevent static discharge. Avgas can be stored in drums, which may be stacked to a maximum of three high. The drums must be kept tightly closed and stored away from ignition sources, in a well ventilated area.

In case of a leak, residual material must be contained to prevent damage to man and environment. The source of the leak must be dealt with (only when possible without personal risk) and all possible sources of ignition must be removed. The vapour must be dispersed or directed to a safe location to keep the airborne concentration below the explosion limit of 1% by volume. Suitable extinguishing agents for Avgas are foam, water spray or fog. Direct water jets can cause a steam explosion and should be avoided. The use of foam and water on the same surface should also be avoided as water destroys the foam. The residual material must be contained to prevent the contamination of surface and ground water.

In the Safety Data Sheet as provided by Linde Inc. [26], hydrogen is identified as a colourless and odourless gas with a boiling point of -252.8°C. Its autoignition temperature is 566°C and the flammability limit is 4-77% by volume. It is stored in pressurised cylinders, which must be stored away from sources of ignition and below a temperature of 52°C. When handling hydrogen cylinders, leather gloves and safety shoes must be worn and the cylinders must be protected from physical damage. Cylinders must never be lifted by their cap. When working with hydrogen, non-sparking tools and explosion proof equipment must be used.

In case of a leak, all sources of ignition must be removed and the flow of hydrogen must be stopped if it is safe to do so. The area must be ventilated and before entering the test cell the atmosphere must be monitored. Hydrogen has a low minimum energy of ignition, which means any leaking hydrogen might ignite spontaneously. A hydrogen flame is nearly invisible, and it should not be attempted to extinguish the flame as flammable vapours may spread from the leak, forming a combustable mixture elsewhere. Instead, the flow of hydrogen must be stopped and endangered containers (for example the hydrogen cylinder(s) present in the test cell) should be cooled with a water spray jet. The water used should be prevented from entering sewage and drainage systems.

4.3.3. Drafted Documents for Safety

Two different documents have to be drafted to assess and mitigate the risks associated with testing in the test set-up: A Safety Analysis, in which a general risk analysis is documented, and an Explosion Safety (ATEX) document, in which the explosion safety of the test set-up is evaluated. In the Safety Analysis report, the probability and consequence of events must be documented. To this cause, an in depth research regarding the forces and temperatures inside the test engine is performed in Part II. In Appendix A templates for the Safety Analysis and Explosion Safety reports are given.

4.4. Electronic Control

To gain electronic control over the engine, equipment, sensors and software need to be installed. In this section, background is given on the basic working of the required equipment.

4.4.1. ECU and Sensors

The Electronic Control Unit acquired for the Lycoming IO-360-A1B6 engine is the MoTeC GPRDI-M182 ECU [27]. This is an ECU developed for the automotive industry, suitable for engines with up to 12 cylinders with direct injection. There is the possibility to replace (some of) the injectors with port fuel injectors. The M182 ECU has 136 in- and output options, with the injection system, ignition system, crankshaft position sensor, camshaft position sensor, throttle position sensor, manifold pressure sensor, fuel pressure sensor, air temperature sensor and coolant temperature sensor as mandatory components for basic operation.

In its most basic configuration, an ECU has two inputs and two outputs. The outputs are the amount of fuel required and the ignition timing. These parameters are determined by tables, which are based on experimental data, also known as engine mapping. The inputs are the engine speed and either the throttle position or the manifold pressure. The combination of engine speed and throttle position/manifold pressure thus gives a value for ignition timing and fuel required. The tables are dependent on the engine type and its configuration. The M182 ECU does not measure the engine speed directly, but derives it from the crankshaft position.

4.4.2. Injection

As mentioned in Section 2.2, port fuel injection and direct injection are both favourable techniques for the introduction of hydrogen into the combustion chamber. Therefore, both will be installed on the Lycoming engine. Initially, regular gasoline injectors will be installed, while in a later stage these will be replaced with special hydrogen injectors. The underlying working of port fuel injection and direct injection is similar. The timing of injection differs, as for port fuel injection, injection occurs during the inlet stroke, while for direct injection this occurs after the compression stroke, just before ignition. This also means that port fuel injection requires lower pressures (approximately 6 bar) compared to direct injection (up to 350 bar) [28].

A schematic overview of the injection system is given in Figure 4.2 [29]. The injection system consists of the fuel tank, fuel filter, fuel pump, pressure regulating valve, high pressure pump, pressure sensor, common rail, pressure relieve valve and injectors. It is controlled by the ECU based on the throttle position sensor, the manifold pressure sensor, the coolant temperature sensor and the speed sensor. Fuel is pumped out of the fuel tank, to the common rail. A pressure sensor communicates the pressure of the fuel to the ECU, which in turn regulates the fuel flow with the pressure regulating valve. The ECU determines the desired fuel pressure based on the engine condition as given by the sensors. In the common rail, the fuel is sent to the individual fuel injectors. Any additional pressure is relieved with the pressure relieve valve, and the fuel is led back to the fuel tank [29].

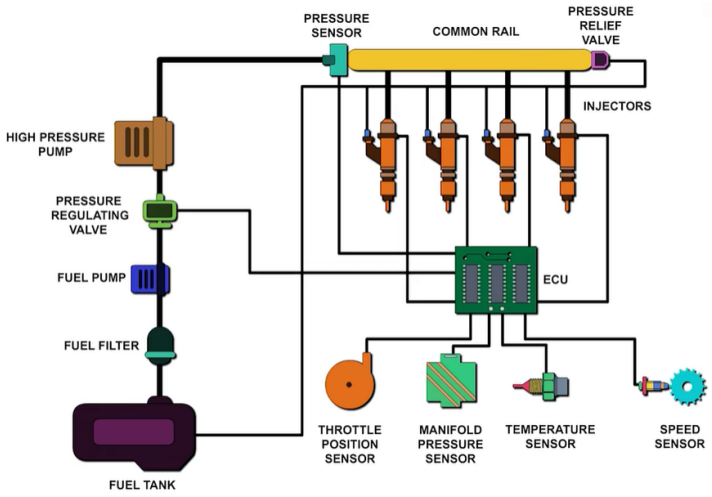

Figure 4.2: Schematic overview of a common rail fuel injection system [29].

As the components currently present on the Lycoming engine are outdated, these will all be replaced.

4.4.3. IGNITION

Ignition systems can be divided into different categories, based on the electricity source (magnet or battery), whether or not a distributor is used, and the method of inducing a flux in the secondary coil. The Lycoming engine originally has a magneto ignition system, of which a schematic overview is given in Figure 4.3 [30]. It consists of an ignition switch, a magneto, a primary and secondary coil, capacitor and contact breaker, distributor and spark plugs. When the switch is turned on and the magnet rotates, an electrical current is induced in the primary coil. This current flows through the contact breaker. At a specific point in the engine cycle, based on the camshaft, the contact breaker opens. The current now goes through the capacitor, changing the current through the primary coil. This change induces a current in the secondary coil, which then flows to the distributor. The distributor then distributes this current to the spark plugs, which in turn create a spark. This system is compact and has low maintenance costs [30]. However, this system does not give independent control over the spark timing, which is desired for testing with hydrogen. Therefore, it will be replaced with another system.

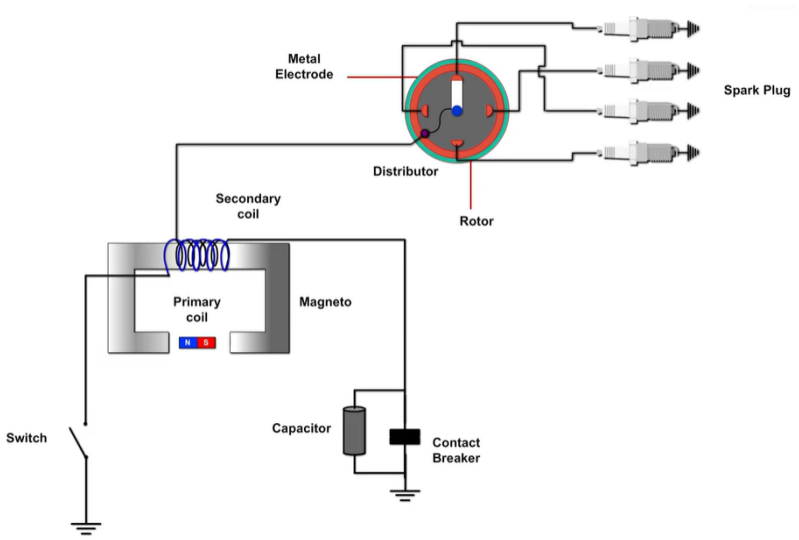

Figure 4.3: Schematic overview of a magneto ignition system [30].

To ensure independent control over the spark timing, the link between the camshaft and the contact breaker must be broken. This link is replaced by the ECU. Whether or not a distributor is used, is still under discussion.

4.5. EXPERIMENTAL EQUIPMENT

Initially, the focus is on the emissions and performance of the Lycoming IO-360-A1B6 engine. To obtain these results, testing equipment is necessary. Section 4.5.1 elaborates on the equipment needed to measure emissions, while Section 4.5.2 discusses the equipment needed to measure performance.

4.5.1. EMISSIONS

Relevant emissions for Avgas combustion are CO_2, CO, NO_x and unburnt hydrocarbons (uHC). The primary greenhouse gases are H_2O, CO_2, CH_4, NO_2 and O_3. These molecules absorb energy radiated by the Earth, and re-emit this energy in different directions. Some of this re-emitted energy returns to Earth and heats the Earth surface. CO_2 directly causes approximately 20% of the greenhouse effect; water vapour amounts to 50%. However, as the CO_2 concentration in the atmosphere increases, the atmosphere temperature increases, disturbing the balance between liquid and gaseous water on Earth. More water vaporises into the air, increasing the greenhouse effect [31].

CO is a product of incomplete combustion, displacing oxygen in the blood. Furthermore, CO reacts with OH to form O_3 [32, p.7.18], in turn decreasing OH concentrations. As OH acts as a sink for CH_4 through oxidation [32, p.509] (and CH_4 is a greenhouse gas), CO indirectly contributes to the greenhouse effects. An increase in O_3 formation also leads to a decrease in air quality [32, p.88].

Similarly to CO, NO_x does not have a direct effect on the greenhouse effect. NO_x emissions affect O_3 and CH_4 concentrations, as well as air quality in a similar manner as CO [32, p.174]. However, locally, the presence of NO_x can increase natural CO_2 sinks such as forests [32, p.468], leading to a net negative effect on the greenhouse effect on a global scale [32, p.662]. uHC oxidate to form CO [32, p.174] and contribute to O_3 formation in a similar matter as CO and NO_x [32, p.670].

The emissions are measured with a 5 gas analyser from Bridge Analyzers, capable of measuring CO, CO_2, fuel dependent uHC (hexane for gasoline), O_2 and NO_x [33]. The probe is placed inside the exhaust and the data is logged. The gas analyser cannot measure just any hydrocarbon but must be configured to measure hexane for Avgas combustion. Based on the hexane content in the exhaust gases, the air-fuel ratio and combustion efficiency are computed.

CO, uHC and CO_2 are measured using Non Dispersive Infrared (NDIR). In NDIR, infrared light is used to detect different molecules, as different molecules absorb different wavelengths. The decrease in transmitted infrared light is measured and based on this, the concentration of the molecule can be determined [34].

O_2 and NO_x are measured using an electro-chemical sensor, where a chemical reaction is used to form electrons and induce a current. The magnitude of the current is related to the concentration of the species [35].

4.5.2. PERFORMANCE

To be able to say anything meaningful about the emissions, the performance of the engine must be measured. The equipment used is a Schenck W 400 eddy current dynamometer. The eddy current dynamometer consists of a toothed rotor connected to the driveshaft, cooling chambers and a magnetic circuit in a stator. A schematic overview is given in Figure 4.4 [36]. As current is led through the coil in the stator, a magnetic field is exited. The teeth of the rotor rotate through this magnetic field, constantly changing it. As the system wants to counteract the change, a drag force on the toothed rotor is induced. This drag force slows down the toothed rotor and the driveshaft, converting the kinetic energy into heat [37, p.4-5]. The W 400 dynamometer measures rotational speed and torque, which relate to power following Equation 4.1, with p power, T_q torque and N rotational speed.

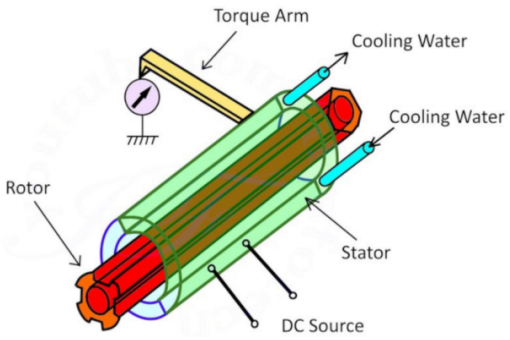

Figure 4.4: Schematic overview of the eddy current dynamometer [36].

$$p\ [\text{kW}] = \frac{1}{9.5488} T_q\ [\text{Nm}] \cdot N\ [\text{RPM}] \tag{4.1}$$

The W 400 dynamometer is water cooled and thus needs a water supply. The inlet cooling water pressure is to be between 0.4 and 4 bar, with a maximum temperature of 40°C. The maximum temperature of the water outlet is 50°C for calcereous water (>5 °dH) and 70°C for low-lime water (<5 °dH). With an average tap water hardness of 7.8 °dH around Amsterdam [38], a maximum of 50°C is used. The required water flow is determined using Equation 4.2, with Q_v the water flow, p the power and ΔT the difference in temperature between the inlet and the outlet of the dynamometer [37, p.26-27].

$$Q_v\ [\text{m}^3/\text{h}] = 0.86 \frac{p\ [\text{kW}]}{\Delta T\ [^\circ\text{C}]} \tag{4.2}$$

A circuit cooling system will be used, where the inlet water is taken from a tank, used to cool the dynamometer and then cooled using a heat exchanger before flowing back into the tank. The lower the difference between the inlet and the outlet temperature, the smaller the heat exchanger needed but the larger the water flow. Figure 4.5 shows the correlation between the temperature difference and the water flow for different power settings. A pressure drop between the inlet and the outlet is required to ensure a proper flow of water, which is realised using a water pump. The required pressure drop is dependent on the dynamometer type and the water flow and is given in Figure 4.6 [37, p.28]. It is assumed the WS 400F dynamometer has similar characteristics to the W 400 dynamometer. For this dynamometer, the cooling water flow is between 7.4 and 24 m^3/h, with a corresponding pressure drop between 0.4 and 4 bar. To ensure broad applicability of the system, the system is designed for a power of 400 kW. Keeping in mind the water flow as determined above, this limits the temperature change to a value between 15 and 45 °C. A heat exchanger must thus be found with the capability of releasing 400 kW of heat with a water flow between 7.4 and 24 m^3/h. A heat exchanger capable of continuous cooling is too large for practical use. Therefore, it is decided to limit the run time of the engine and dynamometer. The design of this heat exchanger is considered in a future stage of the project.

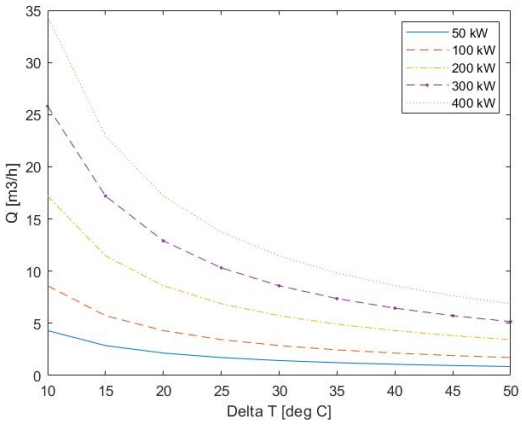

Figure 4.5: Required water flow to cool the dynamometer for different power settings.

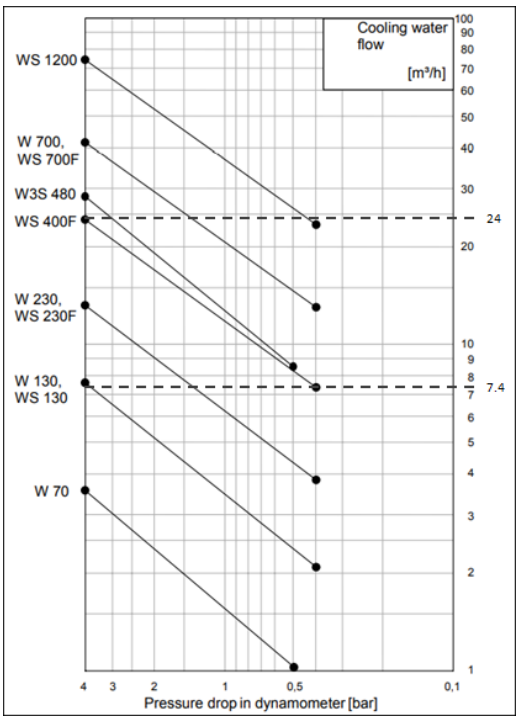

Figure 4.6: Required pressure drop to ensure the required water flow [37, p.28].

5
CONCLUDING REMARKS PART I

To reduce emissions in the aviation industry, alternative methods of propelling aircraft are considered. The project, of which this thesis is a part, focuses on direct hydrogen combustion in a piston engine. This thesis is one of the first theses in this project, and provides relevant preliminary research to be used by future thesis students.

The first part of this thesis focused on the steps required to enable safe and effective testing of the Lycoming IO-360-A1B6 engine.

5.1. CONCLUSIONS

A preliminary test set-up design was conducted, with the test set-up consisting of two parts: a test cell and a control room. Both are 20 ft containers, and the test cell is equipped with a test stand for safe testing of the engine, a dynamometer to measure the engine power and a 5 gas analyser to measure the emissions.

To ensure safe testing of the engine, regulations have to be kept in mind and several safety documents need to be drafted. The regulations regulate the storage and handling of chemicals and the well being of persons involved in testing. A Safety Analysis and an Explosion Safety (ATEX) document must be drafted before testing can start.

To gain electronic control over the engine, the engine must be equipped with an ECU. The ECU requires an injection system, an ignition system, crankshaft position sensor, throttle position sensor, manifold pressure sensor, fuel pressure sensor, air temperature sensor and coolant temperature sensor for basic functioning. The Lycoming IO-360-A1B6 engine's current injection system is not sufficient, and will be replaced with a new, electronically controllable port fuel injection system. Additionally, a direct injection system will be installed. For Avgas testing, gasoline injectors are used, while for hydrogen testing special hydrogen injectors will need to be used. The current ignition system relies on a magneto and distributor, and will be replaced with an electronically controlled system.

5.2. RECOMMENDATIONS

As this report is a preliminary research, many recommendations follow. First and foremost, the design of the test set-up must be completed. More information on this can be found in W. Frijters [3].

Furthermore, the location of the tests must be chosen and local regulations must be considered. As these local regulations might influence the design of the test set-up, this must be done as soon as possible. The Safety Analysis document and Explosion Safety document must be drafted, and risk mitigation strategies must be incorporated in the design.

Both the ignition and injection system need to be replaced, to gain electronic control. For Avgas, a regular electronic ignition system can be used. For hydrogen however, the effect of the low ignition energy must be researched and platinum in the spark plug must be avoided. The existing port fuel injection system must be replaced and a direct injection system must be installed in the second spark plug hole in the cylinders. For hydrogen, all injectors must be replaced to accommodate hydrogen injection. As hydrogen injectors are not commonly available, this might require the design of hydrogen injectors for both port fuel injection and direct injection.

To be able to operate the engine, the ECU must be installed and the engine must be mapped. This can either be done experimentally, or using a validated engine model.

The eddy current dynamometer is used to measure the torque output of the engine. The cooling system for the dynamometer must be designed according to the design restrictions given in Section 4.5.2. Furthermore, decisions must be made on the operating time of the engine, since continuous cooling of the dynamometer requires an unfeasibly large heat exchanger.

II

PRESSURE AND TEMPERATURE INSIDE THE ENGINE

6
ENGINE MODELLING PROGRAM

In this chapter, the working and assumptions of the modelling program used, Chemkin, are discussed. This information is used in subsequent chapters to assess the effect of the input parameters on the results and to identify the shortcomings of the model. In the scope of this thesis, Chemkin is used to compute the pressure, temperature and power of the engine, as these are key indicators to assess whether the engine can endure the transition to hydrogen.

The engine modelling program used in this thesis is Chemkin, which has a validated, zero-dimensional two-zone combustion model. The choice for Chemkin was quite imperative, due to its availability. Using Chemkin instead of a self made model has numerous advantages. Chemkin uses relatively complex combustion mechanisms and has a long history of validation. Furthermore, it is easy to use and it is compatible with Ansys Forte, which can be used to model the whole engine in a future research stage. However, Chemkin does not allow for any additions to the program to make it more accurate and there is little control over convergence.

Overall, using Chemkin instead of a self made model saves time, while only imposing minor issues in this stage of the research. In the subsequent sections, the working and inputs of Chemkin are discussed. In Section 6.1 the implementation of the fuel in Chemkin is explained, and in Section 6.2 the physical modelling of the engine is described. The parameters stipulating the operating conditions are given in Section 6.3 and the method used to compute the heat transfer is given in Section 6.4. The mechanism governing combustion is given in Section 6.5. In Section 6.6 a short overview of the main takeaways is given, while in 6.7 an overview of the assumptions is given.

6.1. FUEL SPECIFICATIONS

Chemkin needs to be provided with information on the species inside the combustion chamber. Two data files must be provided, one detailing the gas phase kinetics of the fuel and the other detailing the thermodynamic properties of the species. A visual of what this looks like in Chemkin is given in Figure 6.1.

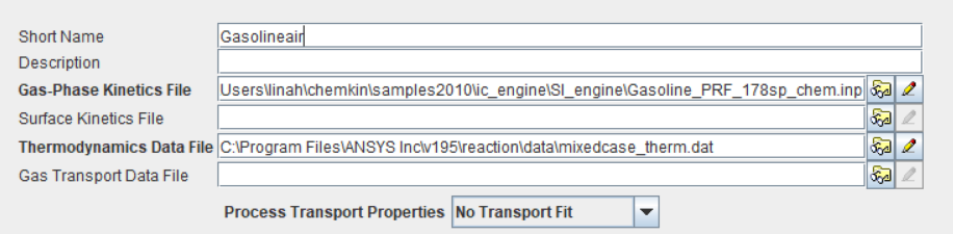

Figure 6.1: Visual of the fuel specification in Chemkin.

The gas-phase kinetics file contains information on the intermediate reactions occurring during combustion. Each relevant reaction equation is given, together with the corresponding Arrhenius rate coefficients A_a and β, and activation energy E_a. The Arrhenius equation used by Chemkin is given in Equation 6.1 [39, p.25] and is used to compute the forward rate constant k_+. The rate constant k_+ determines how much of each species is present at a specific point in time. For iso-octane (used to model gasoline) and hydrogen, the gas-phase kinetics file is already given in Chemkin. For Avgas, it is not. For the scope of this research, it is assumed that the results for iso-octane are representative for the results of Avgas.

$$k_+ = A_a T^{\beta} \exp \frac{-E_a}{RT} \tag{6.1}$$

The thermodynamic properties file consists of data used to compute the heat capacity, enthalpy and entropy of the species. These properties are determined using the NASA polynomials, given in Equations 6.2 through 6.4. Here, C_p is the heat capacity at constant pressure, H is the enthalpy, S is the entropy and a_1 to a_7 are the NASA polynomial coefficients. For each species, the range of thermodynamic properties is split into two parts, a low temperature part and a high temperature part. For each species, the reference enthalpy, reference entropy, the temperature ranges for the low and high part and the 7 NASA polynomial coefficients for both the low and high part are provided. These are then used to calculate the thermodynamic properties. The required values for a large range of species are already provided by Chemkin.

$$C_p = R\left(a_1 + a_2 T + a_3 T^2 + a_4 T^3 + a_5 T^4\right) \tag{6.2}$$

$$H = RT\left(a_1 + \frac{a_2 T}{2} + \frac{a_3 T^2}{3} + \frac{a_4 T^3}{4} + \frac{a_5 T^4}{5} + \frac{a_6}{T}\right) \tag{6.3}$$

$$S = R\left(a_1 \ln T + a_2 T + \frac{a_3 T^2}{2} + \frac{a_4 T^3}{3} + \frac{a_5 T^4}{4} + a_7\right) \tag{6.4}$$

6.2. Physical Properties of the Engine

A number of properties are required by Chemkin to model the physical properties of the engine. These are used to determine the volume inside the combustion chamber. The piston offset (the offset of point B in Figure 6.3 from the centre of the piston) is neglected in this research, but can be specified in Chemkin. A visual of the physical property input in Chemkin is given in Figure 6.2.

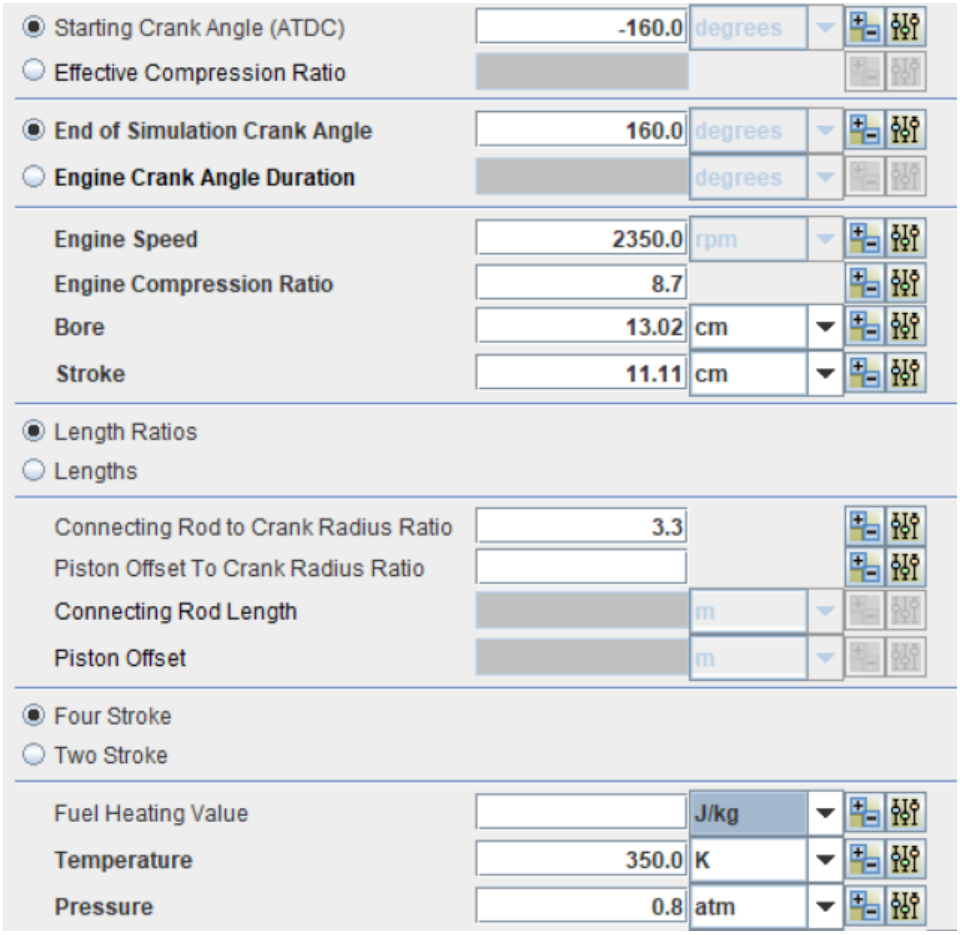

Figure 6.2: Visual of the engine lay-out specification in Chemkin.

The volume at a specific point in time is determined by computing the volume as a function of the crank angle. In Figure 6.3 a schematic of the cylinder and piston is given. The total cylinder volume is given in Equation 6.5 and the volume at TDC is the clearance volume. L_A is the crank arm radius, which is equal to half the stroke, and D is the bore. The clearance volume can be found using Equation 6.6, where CR is the compression ratio.

$$V_0 = \pi \left(\frac{D}{2}\right)^2 2L_A + V_{clear} \tag{6.5}$$

$$CR = \frac{V_0}{V_{clear}} \tag{6.6}$$

The height below the piston (the horizontal distance between point A and point B) can be found using Equation 6.7, after which the height above the piston can be computed using Equation 6.8. Multiplying the height above the piston with the cylinder bore and performing some mathematical computations gives an expression for the cylinder volume as a function of crank angle as given in Equation 6.9, where R_C is the ratio of the connecting rod length L_C to the crank arm radius L_A.

$$d_{A,B} = \sqrt{L_C^2 - L_A^2 \sin^2\theta} \pm \sqrt{L_A^2 - L_A^2 \sin^2\theta} \tag{6.7}$$

$$d_{cyl} = (L_A + L_C) - d_{A,B} \tag{6.8}$$

$$\frac{V}{V_{clear}} = 1 + \frac{CR+1}{2}\left(R_C + 1 - \cos\theta - \sqrt{R_C^2 - \sin^2\theta}\right) \tag{6.9}$$

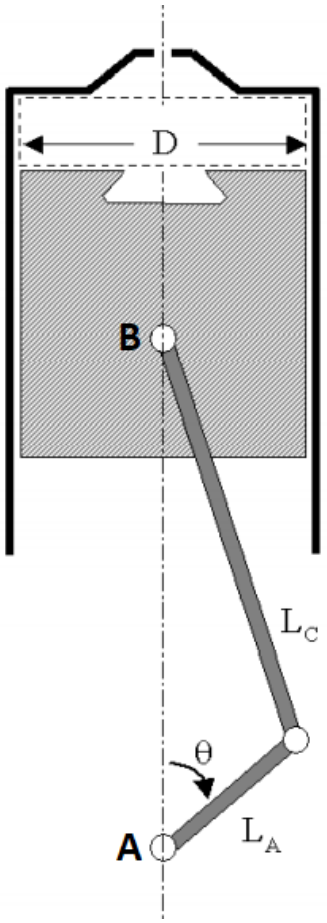

Figure 6.3: Schematic of the piston.

The timing for Inlet Valve Closed (IVC) and Exhaust Valve Opened (EVO) are used to determine the start and the end of the simulation in Chemkin.

6.3. Operating Conditions

The operating conditions of the engine are defined in Chemkin by the engine speed, the pressure and temperature before compression and the equivalence ratio. The engine speed is used to convert dependencies on crank angle to dependencies on time. Part of the operating conditions are already input in Chemkin in Figure 6.2, while a visual of the input of the equivalence ratio is given in Figure 6.4.

Figure 6.4: Visual of the input of the equivalence ratio in Chemkin.

It is assumed that the gases present before compression are all fresh fuel-air mixture (so no residual gases). With a specified pressure and temperature and a known volume, the amount of fuel-air mixture can be computed using the ideal gas law given in Equation 6.10, where n is the number of moles present and R the universal gas constant. With the amount of fuel-air known, the amount of fuel can be determined using the equivalence ratio. The consequences of these assumptions are elaborated on in Section 6.7.

$$pV = nRT \tag{6.10}$$

The pressure and temperature before compression, together with the volume, give the starting conditions for the compression phase. The compression (and expansion) phase is governed by the first law of thermodynamics given in Equation 6.11, where $C_v dT$ is equal to the change in internal energy, dQ_{loss} is equal to the change in heat and pdV is equal to the change in work. The change in temperature can be computed, and can then be used to compute the change in pressure using the ideal gas law.

$$C_v dT = -dQ_{loss} - pdV \tag{6.11}$$

In Figure 6.5, a flowchart is given detailing the calculation process of Chemkin during the compression and expansion phases. The calculation of the convective heat loss is further elaborated upon in Section 6.4.

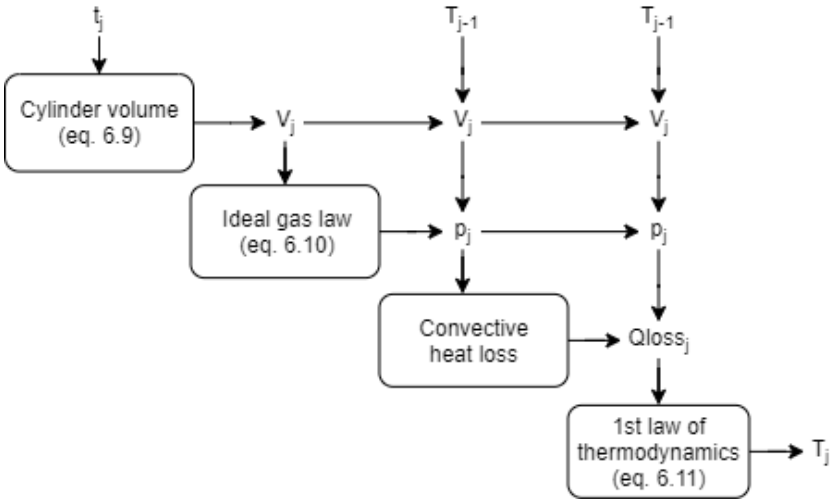

Figure 6.5: Flowchart of the compression and expansion phases in Chemkin.

6.4. Heat Transfer Parameters

The heat loss is part of the compression, the expansion and the combustion phase. The flowchart for the heat loss computation in Chemkin is given in Figure 6.6.

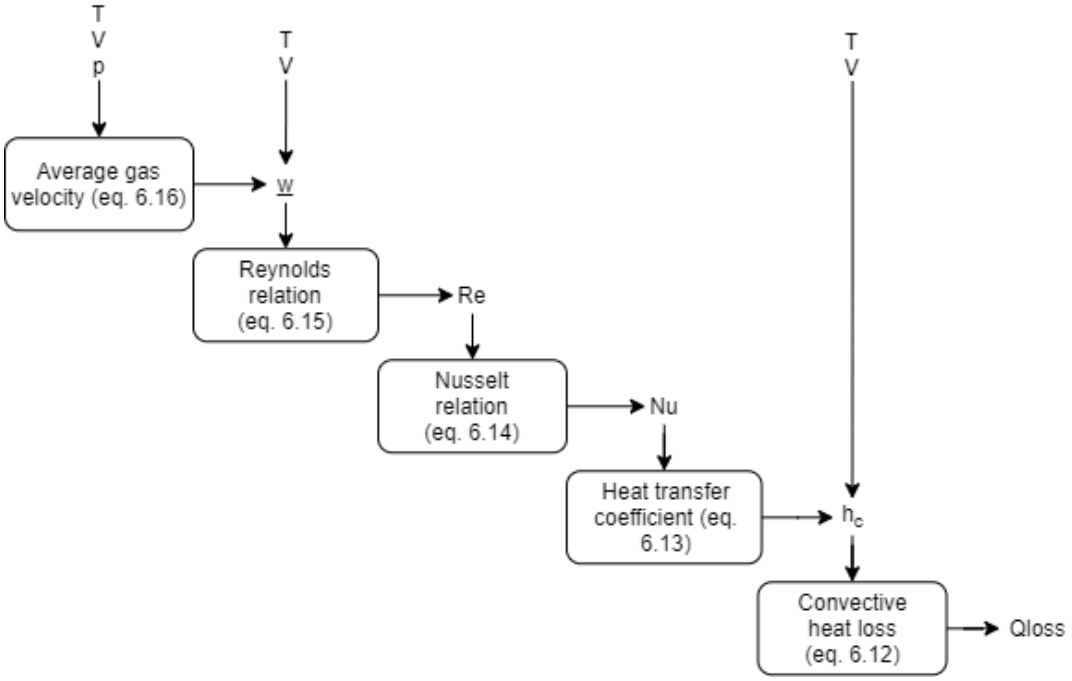

Figure 6.6: Flowchart of the heat loss computation in Chemkin.

The heat transfer is governed by the convective heat transfer relation given in Equation 6.12. h_c is the heat transfer coefficient, A is the area for which heat transfer is taking place and T is the temperature of the gases inside the cylinder. The area is computed by taking the sum of the piston head area, the cylinder head area, and the height above the piston multiplied with the piston circumference. The wall temperature is constant and specified by the user.

$$Q_{loss} = h_c A (T - T_w) \tag{6.12}$$

The heat transfer coefficient can be determined in multiple ways. Either a constant heat transfer coefficient can be used, or a correlation for the heat transfer coefficient. As the heat transfer coefficient is neither known nor constant, the correlation is used. To compute the heat transfer coefficient, the Nusselt number is used. The Nusselt number is a dimensionless number and indicates the ratio of the convective heat transfer to the conductive heat transfer as given in Equation 6.13, where λ is the gas conductivity. With a known Nusselt number and conductivity, the convective heat transfer coefficient can be computed.

To compute the Nusselt number, the Reynolds and Prandtl numbers are used as shown in Equation 6.14, where a, b and c are user specified constants. The Reynolds number is the ratio of inertial forces to viscous forces, and governs flow patterns. The Prandtl number is the ratio of momentum diffusivity to thermal diffusivity. For low Prandtl numbers, momentum diffusivity dominates and hence convection is dominant. For high Prandtl numbers, conduction is dominant. For the Prandtl number, a constant value can be specified. The standard value for air is 0.7.

$$Nu = \frac{h_c D}{\lambda} \tag{6.13}$$

$$Nu = a Re^b Pr^c \tag{6.14}$$

Of the options in Chemkin, the Woschni correlation gives the most accurate results for the Reynolds number [40]. Woschni relates the Reynolds number to the average cylinder gas velocity $\bar{w}$, as given in Equation 6.15, with ρ the density and μ the viscosity. Equation 6.16 gives the relation proposed by Woschni to find the average cylinder gas velocity.

The Woschni correlation is developed specifically for piston engines, and aims to take into account both convection due to the piston motion and convection due to combustion [41]. It assumes the average cylinder gas velocity $\bar{w}$ consists of two parts: the velocity caused by the piston motion and an additional gas velocity due to combustion. Empirical relations are established to determine both. In Equation 6.16, the first term is the velocity caused by the piston motion. It consists of two parts, the average piston velocity $\bar{S}_p$ multiplied with a user specified constant C_{11}, and the swirl velocity induced by the piston motion (v_{swirl}) multiplied with a user specified constant C_{12}.

The second term is the additional gas velocity due to combustion. The additional gas velocity is related to the temperature increase compared to a motored engine (which is rewritten using the ideal gas law to give a dependency on volume, which is known) through the user specified constant C_2. $p_{motored}$ is the motored pressure, the pressure at that specific point in time if isentropic compression and expansion would take place, given by Equation 6.17. Here, γ is the specific heat ratio of air, which is computed using the aforementioned NASA polynomials.

$$Re = \frac{D \bar{w} \rho}{\mu} \tag{6.15}$$

$$\bar{w} = \left(C_{11} + C_{12} \frac{v_{swirl}}{\bar{S}_p} \right) \bar{S}_p + C_2 \frac{V T_0}{p_0 V_0} \left(p - p_{motored} \right) \tag{6.16}$$

$$p_{motored} = p_0 \left(\frac{V_0}{V} \right)^{\gamma} \tag{6.17}$$

The constants C_{11}, C_{12} and C_2 can be specified separately for each phase (compression, combustion, expansion), but literature suggests a constant value for each of these phases [41]. Figure 6.7 gives a visualisation of the input of the heat transfer coefficients in Chemkin.

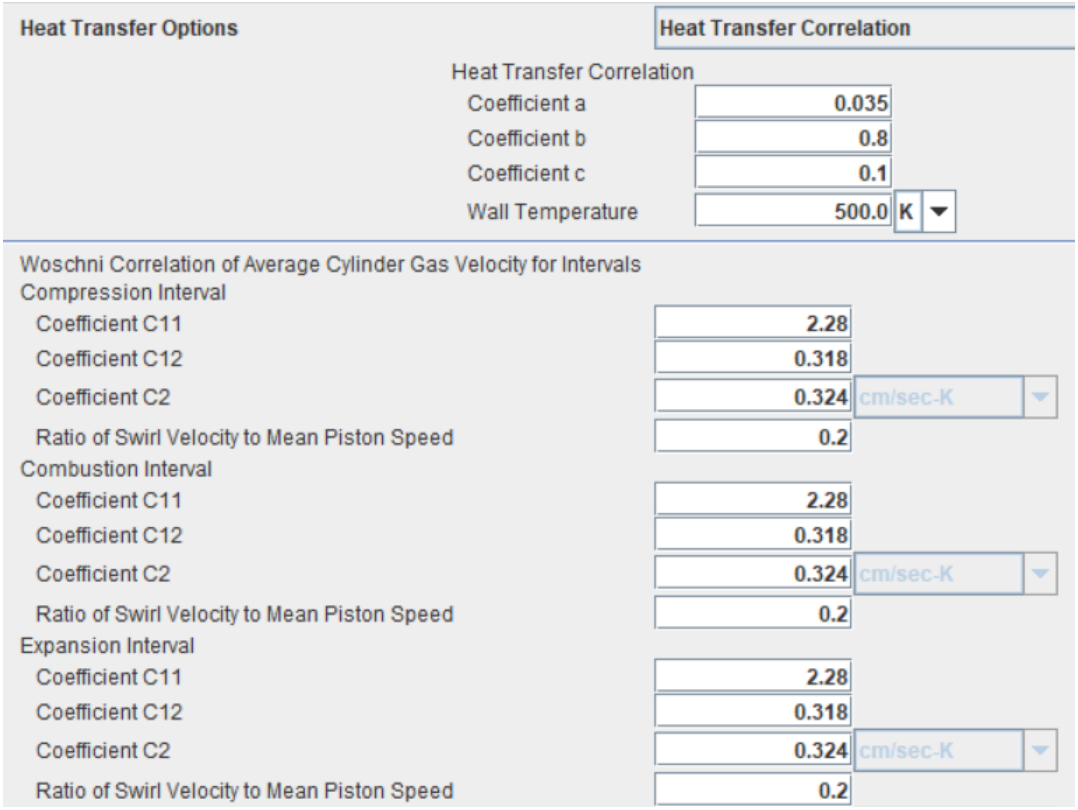

Figure 6.7: Visual of the heat transfer coefficient input in Chemkin.

6.5. Combustion Parameters and Mechanisms

The combustion chamber is divided into two zones: the unburnt zone and the burnt zone. Mass flows from the unburnt zone to the burnt zone through the flame front. The burn profile determines how the mass is divided between the unburnt zone and the burnt zone at each specific point in time. The burn profile can either be manually specified, or the Wiebe function can be used, given in Equation 6.18.

The Wiebe function is developed with the idea that, for engineering purposes, the details of the chemical kinetics of all the reactions taking place inside the piston engine can be replaced with a general reaction rate equation [42]. This general reaction rate equation is derived from the reaction rates of the main reactants inside the combustion chamber. A number of user specified constants (which are to be optimised) are introduced, b_W and n_W, which determine the shape of the Wiebe function. θ_0 is the start of combustion angle relative to TDC and $\Delta\theta$ is the burn duration. The Wiebe function is applicable to diesel and spark ignition engines with different fuel introduction techniques. A visualisation of the inputs of the Wiebe function parameters in Chemkin is given in Figure 6.8.

$$W_b = 1 - \exp\left[-b_W\left(\frac{\theta-\theta_0}{\Delta\theta}\right)^{n_W+1}\right] \tag{6.18}$$

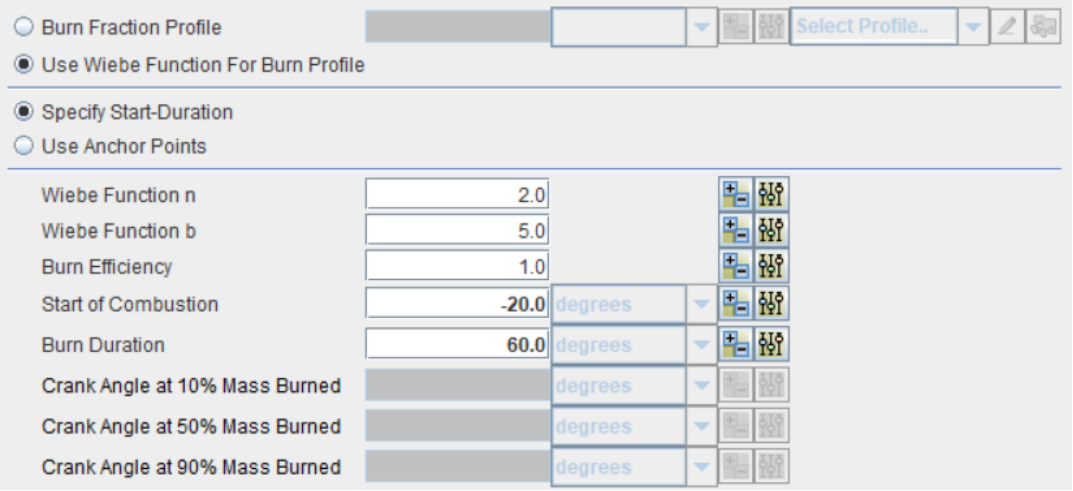

Figure 6.8: Visual of the Wiebe function specification in Chemkin.

The Lycoming engine currently has a fixed spark timing of 20° bTDC, but the goal is to be able to vary this spark timing.

No heat transfer takes place between the burnt zone and the unburnt zone. All mass leaving the unburnt zone enters the burnt zone. The mass of the burnt zone for time step $j+1$ is calculated using Equation 6.19. The mass of the unburnt zone is then the mass of the burnt zone subtracted from the total mass.

$$m_{b,j+1} = m_{total} W_{b,j+1} \tag{6.19}$$

As mass goes from the unburnt zone to the burnt zone, it passes through the flame front where combustion takes place. This combustion changes the composition, temperature and pressure of the combustion chamber. The burnt zone expands, compressing the unburnt zone and changing its temperature according to Equation 6.20.

$$T_{u,j+1} = T_{u,j} \left(\frac{p_j}{p_{j+1}} \right)^{\frac{1-\gamma}{\gamma}} \tag{6.20}$$

As the pressure is assumed to be homogeneous, the pressure of the burnt zone and the unburnt zone are equal to one another. To compute the pressure, first the temperature of the burnt zone needs to be found using Equation 6.21. The left-hand-side of the equation is the change in internal energy. The first term on the right-hand-side is the change in internal energy due to work, the second term is the change due to mass entering the burnt zone. The third term is due to chemical reactions taking place in the burnt zone and the last term is the heat loss. The enthalpy of the incoming mass, h_{in}, is determined at the adiabatic flame temperature.

$$m_{b,j+1} C_{p,b} \frac{T_{b,j+1} - T_{b,j}}{\Delta t} = -p_{j+1} \frac{dV}{dt} + m_{total} \frac{dW_b}{dt} (h_{in} - h_b) - \dot{\omega} h_b - \dot{Q}_{loss} \tag{6.21}$$

In parallel, the volume of the unburnt zone can be computed using Equation 6.22, which is subtracted from the total volume to find the volume of the burnt zone. The volume of the burnt zone is then used together with the temperature of the burnt zone to find the pressure in Equation 6.23. Mm is the average molar mass of the unburnt and burnt species respectively.

$$V_{u,j+1} = \frac{m_{u,j+1} R T_{u,j+1}}{p_{j+1} M m_u} \tag{6.22}$$

$$p_{j+1} = \frac{m_{b,j+1} R T_{b,j+1}}{V_{b,j+1} M m_b}. \tag{6.23}$$

A flowchart of the computations during the combustion phase is given in Figure 6.9. It includes an iterative loop, where the combustion chamber pressure is fed back into the loop. The flowchart of the computation of the burnt zone temperature using Equation 6.21 is given in Figure 6.10. The chemical kinetics are further elaborated upon below. The chemical kinetics and the subsequent enthalpy of the burnt zone are dependent on the temperature of the burnt zone. At this point, it is unknown whether an iterative loop is used or the temperature of the burnt zone of the last time step is used.

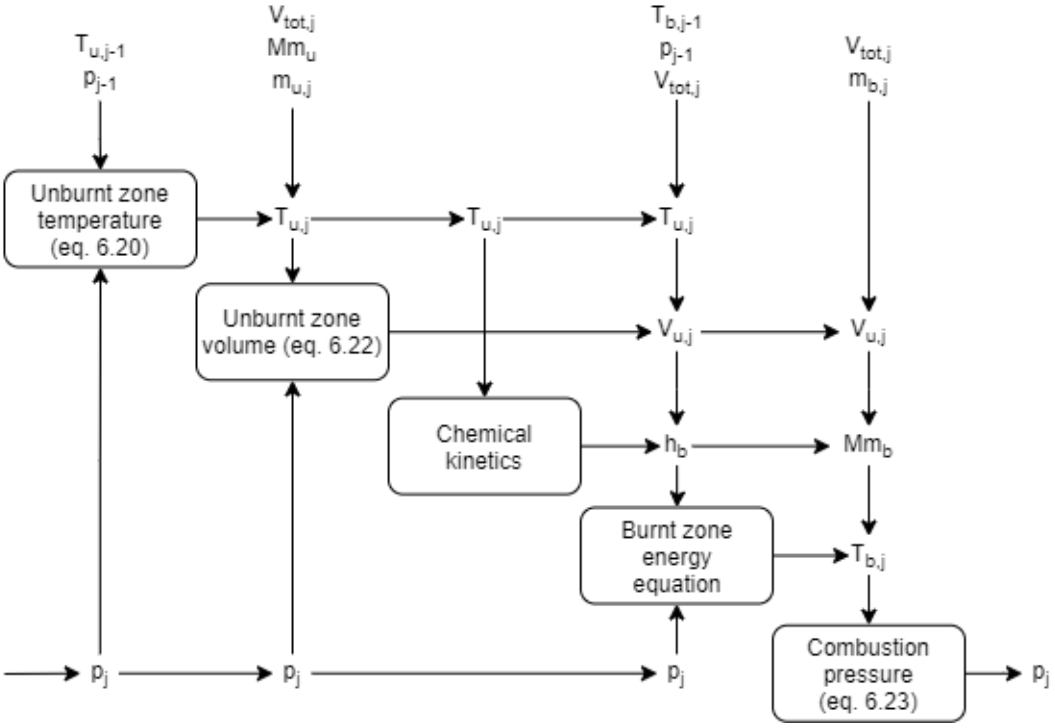

Figure 6.9: Flowchart of the combustion phase in Chemkin.

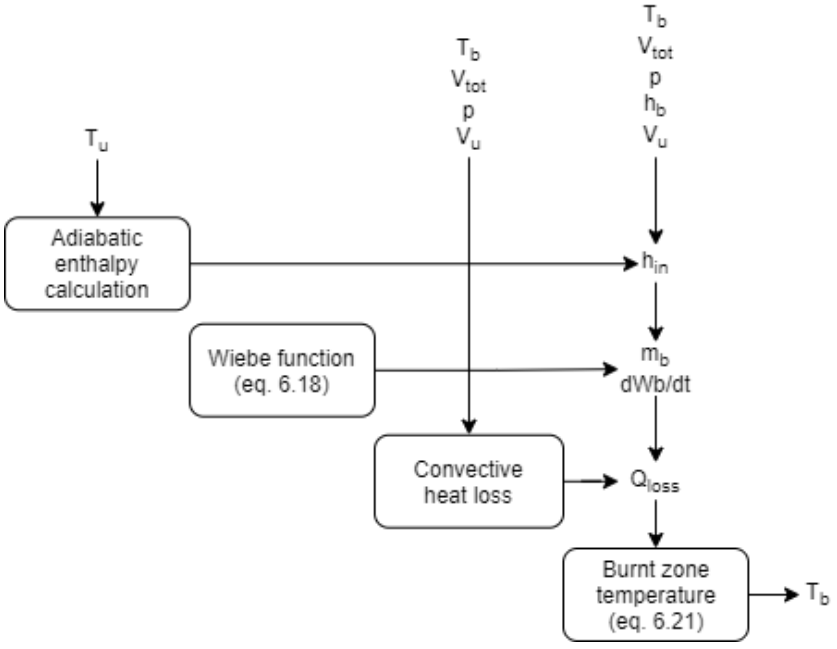

Figure 6.10: Flowchart of the burnt zone temperature computation in Chemkin.

To find the molar mass and the enthalpy, the composition of the unburnt zone and the burnt zone must be known. The unburnt zone consists of air and fuel. The composition of the mass entering the burnt zone (after going through combustion) is determined using chemical equilibrium. In Equation 6.24 a generic reaction equation is given, with σ the stoichiometric molar ratio. At chemical equilibrium, the forward and reverse reaction rates are equal to one another, as represented in Equation 6.25.

$$\sigma_1 Y_1 + \sigma_2 Y_2 \rightleftharpoons \sigma_3 Y_3 + \sigma_4 Y_4 \tag{6.24}$$

$$k_+ Y_1^{\sigma_1} Y_2^{\sigma_2} = k_- Y_3^{\sigma_3} Y_4^{\sigma_4} \tag{6.25}$$

The forward rate constant is determined using the Arrhenius equation as given in Section 6.1. The reverse rate constant can be determined using the equilibrium constant, which can be determined using Equation 6.26. Here, ΔS and ΔH are the change in entropy and enthalpy respectively, when passing completely from reactants to products.

$$K_c = \frac{k_+}{k_-} = \exp\left[\frac{\Delta S}{R} - \frac{\Delta H}{RT}\right]\left[\frac{p_{atm}}{RT}\right]^{\sigma_3+\sigma_4-(\sigma_1+\sigma_2)} \tag{6.26}$$

The flowchart of the computation of the molar mass and enthalpy is given in Figure 6.11. The reaction rate is dependent on the enthalpy of the burnt zone, which is in turn dependent on the reaction rate. Therefore an iterative loop is constructed, where the enthalpy of the burnt zone is fed back into the loop.

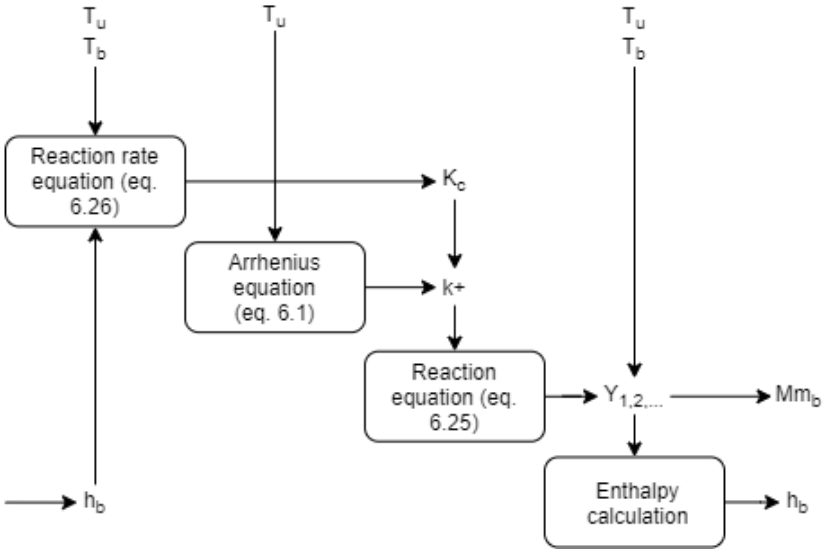

Figure 6.11: Flowchart of the molar mass and enthalpy computation in Chemkin.

The temperature of the gas passing from the unburnt zone to the burnt zone is equal to the adiabatic flame temperature, which is determined using Equation 6.27.

$$\sum H_{react} = \sum H_{prod} \tag{6.27}$$

6.6. Main Takeaways

The compression and expansion phase are governed by the ideal gas law and the first law of thermodynamics, given in Equations 6.10 and 6.11 respectively.

During the compression, expansion and combustion phases, heat transfer occurs. The heat transfer parameters are computed using a relation between the Nusselt number, Reynolds number and Prandtl number as given in Equation 6.14. The Reynolds number is computed using the average cylinder gas velocity as proposed by Woschni, given in Equation 6.15.

The mass transfer from the unburnt to the burnt zone during the combustion phase is governed by the Wiebe function, as given in Equation 6.18. The species entering the burnt zone are determined using equilibrium kinetics, where the forward and reverse reaction rates are equal to one another. The temperature of the species entering the burnt zone are at adiabatic flame temperature. As combustion takes place, the pressure increases, which in turn leads to an increase in temperature of the unburnt zone as given by Equation 6.20. Based on the temperature of the unburnt zone, the volume of the unburnt zone can be computed, which can then be used to compute the volume of the burnt zone.

Using the Wiebe function, and the enthalpy of the burnt zone and the incoming species (determined at adiabatic flame temperature), the new temperature of the burnt zone can be computed using Equation 6.21. With the new temperature and the volume of the burnt zone, the overall pressure can be computed using the ideal gas law as given in Equation 6.23.

The goal of using Chemkin as a tool is to make predictions on the peak pressure and peak temperature for specific conditions for both Avgas and hydrogen. Therefore, the pressure and temperature profiles, as well as the power are considered in this study.

6.7. Assumptions

Chemkin makes use of a number of assumptions to simplify the computations. In addition, some physical phenomena that are expected to occur in the actual engine, are not taken into account. In this section, these assumptions are identified and the effect of these assumptions is explained. The assumptions are divided into five categories. Section 6.7.1 explains the assumptions regarding the fuel used in the Chemkin simulation and Section 6.7.2 assesses the effects of the simplifications with regards to the thermodynamic properties. Section 6.7.3 explains the assumptions made regarding the combustion phase, Section 6.7.4 explains the simplifications regarding the heat transfer and Section 6.7.5 details the physical phenomena of a real engine which are not modelled in Chemkin. Finally, in Section 6.7.6 the main takeaways of this section are presented.

6.7.1. Fuel

Instead of Avgas, iso-octane is used in Chemkin. Both Avgas (rating 100LL) and iso-octane have an octane number of 100. Iso-octane is a component of Avgas, but Avgas also contains other hydrocarbons and tetraethyllead. It can be seen as gasoline with added tetraethyllead. When comparing the combustion behaviour of iso-octane with Avgas, some differences can be found. An overview of the basic fuel properties is given in Table 6.1. The higher stoichiometric air-fuel ratio for iso-octane combined with its higher Lower Heating Value leads to a 2.3% decrease in energy release during stoichiometric combustion compared to Avgas. This means that the heat release in Chemkin underestimates the real situation.

Avgas shows a lower burn duration (by approximately 13%) and subsequently a higher peak pressure compared to iso-octane [43], corresponding to behaviour found in Section 7.5.3. Decreasing the burn duration and the equivalence ratio when using iso-octane in the simulation should account for the differences between Avgas and iso-octane.

Table 6.1: Properties of Avgas and iso-octane. a: Values obtained from Coordinating Research Council [44]. b: Values obtained from J. Serras Pereira et al. [43].

	Avgas$^{(a)}$	**Iso-octane**$^{(b)}$
Molar mass [g/mol]	100 - 105$^{(b)}$	114.3
Density [kg/m^3]	698	690
Autoignition temperature [K]	716	683
Stoichiometric AFR	14.6$^{(b)}$	15.1
Lower Heating Value [MJ/kg]	44.15	44.6
Explosion limit [vol%]	1.2 - 7	1 - 6

Chemkin assumes pure hydrogen, but one of the advantages of hydrogen combustion compared to hydrogen fuel cells is the possibility to use hydrogen with lower purity. The main contaminants found in hydrogen are CO, CO_2, H_2S, NH_3, organosulfurs and hydrocarbons [45]. Of these contaminants, only H_2S and hydrocarbons are flammable, and both decrease the energy content and hence the temperature, pressure and power compared to the predictions by Chemkin. The effect on the thermodynamic properties is assumed negligible.

The model used in Chemkin assumes a homogeneous fuel-air mixture from the start of compression. For the unmodified Lycoming engine this is relatively accurate, as it has a port fuel injection system, although the mixture will never be 100% homogeneous. However, once modifications to the engine have been made and a direct injection system is installed, the homogeneity decreases considerably.

From Figure 6.12, it is clear that the value for heat capacity of air lies between that of both fuel-air mixtures, leading to pressure and temperature results for the compression phase between those of Avgas and hydrogen as given in Section 7.2. This gives a slightly higher pressure and temperature than for Avgas during compression, but a slightly lower pressure and temperature than for hydrogen. However, the greatest effect is expected after the compression phase, when injection takes place. During Avgas direct injection, cooling takes place as the Avgas evaporates. Additionally, the total amount of combustable mixture increases. The difference between port fuel injection and direct injection is even higher for hydrogen, as it takes up a large portion of the total cylinder volume when already present at the beginning of compression. Due to the increase in pressure, there is an increase in temperature. The power output is expected to increase for both fuels when using direct injection compared to the Chemkin model as there is more combustable mixture present, with a larger increase expected for hydrogen.

To overcome this effect, the pressure before compression is increased. This allows for more combustable mixture to be present, however this also increases the pressure throughout the compression phase, in turn influencing the peak pressure and the power. A compromise can be found, where the combination of the higher pressure during compression and the higher amount of combustable mixture together give an accurate peak pressure and power result.

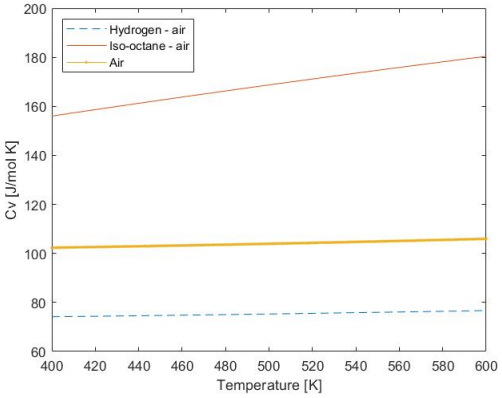

Figure 6.12: Heat capacity of air and the fuel-air mixtures.

When using direct injection, the fuel-air mixture is not homogeneous. This leads to locations in the combustion chamber with different equivalence ratios. A decrease in homogeneity leads to a decrease in pressure, temperature and power [46, p.186-187], and possibly could be accounted for by decreasing the equivalence ratio. This does however influence the emissions. As hydrogen is highly dissipative, the homogeneity is lower for Avgas than for hydrogen.

6.7.2. THERMODYNAMIC PROPERTIES

The NASA polynomials are used to find the temperature dependent heat capacity and enthalpy of each species. The values for each species are found by curve fitting to experimental data. As no experiment is the same, this behaviour could deviate from the behaviour found in the engine. However, this effect is deemed negligible.

The viscosity of each species is found using Sutherland's law, given in Equation 6.28, where S_T is the Sutherland temperature and μ_0 is a known viscosity at reference temperature T_0. Sutherland's law is fairly accurate, with a 2% error for a temperature range of 200 - 1500 K for the most common gases [47, p.28]. The viscosity is used to compute the Reynolds number, which is then used for the heat transfer coefficient. As the heat transfer is not a major player during compression, combustion and expansion, the effect of a few percent error is deemed negligible.

The Sutherland temperature for air is assumed to be valid for the fuel-air mixture and the combustion products. Compared to the other gases present, air has a relatively high viscosity [48], except for gaseous water. This means that during the compression phase the viscosity is slightly overestimated, leading to a lower Reynolds number. This lower Reynolds number then leads to a lower heat transfer coefficient, and a lower heat loss. During the expansion phase, the viscosity is underestimated (with 27% for iso-octane combustion and 41.5% for hydrogen combustion), leading to a higher heat transfer coefficient and a higher heat loss. The effect during expansion is higher than during compression and overall overestimation of the heat loss is expected. This can be accounted for by decreasing the heat transfer coefficient b as elaborated on in Section 6.7.4.

$$\mu = \mu_0 \left(\frac{T}{T_0} \right)^{3/2} \frac{T_0 + S_T}{T + S_T} \tag{6.28}$$

The ideal gas law is used to find the relation between the temperature, volume and pressure inside the cylinder. This assumption does not hold for real gases. Brown et al. [49] explains that two of the main assumptions of the ideal gas law do not hold under high pressures: the assumption that gas particles have zero volume and the assumption that there are no intermolecular forces. As the temperature decreases, the deviation from the ideal gas law increases. The deviation from the ideal gas law for some common gases is given in Figure 6.13. For N_2, O_2, CO_2, H_2O and octane the pressure computed with the ideal gas law is an overestimation, while for H_2 it is an underestimation [50]. Overall, this means that the pressure throughout the whole simulation is overestimated.

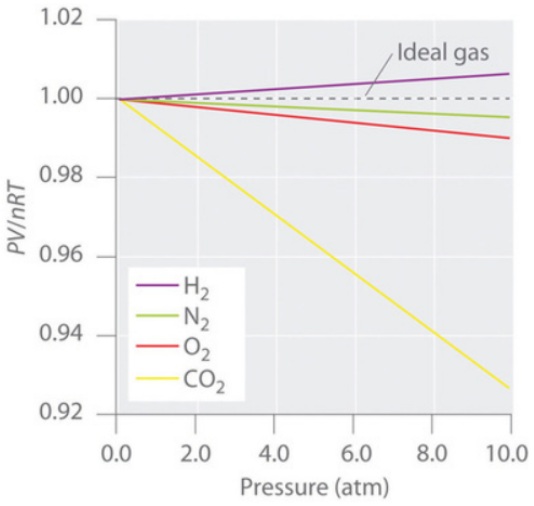

Figure 6.13: Deviation from the ideal gas law for common gases [49].

6.7.3. COMBUSTION MECHANISM

Chemkin assumes equilibrium chemistry to determine the species present in the unburnt and burnt zone. At chemical equilibrium, the forward and reverse reaction rates are equal to one another and the concentration of both reactants and products does not change. This equilibrium does not represent real life conditions. As the equilibrium chemistry is usually a part of a computer model modelling different aspects of combustion, the effect of equilibrium chemistry alone on the pressure, temperature and performance is not clear. However, C.H. Marchi and L.K. Araki [51] suggest that non-equilibrium chemistry only becomes relevant at very high temperatures as found in rocket engines. Furthermore, it is generally accepted that NOx formation is not accurately represented by equilibrium chemistry [52] [53] [54]. Although the effect of equilibrium chemistry on the emissions might be significant, the effect on the pressure, temperature and power inside the cylinder is deemed negligible.

The burn profile is determined by the Wiebe function as given in Section 6.5. For each combustion condition, the parameters of the Wiebe function should be optimised to match the actual burn profile. However, for the Lycoming engine, the actual burn profile is not available. Either experiments must be performed to obtain the burn profile, or an empirical method can be used to approximate the Wiebe parameters.

For the burn duration from 0 - 90% and the Wiebe parameter n, correlations can be found. The most accurate as found by F. Bonatesta et al. [55] are given in Equations 6.29 and 6.30 respectively. Here, ρ_{ST} is the density when the spark is fired, θ_{ST} is the crank angle at which the spark is fired in °bTDC and x_r is the dilution mass fraction which can be calculated using Equation 6.31. Here, p_{exh} is the exhaust pressure which can be assumed to be equal to 1.5 atm, V_{EVC} is the cylinder volume at Exhaust Valve Closed, T_{exh} is the temperature of the exhaust gases, which can be approximated using Equation 6.32, and m_{total} is the total mass present in the cylinder. A maximum Wiebe parameter n error is found of 8%, while a maximum burn duration error is found of 13% with an average of 4.5% for a wide range of operating conditions [55].

$$\Delta\theta_{90} = 178\left(\frac{1}{\rho_{ST}}\right)^{0.34}\left(1-\frac{1.164}{\sqrt{\bar{S}_p}}\right)\left(\frac{1}{1-2.06x_r^{0.77}}\right)^{0.85}\left(0.00033\theta_{ST}^2-0.0263\theta_{ST}+1\right) \tag{6.29}$$

$$n+1 = 3.46\left(\frac{1}{\sqrt{\bar{S}_p}}\right)^{0.45}\left(\frac{1}{1+\sqrt{\theta_{ST}}}\right)^{-0.35}(1-1.28x_r) \tag{6.30}$$

$$x_r = \frac{p_{exh}V_{EVC}Mm}{RT_{exh}m_{total}} \tag{6.31}$$

$$T_{exh} = -2.537\cdot10^{-5}N^2+0.2523N+273.15 \tag{6.32}$$

The Wiebe parameter b can be assumed to be equal to 2.302 [56]. For a specific engine, this leads to an underestimation of the peak pressure of 19% [56], which must be accounted for with a safety factor.

6.7.4. HEAT TRANSFER

The two-zone model used in Chemkin assumes adiabatic combustion (with mass entering the burnt mass zone at adiabatic flame temperature) and no heat transfer between the two zones. In real life, there is heat transfer, both during combustion and between the two zones. This means that the mass entering the burnt zone does so at a lower temperature, and hence with lower enthalpy, decreasing the temperature of the burnt zone. Additionally, some of the heat of the burnt zone is transported to the unburnt zone, again decreasing the temperature of the burnt zone. This leads to a decrease in both the peak pressure and temperature for the actual engine.

The heat transfer to the walls of the combustion chamber is simplified. Heat transfer through radiation is neglected. Only convection is considered, with an estimate for the heat transfer coefficient. The heat transfer coefficient is estimated using the Nusselt number, which is in turn estimated using the Reynolds and Prandtl numbers and three user specified parameters as given by Equation 6.33. The Reynolds number is estimated using the Woschni correlation, based on the pressure, volume, swirl velocity and mean piston speed. In addition, it contains a number of constants which must be optimised to match the pressure and temperature profile of experiments. These constants, and those used to compute the Nusselt number, are assumed to be constant throughout the simulation. It is suggested that, to isolate the heat transfer and obtain the constants,

experimental data should be obtained without firing the spark plug and compared to the simulation data without heat release. By optimising the constants, some real life effects which are not directly taken into account in Chemkin can be indirectly incorporated, such as the quenching distance, the cooling of the engine, and the radiation.

$$Nu = aRe^b Pr^c \tag{6.33}$$

The Prandtl number is assumed to be constant, and equal to the standard value for air. It is the ratio of momentum diffusivity to thermal diffusivity, which are both dependent on temperature and pressure. For the temperature and pressure range relevant for the Lycoming engine, the Prandtl number for air varies between 0.7 and 0.74 [57]. In addition, the presence of other gases can change the Prandtl number. For the unburnt zone, the amount of gases present other than air is so small that the influence on the Prandtl number can be neglected. For the burnt zone, the presence of CO_2, H_2O and N_2 is dominant, with a Prandtl number of approximately 0.72 [58], 0.9 [59] and 0.7 [60] respectively. This gives a molar average Prandtl number of 0.73 for the products of iso-octane combustion and 0.77 for the products of hydrogen combustion. From Section 7.4 is it clear that these relatively minor changes in Prandtl number do not influence the power, pressure and temperature. Therefore, the assumption of a constant Prandtl number equal to the value of air holds.

6.7.5. COMPARISON TO A REAL ENGINE

Although the model in Chemkin takes into account heat losses, it does not take into account some other loss sources. In Figure 6.14 [61], typical engine losses for an engine at part load and an engine at full load are given. Three loss sources apart from thermal losses are given: exhaust chemical loss, caused by unburnt fuel leaving the engine, mechanical friction loss, caused by friction between moving parts of the engine and gas exchange loss, caused by the gas exchange process. The exhaust chemical loss and gas exchange loss lead to a decrease in heat release, which in turn leads to a decrease in pressure and a decrease in power. To account for this, the amount of fuel must increase (a higher equivalence ratio) to reach the same peak temperature, peak pressure and power. The mechanical friction loss however might lead to an increase in peak pressure while decreasing the power, as more force is needed to move the piston.

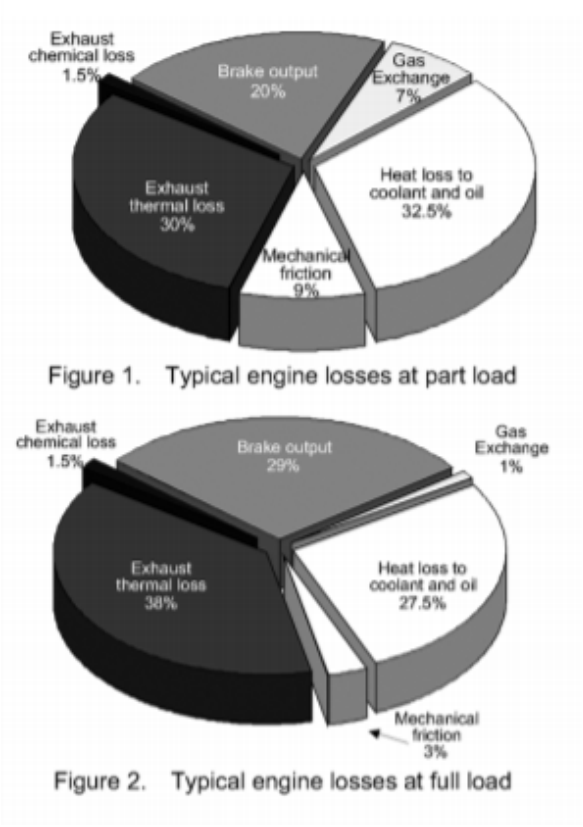

Figure 6.14: Typical engine losses for an engine at part load and full load [61].

The model in Chemkin only models one cylinder, while the Lycoming engine consists of four cylinders. To obtain the total power of the engine, the power of one cylinder cannot simply be multiplied by four. The main differences between a single cylinder engine and a four-cylinder engine lies within the mechanical losses, with a four-cylinder engine experiencing higher friction losses than a single cylinder engine.

As mentioned in Section 2.4, blowby takes places in an engine, more so for hydrogen than for Avgas. This is most prominent during compression and combustion and can reduce the amount of fuel-air mixture in the combustion chamber by 1% for gasoline [14, p.217]. The crankcase must be ventilated to make sure the pressure in the crankcase does not build up. The decrease in fuel-air mixture decreases the peak pressure, peak temperature and power and is expected to have a higher influence for hydrogen than for Avgas. This could be modelled in Chemkin by decreasing the pressure before compression and hence decreasing the amount of fuel-air mixture present in the cylinder.

In the Chemkin model, pre-ignition is currently not considered, however there is the option of modelling it. This means that there are no limits for the compression ratio and operating conditions. When operating below the real pre-ignition limit, pre-ignition should not occur and this assumption hence does not influence the peak temperature, peak pressure or power.

One of the parameters used in Chemkin is the start of combustion. For an actual piston engine, the parameter of interest is not the start of combustion, but the spark timing. The spark timing differs from the start of combustion with the ignition delay. The ignition delay is dependent on the engine, the fuel and the operating conditions. It is generally optimised for one operating condition, although it is also possible to have variable spark timing. The spark timing is optimised such that the expansion as a result of combustion does not happen too early as this hinders the compression stroke. The spark timing must not be too late, as the expansion as a result of combustion should push the piston down, and not lag behind. To accurately compare the predicted performance, pressure and temperature in Chemkin to the real engine, the ignition delay must be taken into account. A method of achieving this is by developing ignition delay correlations based on experimental data, similarly to Z. Zhao et al. [62].

6.7.6. Main Takeaways

To simplify the computations, a number of assumptions are made by Chemkin. The assumptions which are expected to have a significant influence on the peak pressure, peak temperature or power, and need to be validated, are given below.

- The use of iso-octane instead of Avgas: Chemkin uses iso-octane to model Avgas, iso-octane has a lower energy content;
- The use of pure hydrogen instead of contaminated hydrogen: Chemkin uses pure hydrogen to model hydrogen combustion, pure hydrogen has a higher energy content;
- Fuel present from the start of compression: Chemkin assumes that fuel is present throughout the simulation, this is not the case for direct injection. Especially for hydrogen combustion Chemkin underestimates the volumetric efficiency;
- A homogeneous fuel-air mixture: Chemkin assumes a homogeneous fuel-air mixture, this is especially not accurate for direct injection. A less homogeneous mixture leads to a decrease in pressure, temperature and power;
- Using air viscosity: Chemkin uses Sutherland's law with the Sutherland temperature set to the standard temperature for air for the whole simulation. This results in overestimation of the viscosity and subsequently an underestimation of the heat transfer coefficient;
- Using the ideal gas law: Chemkin uses the ideal gas law to relate pressure to temperature. At high pressures and temperatures, this assumption does not hold and leads to an overestimation of the pressure throughout the whole simulation;
- Using the Wiebe function: Chemkin uses the Wiebe function to specify the burn profile, which must be optimised for each engine, fuel and operating condition. Additionally, the ignition delay can be incorporated in the Wiebe function;
- Adiabatic combustion: Chemkin assumes adiabatic combustion and no heat transfer between the burnt and unburnt zone during combustion. The temperature of the burnt zone is thus overestimated;

- Convective heat transfer with the Woschni correlation: Chemkin uses convective heat transfer with the Woschni correlation, for which several parameters need to be optimised to also include other forms of heat transfer and cooling;
- Gas exchange loss and mechanical loss: Chemkin does not model the gas exchange loss and mechanical loss, although these losses can decrease the power significantly;
- Multiple cylinders: Chemkin only models one cylinder and multi-cylinder interference is hence not taken into account;
- Blowby: Chemkin does not consider blowby, while this is expected to reduce the amount of fuel-air mixture.

The significance of some of the effects modelled by Chemkin are further elaborated on in Chapter 7, while experiments to validate the effects of the assumptions are proposed in Chapter 9.

7
SENSITIVITY ANALYSIS OF CHEMKIN

A sensitivity study is performed to assess which parameters and assumptions have the highest impact on the results, and verify the working of Chemkin. This information is used in Chapter 9 to identify which experiments need to be performed to assure accurate results. Each input parameter is varied by 20%, unless specified otherwise. A value of 20% is chosen as this deviation would result in an engine with similar characteristics, with a range of operating conditions which falls within cruise conditions for this engine. For the heat transfer parameters and the burn profile, a standard range of values is unknown at this point. Therefore 20% is used for consistency with the other parameters.

The effect of the variation of the respective parameter on the power, peak pressure, peak temperature, P-V diagram and temperature profile is considered. The power is not directly given by Chemkin, but computed by taking the area in the P-V diagram to find the work, and dividing this by the time needed to complete four strokes. The results from Chemkin are compared to the expectations based on the mathematical background of Chemkin, and where applicable the expectations based on the physical knowledge of piston engines. The changes in input parameters can be subdivided into a number of categories: changing the engine, changing the fuel, changing the operating conditions, changing the heat transfer parameters and changing the burn profile.

Not all parameters could be varied by the same amount due to convergence issues. To be able to fairly compare the effects of the different parameters, all errors in power, peak pressure and peak temperature are normalised to a parameter change of 100%. This means that, if a parameter is changed by 20%, a power error of 2% is represented as 10%. As Chemkin is a numerical program, the results of the program can vary as the simulation parameters (such as time step or convergence criteria) change. It was found that this can lead to an error of up to 1.20% for the power, 0.30% for the peak pressure and 0.20% for the peak temperature. Normalising this as mentioned above gives an error of 6% for power, 1.50% for peak pressure and 1.0% for peak temperature. Any errors in power, peak pressure and temperature found below these values, are attributed to the simulation parameters, and thus not to the change in input parameter. In the results, these are denoted with an asterisk.

The remaining errors are divided into three categories: minor, moderate and significant. An error above 25% is seen as significant, an error above 10% for power and 5% for pressure and temperature is seen as moderate and a lower error is seen as minor. When there is a minor error when decreasing the parameter, while there is an error smaller than the convergence error when increasing the parameter, both errors are deemed negligible. The same is valid for the opposite, with a smaller than convergence error when decreasing the parameter and a minor error when increasing the parameter. These values are also denoted with an asterisk.

A brief overview of the results for the power, peak pressure and peak temperature is found in Figure 7.1, where the change in power, peak pressure and peak temperature is given when changing each parameter with 100%. The blue bar represents a decrease while the red bar represents an increase in the respective parameter. In the subsequent sections, each of the parameters is analysed and the change in power, peak pressure and peak temperature is explained. For each parameter, the changes in the equations governing the compression, combustion and expansion phase (Equations 6.10, 6.11, 6.21 and 6.23) and subsequent effects on the pressure, temperature and power are evaluated.

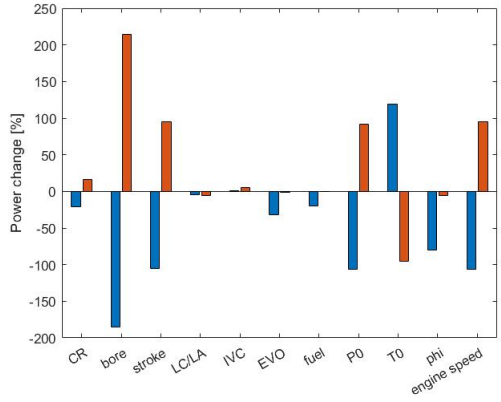

(a) Effect of the change in input parameters on the power (1).

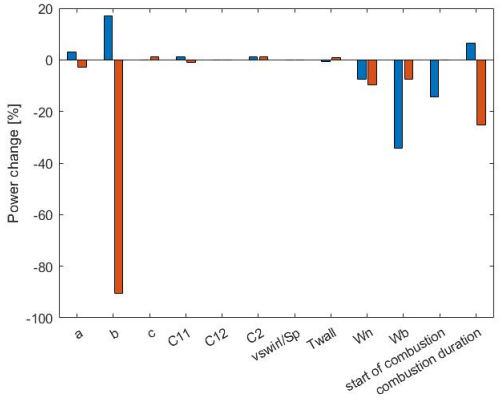

(b) Effect of the change in input parameters on the power (2).

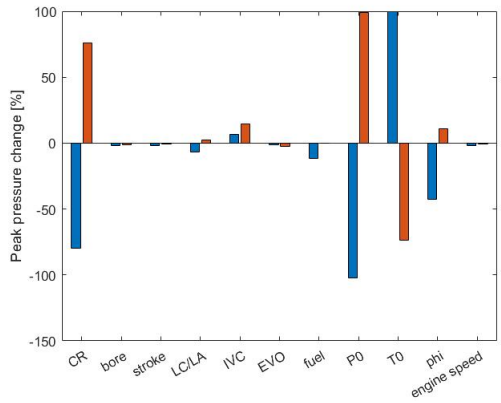

(c) Effect of the change in input parameters on the peak pressure (1).

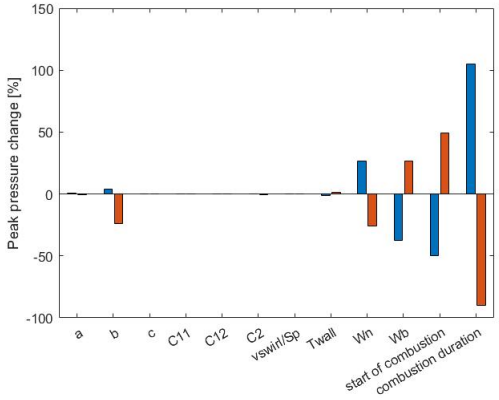

(d) Effect of the change in input parameters on the peak pressure (2).

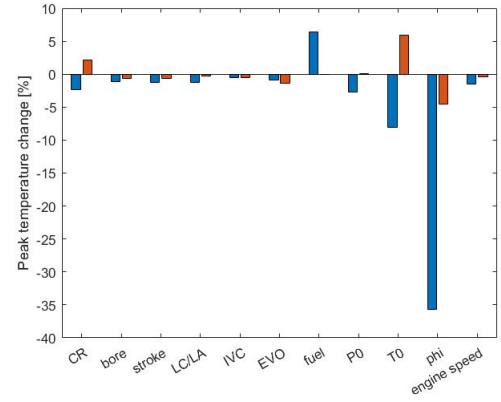

(e) Effect of the change in input parameters on the peak temperature (1).

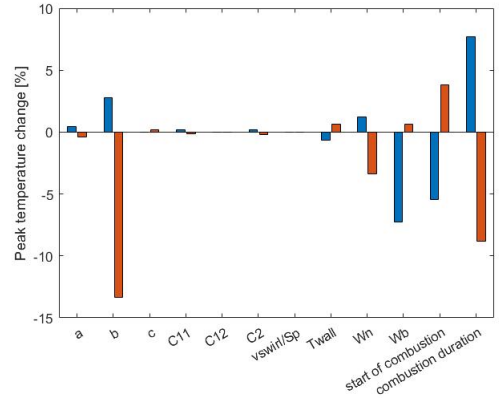

(f) Effect of the change in input parameters on the peak temperature (2).

Figure 7.1: Effect of the change in input parameters on the outputs of interest. The parameters are changed by 20% and normalised to 100%, with the blue bar giving the result for a decrease in input parameter and the red bar giving the result for an increase in input parameter.

7.1. CHANGING THE ENGINE

Six engine parameters can be changed: the compression ratio, the bore, the stroke, the connecting rod length, IVC and EVO. The standard values for these inputs are given in Table 7.1. Furthermore, when changing the engine parameters, the heat transfer parameters change, as these are optimised for one specific engine, operating on one specific fuel for one specific operating condition. These are covered in Section 7.4. When using the same engine, the compression ratio, bore, stroke and connecting rod length do not change. Changing these with 20% would result in a different engine with a similar power rating. IVC and EVO can change when altering the valve timing, which might be necessary in the future for smooth operation with hydrogen. A change of 20% is probably along the upper limit of the expected change in IVC and EVO.

Table 7.1: Standard physical property values.

	Compression ratio	**Bore [cm]**	**Stroke [cm]**	**Connecting rod length [cm]**	**IVC [°bTDC]**	**EVO [°aTDC]**
Value	8.7	13.02	11.11	18.33	160	160

7.1.1. COMPRESSION RATIO

$$pV = nRT \tag{7.1}$$

$$C_v dT = -dQ_{loss} - pdV \tag{7.2}$$

As the compression ratio increases, the ratio between the original volume and the clearance volume increases. As the bore and stroke do not change, this means the clearance volume decreases. With a decreased clearance volume, there is a decreased volume throughout the whole simulation. This means that the amount of fuel-air mixture ingested into the cylinder is smaller, as can be seen in Equation 7.1, where the orange symbols denote a decrease in the respective parameter. For the same volume, this thus gives a slightly lower value for the pressure. Then, for an increase in compression ratio, the volume reduces more, and thus the pressure increases more, as can be seen in Figure 7.2. The change in volume is constant, but the pressure increases as the compression phase proceeds. During the compression phase, the change in volume is negative, and an increase in pressure thus leads to an increase in temperature change, as can be seen in Equation 7.2. where the green symbols denote an increase in the respective parameter. This leads to an increase in absolute temperature, as can be seen in Figure 7.3.

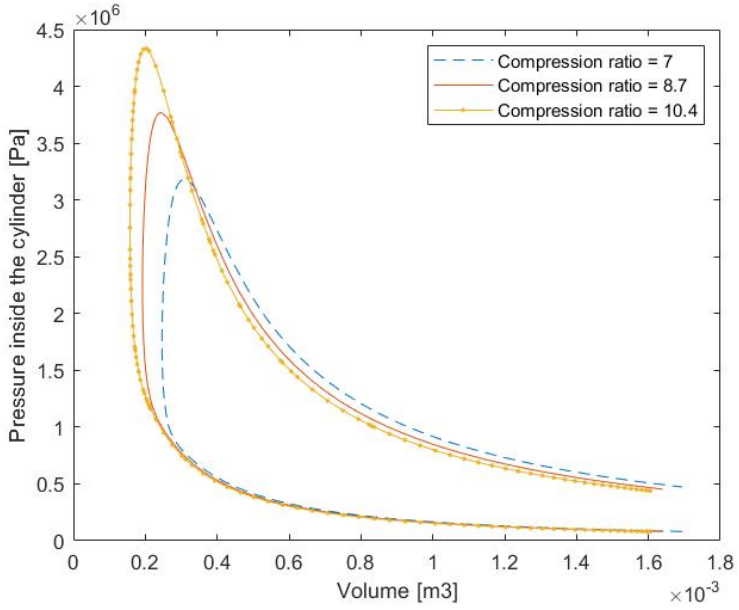

Figure 7.2: P-V diagram with varying compression ratio.

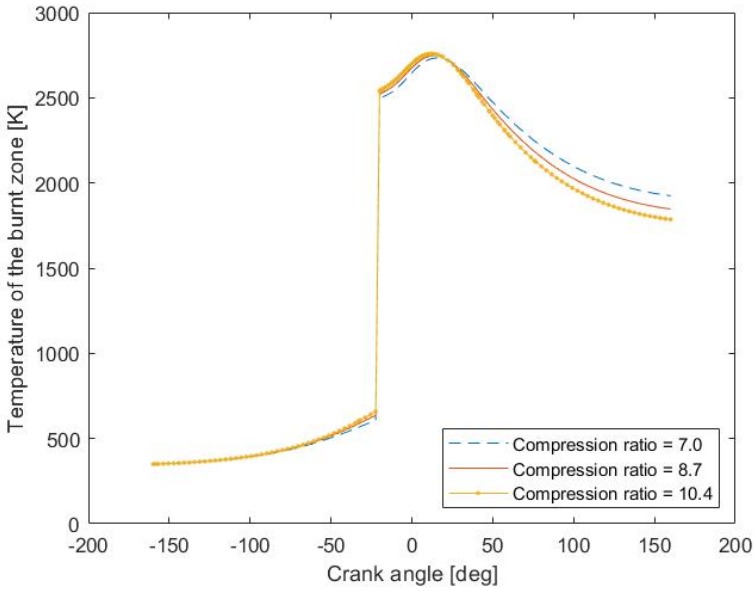

Figure 7.3: Burnt zone temperature profile with varying compression ratio.

$$m_{b,j+1} C_p \frac{T_{b,j+1} - T_{b,j}}{\Delta t} = -P_{j+1} \frac{dV}{dt} + m_{total} \frac{dW_b}{dt} (h_{in} - h_b) - \dot{\omega} h_b - \dot{Q}_{loss} \tag{7.3}$$

$$P_{j+1} = \frac{m_{b,j+1} R T_{b,j+1}}{V_{b,j+1} M m_b}. \tag{7.4}$$

The difference in pressure at the start of combustion is amplified during combustion, while the difference in temperature is not. As $\frac{dV}{dt}$ is negative before TDC, an increase in temperature due to the increase in pressure is expected. As the amount of fuel-air mixture ingested into the cylinder before compression is smaller, the total mass and the burnt mass are also smaller. In addition, the slightly higher temperature of the burnt zone leads to an increase in enthalpy for the burnt zone. All together, these terms cancel one another out and the temperature increase before compression is not amplified during combustion. As the combustion phase continues, the temperature for the higher compression ratio decreases compared to the original compression ratio. After TDC, $\frac{dV}{dt}$ becomes positive. This means that the increase in pressure for the higher compression ratio leads to a smaller increase in temperature, and hence a lower absolute temperature.

The mass and volume are both decreased, and due to the higher compression ratio, there is a bigger decrease in volume than there is in mass. Therefore the ratio of mass to volume increases. Combined with the slightly higher temperature, this leads to a significant increase in pressure, and hence also in peak pressure. Due to the decrease in temperature near the end of the combustion phase, the increase in pressure also diminishes.

Table 7.2: Change in power, peak pressure and peak temperature when varying the compression ratio.

	Power	**Peak pressure**	**Peak temperature**
-100%	-21.23%	-79.79%	-2.38%
+100%	16.34%	76.18%	2.14%

$$pV = nRT \tag{7.5}$$

$$C_v dT = -dQ_{loss} - pdV \tag{7.6}$$

The decrease in temperature for the higher compression ratio is amplified during the expansion phase. The sign of dV has changed and the increase in pressure for the higher compression ratio is diminishing, but it is still present. This increase in pressure now leads to a more negative dT and hence an amplification of the temperature decrease. This leads to a decrease in pressure, which in turn would lead to a less negative dT.

7.1.2. BORE

$$pV = nRT \tag{7.7}$$

$$C_v dT = -dQ_{loss} - pdV \tag{7.8}$$

From Figure 7.4, it is clear that the bore has a significant effect on the volume inside the cylinder. From Table 7.3 it can be seen that, when changing the bore with 100%, the effect on the power is even higher than 100%. This is because the volume (and hence the power) scales with the bore squared. The difference in volume is most distinct at the start of compression, and becomes smaller as the compression phase proceeds. From Figure 7.4 it can be seen that the clearance volume, which is signified by the minimum volume in the P-V diagram, increases with increasing bore. Since the compression ratio does not change, but V_0 does change, the clearance volume has to change. The increase in volume due to the increase in bore leads to an increase in fuel-air mixture inside the cylinder, while all other factors influencing the compression phase stay the same. This gives no change in pressure and temperature during the compression phase.

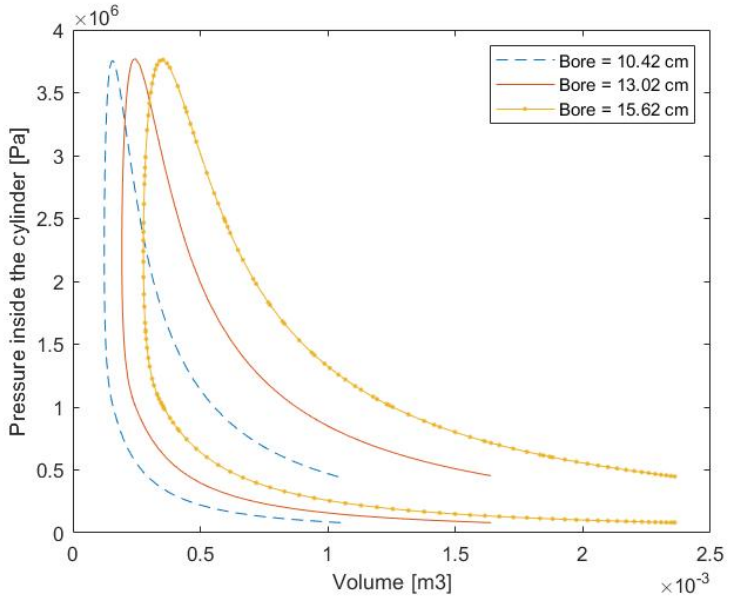

Figure 7.4: P-V diagram with varying bore.

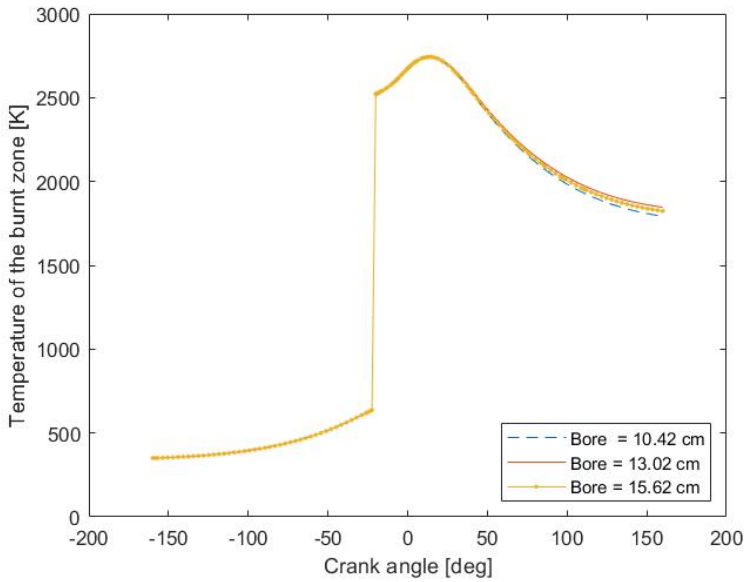

Figure 7.5: Burnt zone temperature profile with varying bore.

$$m_{b,j+1} C_p \frac{T_{b,j+1} - T_{b,j}}{\Delta t} = -P_{j+1} \frac{dV}{dt} + m_{total} \frac{dW_b}{dt} (h_{in} - h_b) - \dot{\omega} h_b - \dot{Q}_{loss} \tag{7.9}$$

$$P_{j+1} = \frac{m_{b,j+1} R T_{b,j+1}}{V_{b,j+1} M m_b}. \tag{7.10}$$

A change in the bore does not affect the combustion phase. As mentioned, the amount of fuel-gas mixture increases. In addition, $\frac{dV}{dt}$ increases. However, since the amount of mass in the cylinder and the volume are linearly related, these cancel each other out, leading to an unchanged temperature. The same applies to the pressure.

Table 7.3: Change in power, peak pressure and peak temperature when varying the bore.

	Power	**Peak pressure**	**Peak temperature**
-100%	-185.14%	-1.75%*	-1.19%*
+100%	214.47%	-1.10%*	-0.67%*

During the expansion phase, the same is valid as for the compression phase. A small deviation in temperature can be seen in Figure 7.5, but it is assumed this is due to numerical error.

7.1.3. STROKE

The effect of the stroke on the pressure is clearly less distinct than the effect of the bore, as can be seen from both Figure 7.6 and Table 7.4, as the volume scales linearly with the stroke. The clearance volume also changes with the stroke, though less than for the bore. Overall, a change in stroke leads to the same effects as a change in bore, but with a lower magnitude.

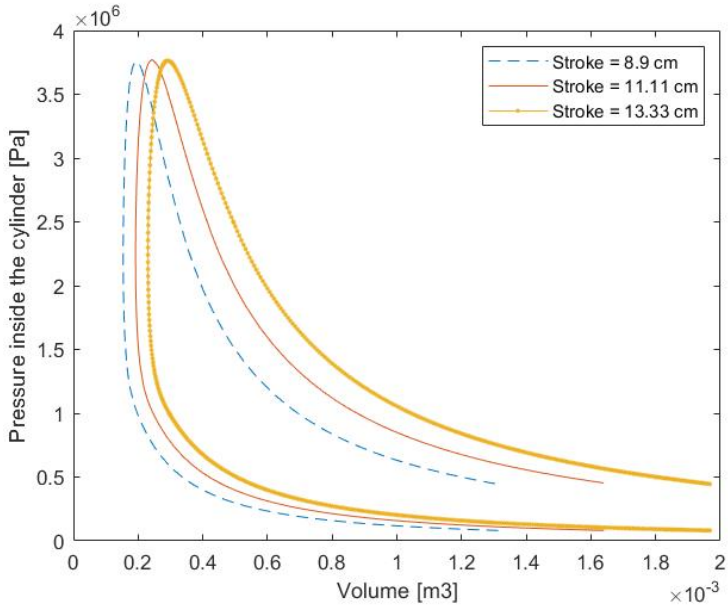

Figure 7.6: P-V diagram with varying stroke.

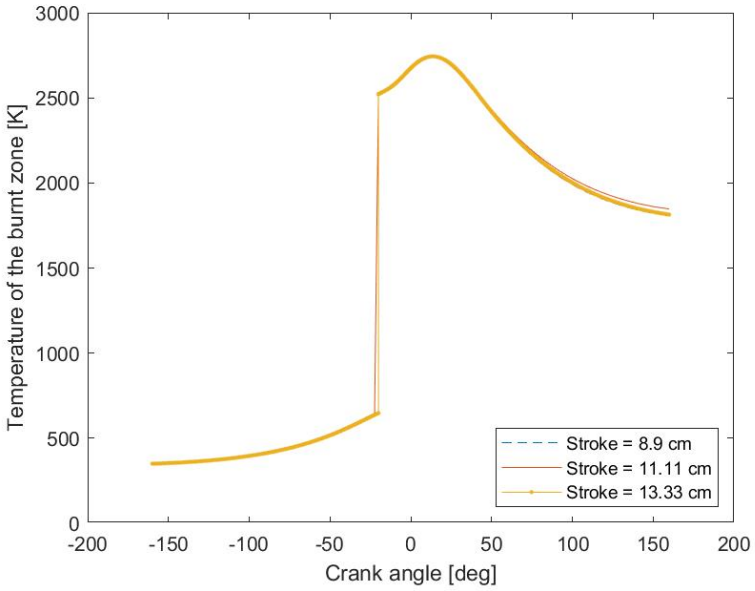

Figure 7.7: Burnt zone temperature profile with varying stroke.

Table 7.4: Change in power, peak pressure and peak temperature when varying the stroke.

	Power	**Peak pressure**	**Peak temperature**
-100%	-105.68%	-1.97%*	-1.24%*
+100%	94.57%	-0.88%*	-0.62%*

7.1.4. CONNECTING ROD LENGTH

$$pV = nRT \tag{7.11}$$

$$C_v dT = -dQ_{loss} - pdV \tag{7.12}$$

The connecting rod length, or more specifically the connecting rod length to crank arm ratio, has an influence on the volume profile. For convenience, the governing equation is repeated in Equation 7.13, where R is this ratio. When the crank angle is equal to -180°, 0° or 180°, the connecting rod length does not impact the volume. However, between these points, the volume decreases slightly with an increase in connecting rod length to crank arm ratio. Additionally, there is an increase in dV early in the compression phase (as there is a larger decrease in volume), while there is a decrease in dV later in the compression phase, though this does not seem to influence the temperature significantly. However, a minor difference in peak pressure is present as can be seen in Figure 7.8 and Table 7.5. As the pressure at the end of compression is not dependent on the path, the change in volume throughout the compression phase should not influence the pressure before combustion. This means that the change in pressure occurs during the combustion phase.

$$\frac{V}{V_{clear}} = 1 + \frac{CR+1}{2}\left(R + 1 - \cos\theta - \sqrt{R^2 - \sin^2\theta}\right) \tag{7.13}$$

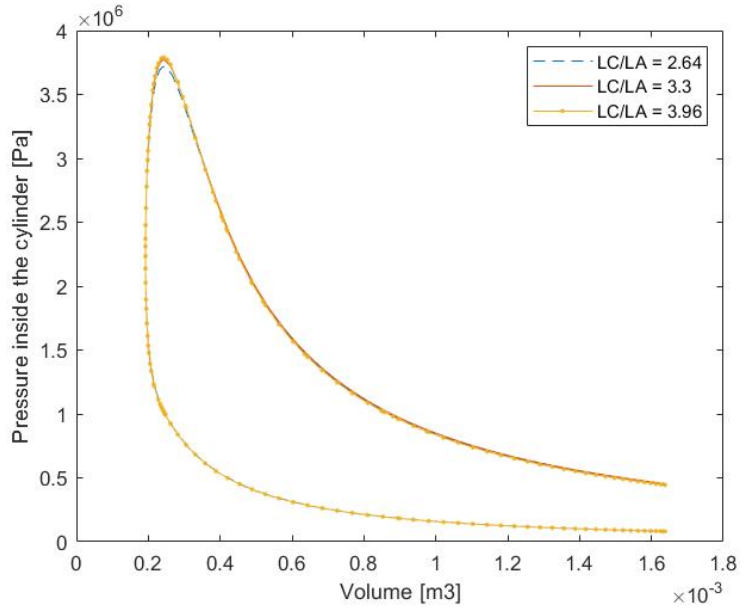

Figure 7.8: P-V diagram with varying crank arm to connecting rod length ratio.

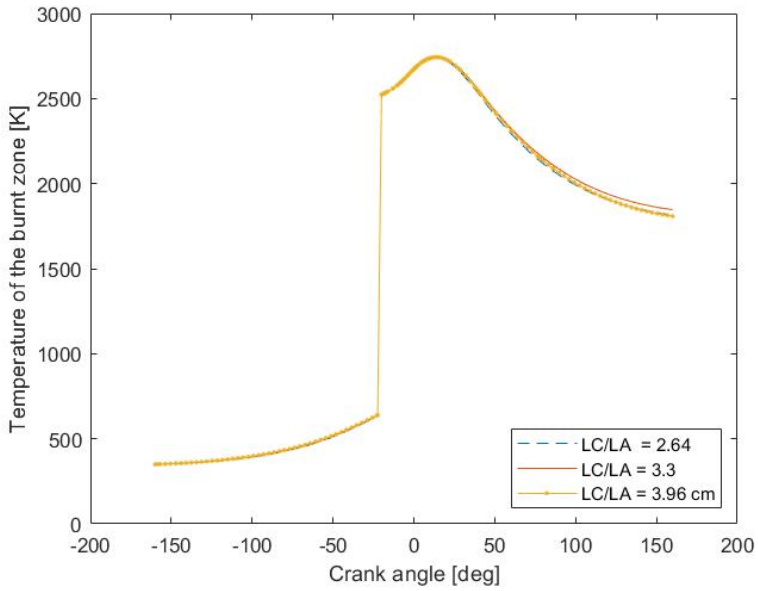

Figure 7.9: Burnt zone temperature profile with varying crank arm to connecting rod length ratio.

$$m_{b,j+1} C_p \frac{T_{b,j+1} - T_{b,j}}{\Delta t} = -P_{j+1} \frac{dV}{dt} + m_{total} \frac{dW_b}{dt} (h_{in} - h_b) - \dot{\omega} h_b - \dot{Q}_{loss} \tag{7.14}$$

$$P_{j+1} = \frac{m_{b,j+1} R T_{b,j+1}}{V_{b,j+1} M m_b}. \tag{7.15}$$

During the first phase of combustion (before TDC), there is a small decrease in volume. This decrease in volume leads to a decrease in volume of the burnt zone, and together with the unchanged temperature leads to a higher pressure. Then, this higher pressure in combination with the decreased $\frac{dV}{dt}$ explains the lack of change in temperature.

Table 7.5: Change in power, peak pressure and peak temperature when varying the crank arm to connecting rod length ratio.

	Power	**Peak pressure**	**Peak temperature**
-100%	-4.94%*	-6.98%	-1.22%*
+100%	-5.81%*	2.65%	-0.33%*

7.1.5. INLET VALVE CLOSED

$$pV = nRT \tag{7.16}$$

$$C_v dT = -dQ_{loss} - pdV \tag{7.17}$$

Decreasing the IVC angle by 20% leads to convergence issues, therefore a decrease of 12.50% is used. Furthermore, IVC angle cannot be increased beyond -180°, which gives an increase of 12.50%. Instead of looking at the increase in IVC angle, the decrease in IVC angle is considered. As IVC angle is decreased, the simulation starts later. The imposed pressure and temperature before compression are thus defined at a later stage, and hence give a lower pressure and temperature for the same crank angle and volume compared to the higher values for IVC angle. This does not significantly influence the temperature, but does have an effect on the pressure during the compression phase. In addition, the same pressure for a smaller volume leads to a smaller amount of fuel-air mixture present in the cylinder. Similarly to Section 7.3.1, this leads to an amplification of the pressure difference as the compression phase continues, while not influencing the temperature.

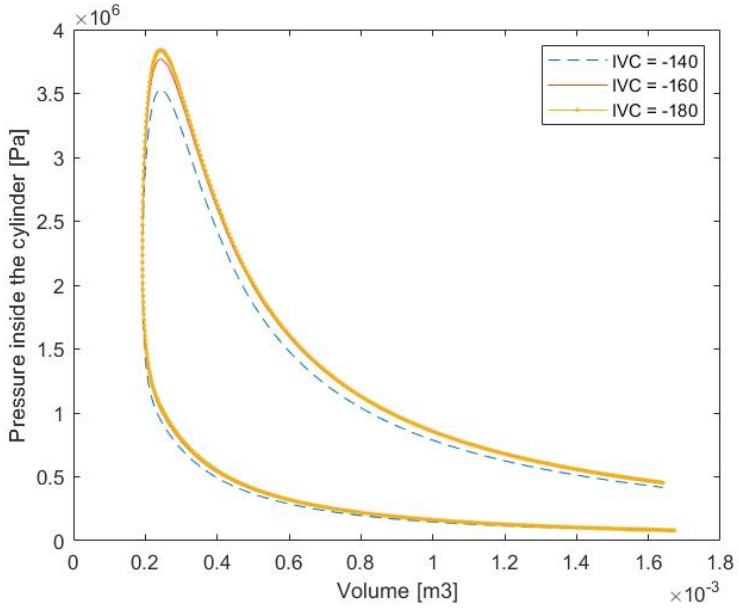

Figure 7.10: P-V diagram with varying IVC angle.

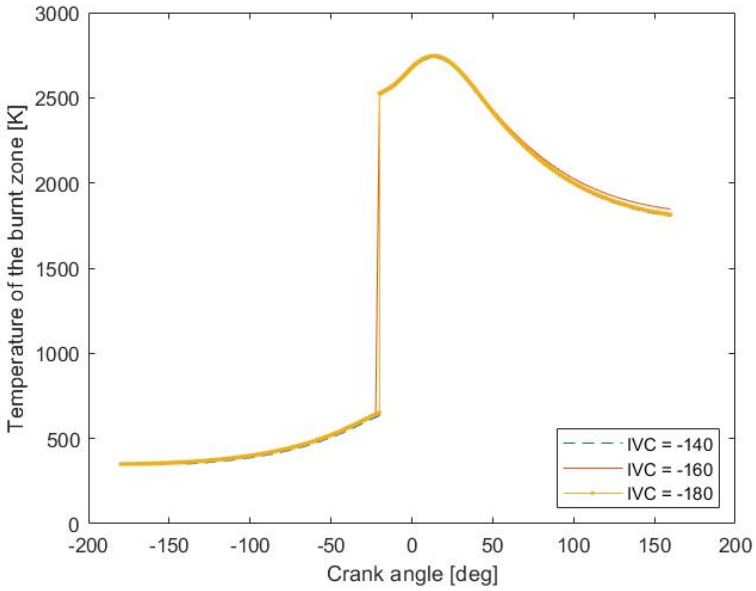

Figure 7.11: Burnt zone temperature profile with varying IVC angle.

$$m_{b,j+1} C_p \frac{T_{b,j+1} - T_{b,j}}{\Delta t} = -P_{j+1} \frac{dV}{dt} + m_{total} \frac{dW_b}{dt} (h_{in} - h_b) - \dot{\omega} h_b - \dot{Q}_{loss} \tag{7.18}$$

$$P_{j+1} = \frac{m_{b,j+1} R T_{b,j+1}}{V_{b,j+1} M m_b}. \tag{7.19}$$

For the combustion, the results can be compared to those of Section 7.3.1, where the decrease in amount of fuel-air mixture present leads to an amplified decrease in pressure, while cancelling out the effect on the temperature. These effects are more prominent for a decrease in IVC angle than for an increase in IVC angle, although an increase in the peak pressure is seen for an increase in IVC angle. At crank angles close to BDC (at the start of the compression stroke), the change in pressure with crank angle is relatively small, as the relative change in volume is small. This means that an absolute change in pressure closer to BDC (as is the case for a larger IVC angle) has a smaller effect, eventually leading to a smaller effect on the peak pressure.

The power is computed by dividing the work by the time it takes to complete two strokes. The work is found by taking the area in the P-V diagram, using the *trapz* function in Matlab. This function computes the area in the graph according to Equation 7.20. The summation starts in the bottom right corner of Figure 7.10 and works its way through the simulation. During the compression stroke, $x_{n+1} - x_n$ is negative, subtracting the area under the compression stroke from the total. Then, once the minimum volume is reached, $x_{n+1} - x_n$ becomes positive, adding the area between the expansion stroke and the x-axis. As IVC angle increases, the subtracted area becomes larger, decreasing the work and hence the power. This explains why, even though there is an increase in peak pressure, there is no increase in power. As IVC angle decreases, the subtracted area becomes smaller. One would expect this to lead to an increase in power. As the subtracted area is small (as the pressure is relatively close to 0), this effect is easily compensated for by the decrease in peak pressure and pressure during the expansion phase, hence leading to a net decrease in power.

$$\int_a^b = f(x)dx \approx \frac{1}{2} \sum_{n=1}^{N} (x_{n+1} - x_n) \left[f(x_n) + f(x_{n+1}) \right] \tag{7.20}$$

Table 7.6: Change in power, peak pressure and peak temperature when varying IVC angle.

	Power	**Peak pressure**	**Peak temperature**
-100%	-49.95%	-51.25%	-3.73%*
+100%	4.77%*	14.57%	-0.47%*

7.1.6. EXHAUST VALVE OPEN

The EVO angle could not be increased beyond 180°, which is an increase of 12.50%. With EVO angle, the end of the simulation is changed. As this change only happens at the end of the expansion phase, there is no influence on the pressure and temperature throughout the compression, combustion and expansion phase. However, Table 7.7 shows a significant influence on the power when EVO angle is decreased. The more EVO angle is decreased, the smaller the area in the P-V diagram as computed in Matlab. However, one would expect an increase in EVO angle to lead to an increase in area under the P-V diagram, and hence an increase in power. This is not the case.

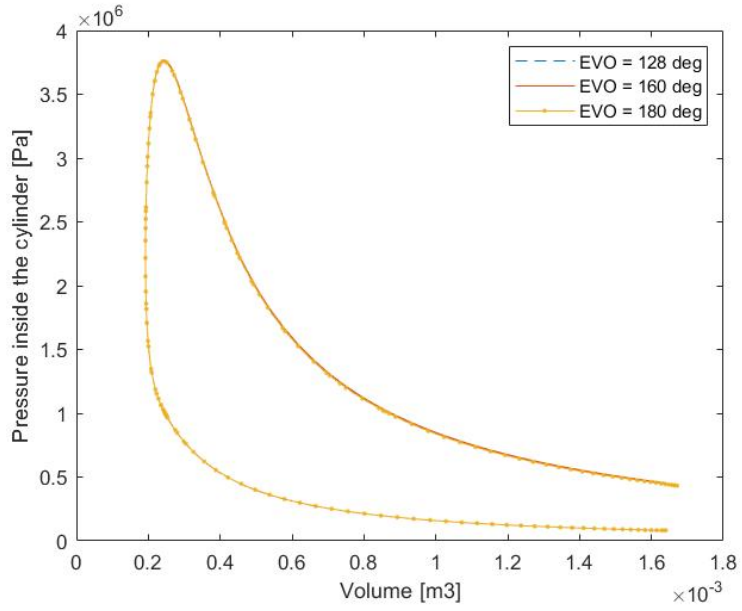

Figure 7.12: P-V diagram with varying EVO angle.

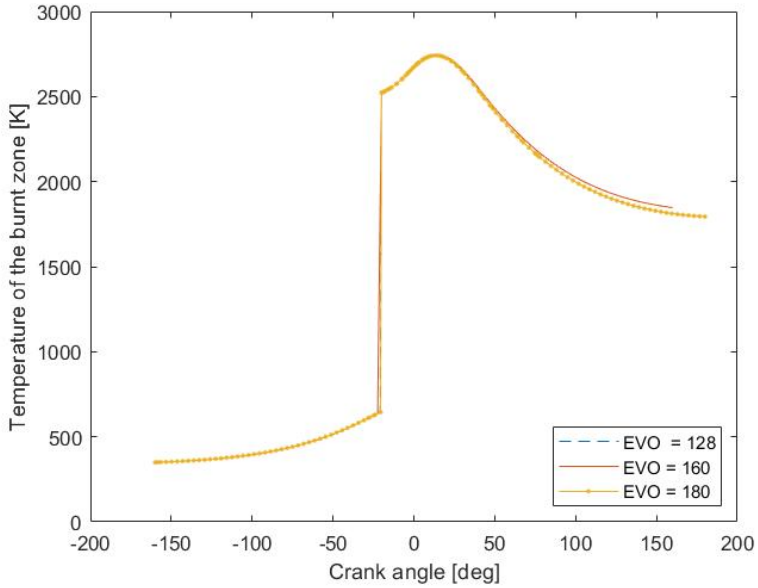

Figure 7.13: Burnt zone temperature profile with varying EVO angle.

Table 7.7: Change in power, peak pressure and peak temperature when varying EVO angle.

	Power	**Peak pressure**	**Peak temperature**
-100%	-34.18%	-1.35%*	-0.87%*
+100%	-1.50%*	-2.31%*	-1.37%*

It is clear that the problem is a numerical one, introduced when processing the data instead of when creating the data. To find the problem, the integration process by Matlab is replaced by a manual integration process, where a list of the multiplications inside the sum in Equation 7.20 is created and then summed. In Figure 7.14, the values of the multiplication can be found for each different value of EVO angle. It is quite clear that the values for an EVO angle of 160° and 180° are higher, but also that the amount of data points is smaller, hence cancelling out when the values are summed. However, when removing some of these relatively high values, as is the case when decreasing the EVO angle, summing the values no longer cancels out the change in magnitude. This could explain why an increase in EVO angle does not lead to a change in power (as the amount of data points for an EVO angle of 160° and an EVO angle of 180° are similar), but a decrease in EVO angle does lead to a decrease in power. The method of finding the work used in the current program is not suitable to compare simulations with a significantly different amount of data points and simulation lengths.

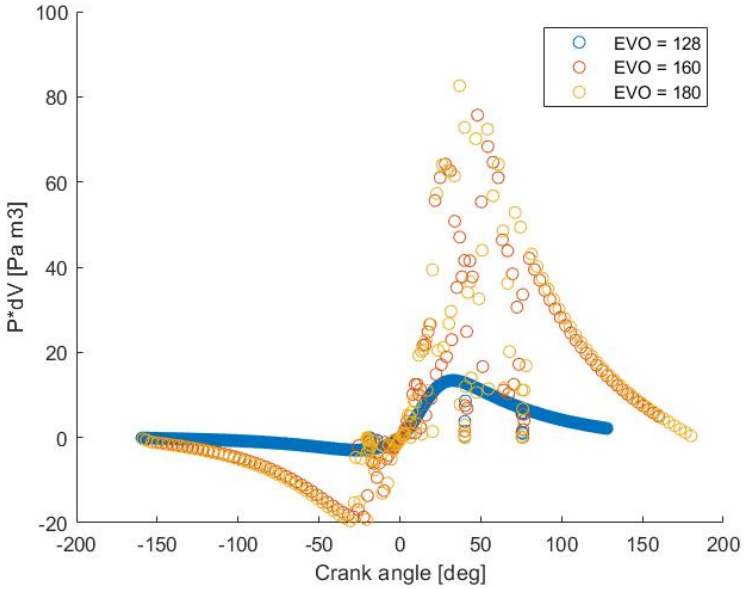

Figure 7.14: Graph showing the values of the multiplication used to find the work.

7.1.7. Main Takeaways

The effect of the compression ratio, bore and stroke on the power is significant, due to the increase in work. The compression ratio is the only parameter which affects the peak pressure. For a change in bore or stroke the compression ratio remains the same. None of the engine lay-out parameters have a significant effect on the peak temperature. Additionally, the method used to determine the power of the engine is not suitable in comparing different values of Inlet Valve Closed angle and Exhaust Valve Open angle.

7.2. Changing the Fuel

When changing the fuel, two things change: the thermodynamic properties and the gas kinetics files. The thermodynamic properties and gas kinetics cannot simply be changed by 20%, so a comparison is made between iso-octane and hydrogen. In this paragraph, only the thermodynamic properties and gas kinetics files are changed, not other fuel dependent parameters.

$$pV = nRT \tag{7.21}$$

$$C_v dT = -dQ_{loss} - pdV \tag{7.22}$$

In Chemkin, the fuel is assumed to be present and well mixed at the start of the simulation. This means that, when switching to hydrogen, the properties during the compression phase change, as well as the amount of air present due to the lower volumetric efficiency. The change in properties during compression is evident from Figure 7.15. For the same volume, there is a higher pressure (and temperature) for hydrogen. The governing property is the heat capacity of the fuel-air mixture. A comparison between the values for the iso-octane mixture and for the hydrogen mixture for temperatures relevant for the compression phase can be seen in Figure 7.17. It is clear that for both the heat capacity the values for hydrogen are lower than the values for iso-octane. The lower heat capacity leads to a higher temperature. This higher temperature then leads to the higher pressure during the compression phase.

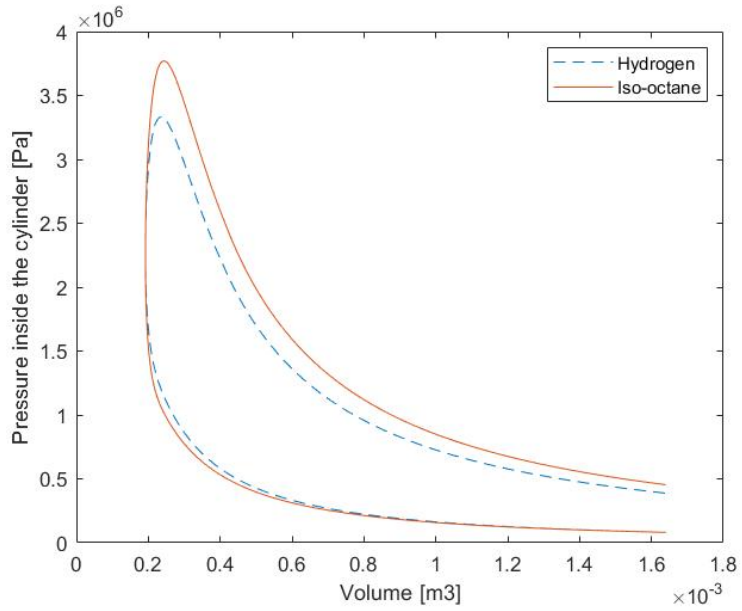

Figure 7.15: P-V diagram with varying fuel.

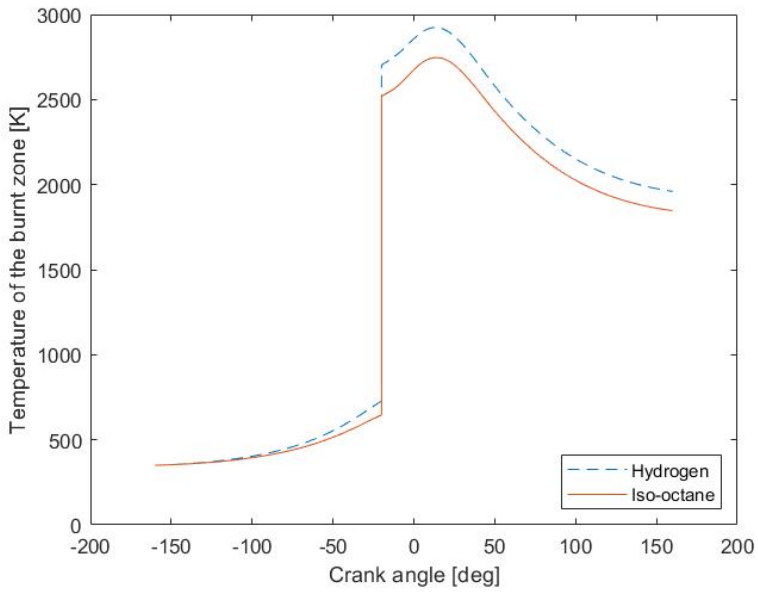

Figure 7.16: Burnt zone temperature profile with varying fuel.

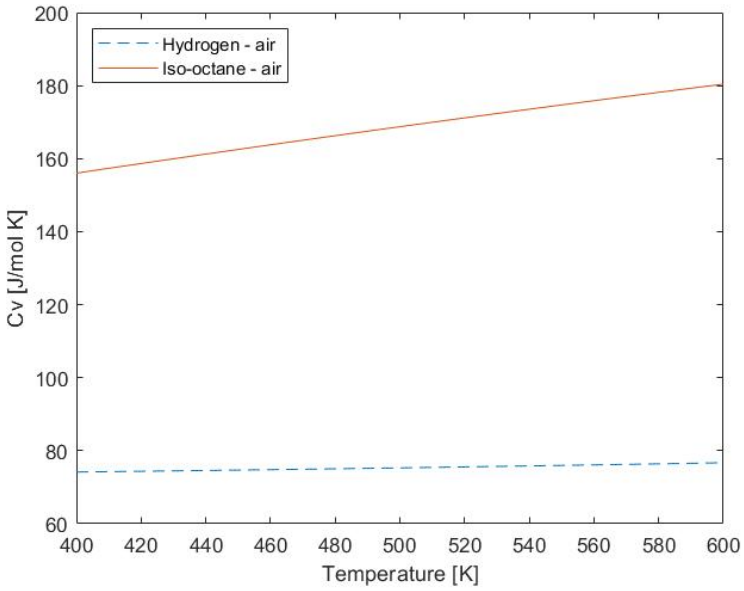

Figure 7.17: Heat capacity of the fuel-air mixture for Avgas and hydrogen.

$$m_{b,j+1} C_p \frac{T_{b,j+1} - T_{b,j}}{\Delta t} = -P_{j+1} \frac{dV}{dt} + m_{total} \frac{dW_b}{dt} (h_{in} - h_b) - \dot{\omega} h_b - \dot{Q}_{loss} \tag{7.23}$$

The temperature rise during combustion is larger for hydrogen than for iso-octane as can be seen in Figure 7.16. Figures 7.18 and 7.19 show the enthalpy and heat capacity of the products of the combustion of iso-octane and hydrogen. As can be seen, there is a slightly lower enthalpy for the same temperature for hydrogen as there is for iso-octane. However, since the temperature of the burnt zone for hydrogen is higher, the enthalpy of the burnt zone for hydrogen is higher. The enthalpy of the incoming mass flow is also higher for hydrogen, due to the higher adiabatic flame temperature for hydrogen. In addition, there is a higher total mass (and also burnt zone mass) due to the higher molar mass of the burnt zone species with hydrogen combustion, as well as a higher heat capacity for the burnt zone temperature. All things considered, the lower heat capacity for hydrogen (up to approximately 1800 K) seems to have the most influence, increasing the temperature increase and explaining the increase in temperature rise.

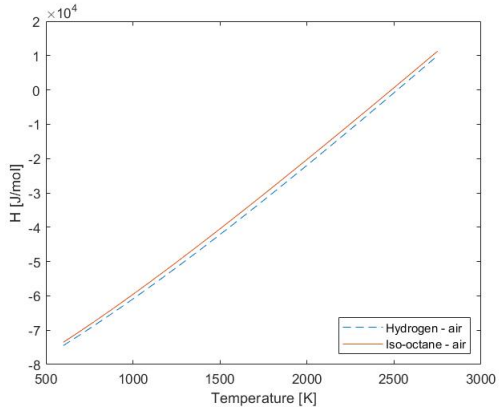

Figure 7.18: Enthalpy of the products for iso-octane and hydrogen combustion.

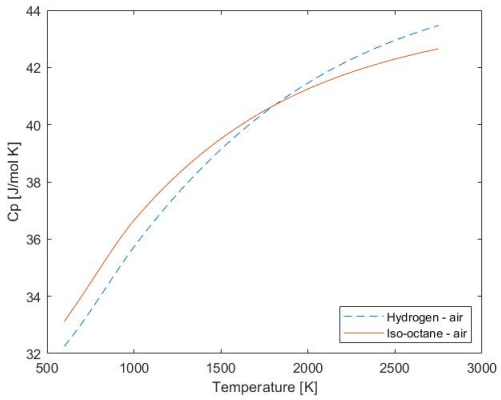

Figure 7.19: Heat capacity of the products for iso-octane and hydrogen combustion.

$$P_{j+1} = \frac{m_{b,j+1} R T_{b,j+1}}{V_{b,j+1} M m_b} \tag{7.24}$$

With a higher temperature, one would expect a higher pressure. However, Figure 7.15 clearly shows that this is not the case. This can be explained by the significantly higher molar mass of the products in the burnt zone for hydrogen (69 g/mol) compared to iso-octane (28.6 g/mol).

Table 7.8: Change in power, peak pressure and peak temperature when varying the fuel.

	Power	**Peak pressure**	**Peak temperature**
Hydrogen	-19.67%	-11.65%	6.44%

$$pV = nRT \qquad (7.25) \qquad C_v dT = -dQ_{loss} - pdV \qquad (7.26)$$

The decrease in pressure is damped during the expansion phase, and the temperature increase is damped slightly. The damping of the pressure divergence means the pressure for hydrogen increases compared to iso-octane, and can be explained by the increased temperature. The increase in dT (which causes the damping effect for the temperature) can be attributed to the lower heat capacity of the products of hydrogen combustion.

Changing the fuel without changing any other parameter, leads to unexpected changes in power, pressure and temperature. It is clear that other parameters (such as the burn duration) must be changed to accommodate for a change in fuel.

7.3. Changing the Operating Conditions

Four parameters defining the operating conditions can be changed: the pressure before compression, the temperature before compression, the equivalence ratio and the engine speed. The default values used in this sensitivity analysis are given in Table 7.9. With the economy cruise setting at 65% of full power [63, p.3-13], a decrease and increase of 20% of the operating conditions relative to the standard values as defined in Table 7.9 approximately spans the standard operating envelope of the engine.

Table 7.9: Standard operating condition values.

	Pre-compression pressure [atm]	**Pre-compression temperature [K]**	**Equivalence ratio**	**Engine speed [RPM]**
Value	0.8	350	1.0	2350

7.3.1. Pressure Before Compression

$$pV = nRT \qquad (7.27) \qquad C_v dT = -dQ_{loss} - pdV \qquad (7.28)$$

Due to convergence issues, the pressure before compression could not be differed by 20% in either direction. Therefore, a change of -18.75% and +12.50% is used. As can be seen in Figure 7.20 an increase in the pressure before compression is amplified during the compression phase, leads to a higher peak pressure and is damped during the expansion phase. The temperature does not change. The increase in pressure during the compression phase is due to the increase in fuel-air mixture present in the cylinder. This same increase in fuel-air mixture cancels out the effect of the increase in pressure on the temperature.

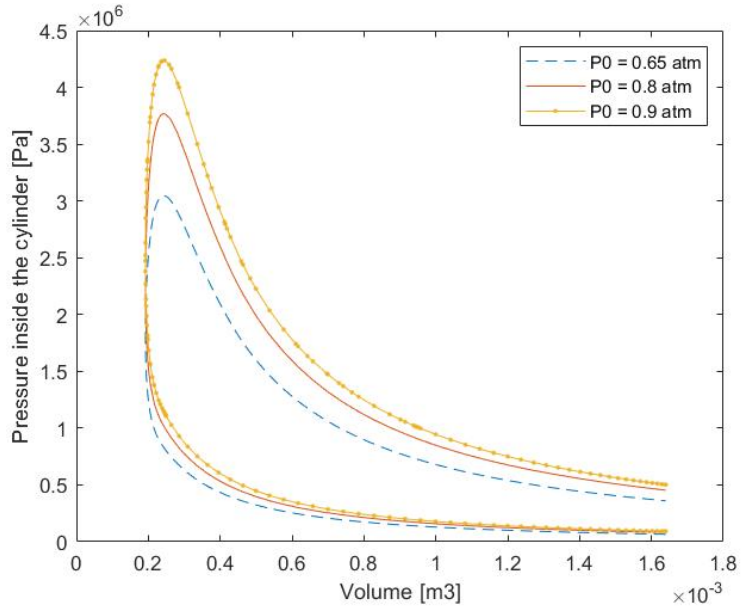

Figure 7.20: P-V diagram with varying $P0$.

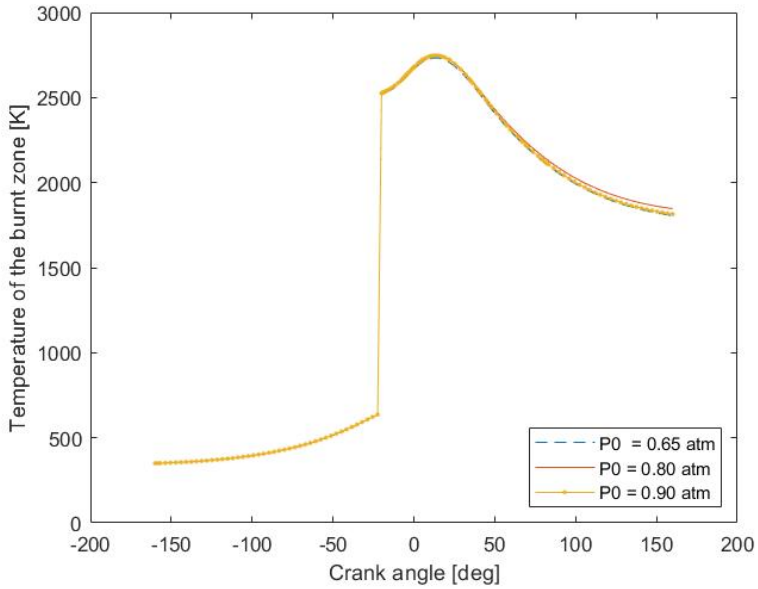

Figure 7.21: Burnt zone temperature profile with varying $P0$.

$$m_{b,j+1} C_p \frac{T_{b,j+1} - T_{b,j}}{\Delta t} = -P_{j+1} \frac{dV}{dt} + m_{total} \frac{dW_b}{dt} (h_{in} - h_b) - \dot{\omega} h_b - \dot{Q}_{loss} \tag{7.29}$$

$$P_{j+1} = \frac{m_{b,j+1} R T_{b,j+1}}{V_{b,j+1} M m_b}. \tag{7.30}$$

The increase in pressure is amplified during combustion due to the higher total mass, which leads to a higher burnt zone mass. This same higher burnt zone mass cancels out the increase in pressure and total mass, leading to an unchanged temperature. As the ratio between the amount of moles inside the cylinder and the volume decreases during expansion, the pressure difference must also decrease, damping the pressure divergence. This has no influence on the temperature.

Table 7.10: Change in power, peak pressure and peak temperature when varying $P0$.

	Power	**Peak pressure**	**Peak temperature**
-100%	-106.27%	-102.33%	-2.74%*
+100%	91.90%	99.16%	0.12%*

7.3.2. TEMPERATURE BEFORE COMPRESSION

$$pV = nRT \tag{7.31}$$

$$C_v dT = -dQ_{loss} - pdV \tag{7.32}$$

Decreasing the temperature before compression by 20% leads to convergence issues, therefore a decrease of 14.30% is used. Increasing the temperature reduces the amount of fuel-air mixture present in the cylinder. The decrease in amount of fuel-air mixture and the increase in temperature cancel each other out, leading to an unchanged pressure, as can be seen in Figure 7.22. This increase in temperature before compression is not amplified during the compression stage, as can be seen in 7.23.

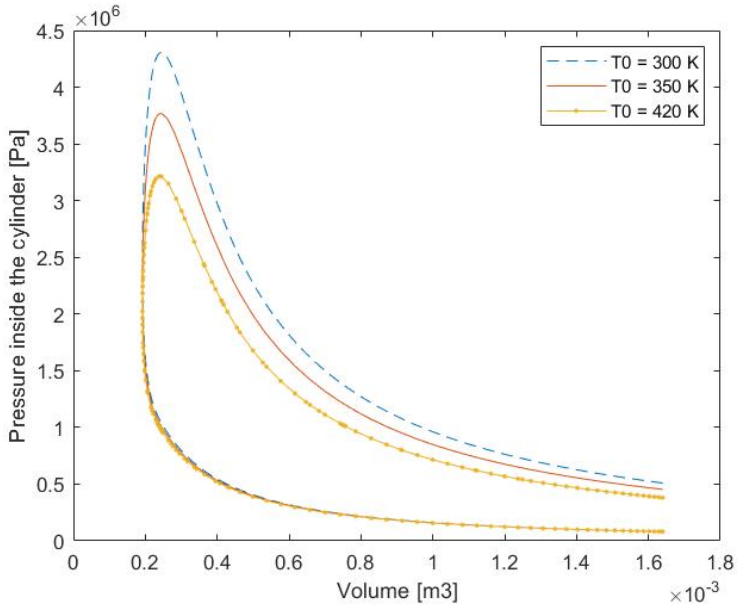

Figure 7.22: P-V diagram with varying $T0$.

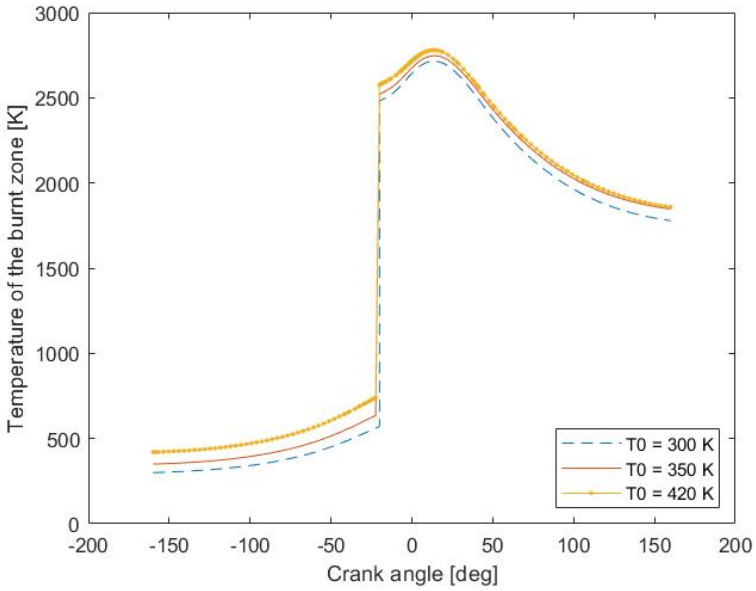

Figure 7.23: Burnt zone temperature profile with varying $T0$.

$$m_{b,j+1} C_p \frac{T_{b,j+1} - T_{b,j}}{\Delta t} = -P_{j+1} \frac{dV}{dt} + m_{total} \frac{dW_b}{dt} (h_{in} - h_b) - \dot{\omega} h_b - \dot{Q}_{loss} \tag{7.33}$$

$$P_{j+1} = \frac{m_{b,j+1} R T_{b,j+1}}{V_{b,j+1} M m_b}. \tag{7.34}$$

During combustion, the total mass and burnt zone mass are decreased, while the pressure decreases as the combustion phase continues. Due to the higher temperature, the enthalpy of the burnt zone increases. This all leads to a decrease in change in temperature, damping the temperature increase as found before combustion. As the increase in temperature dampens, the pressure decreases, leading to a decreased peak pressure for a higher temperature before compression.

Table 7.11: Change in power, peak pressure and peak temperature when varying $T0$.

	Power	**Peak pressure**	**Peak temperature**
-100%	118.93%	99.62%	-8.05%
+100%	-95.54%	-73.64%	5.97%

$$pV = nRT \tag{7.35}$$

$$C_v dT = -dQ_{loss} - pdV \tag{7.36}$$

The change in pressure dampens as the expansion phase proceeds, as the ratio of temperature to volume decreases. The lower pressure for the higher temperature before start of compression leads to a slightly changed dT and thus a minor effect on the temperature during the expansion phase.

7.3.3. Equivalence Ratio

$$pV = nRT \tag{7.37}$$

$$C_v dT = -dQ_{loss} - pdV \tag{7.38}$$

Changing the equivalence ratio changes the ratio of fuel to air in the fuel-air mixture, and hence changes the thermodynamic properties of the fuel-air mixture. A higher equivalence ratio leads to more fuel and increases the specific heat capacity. As can be seen in Figures 7.24 and 7.25, this effect is negligible.

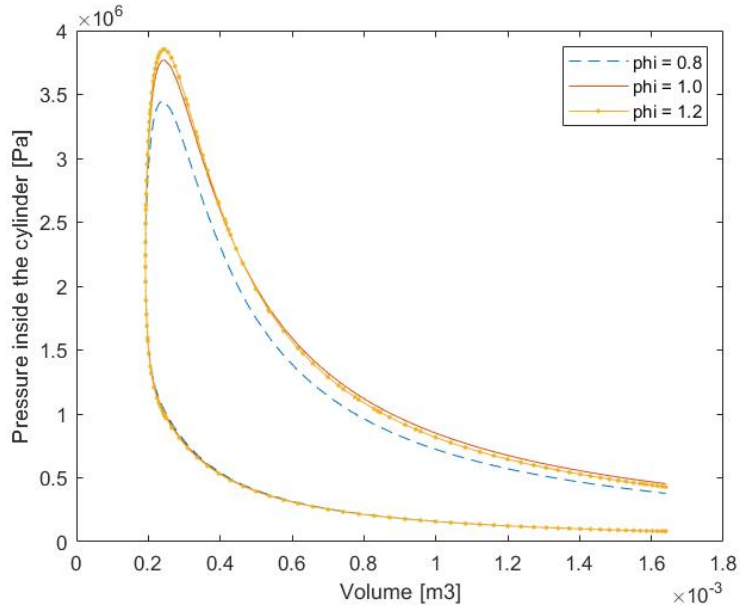

Figure 7.24: P-V diagram with varying equivalence ratio.

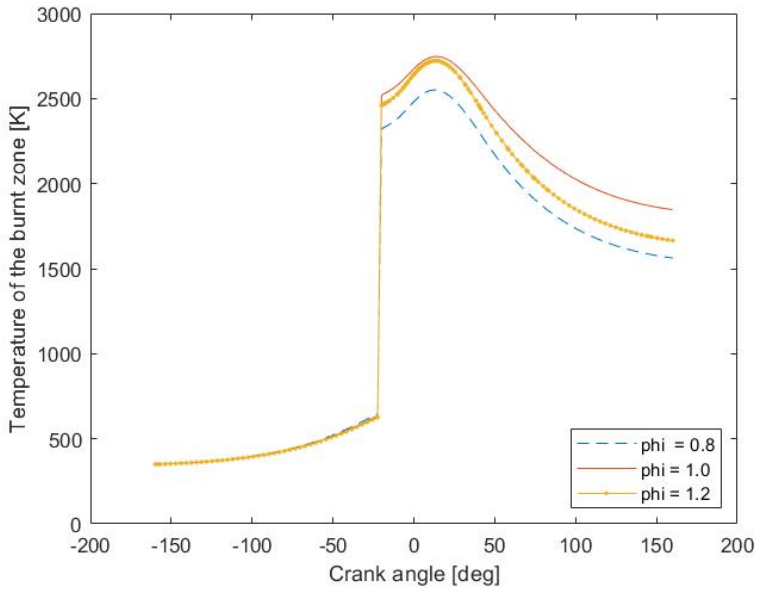

Figure 7.25: Burnt zone temperature profile with varying equivalence ratio.

$$m_{b,j+1} C_p \frac{T_{b,j+1} - T_{b,j}}{\Delta t} = -P_{j+1} \frac{dV}{dt} + m_{total} \frac{dW_b}{dt} (h_{in} - h_b) - \dot{\omega} h_b - \dot{Q}_{loss} \tag{7.39}$$

$$P_{j+1} = \frac{m_{b,j+1} R T_{b,j+1}}{V_{b,j+1} M m_b}. \tag{7.40}$$

During combustion, the deviation becomes apparent. As the equivalence ratio increases, the peak pressure increases. As the peak pressure for an equivalence ratio equal to 1.2 is only slightly higher than the peak pressure for an equivalence ratio of 1.0, an optimum equivalence ratio is implied. This effect can also be seen in Figure 7.25, where an equivalence ratio of 1.0 leads to the highest peak temperature. This can be explained when looking at the enthalpy of the mass flow entering the burnt zone. The enthalpy is evaluated at the adiabatic flame temperature. This adiabatic flame temperature decreases when the equivalence ratio deviates from approximately 1.1, as excess air or fuel absorbs part of the energy released. The decrease in adiabatic flame temperature leads to a decrease in enthalpy of the incoming mass flow. In addition, an increase in equivalence ratio leads to an increase in total mass and burnt zone mass (due to the higher molar mass of the fuel). The pressure is slightly increased, but not enough to realise an increase in the change in temperature. This all leads to a decrease in temperature change, and hence a decrease in peak temperature. This coincides with general knowledge of a piston engine, as a piston engine is run slightly rich to provide cooling. For an equivalence ratio of 1.2, the decrease in temperature is not severe enough to result in a lower pressure. As the equivalence ratio increases, the change in temperature is expected to become more dominant and result in a decrease in pressure.

Table 7.12: Change in power, peak pressure and peak temperature when varying the equivalence ratio.

	Power	**Peak pressure**	**Peak temperature**
-100%	-79.88%	-42.68%	-35.71%
+100%	-5.85%*	10.95%	-4.53%

$$pV = nRT \tag{7.41}$$

$$C_v dT = -dQ_{loss} - pdV \tag{7.42}$$

Then, as the expansion phase commences, the temperature for an equivalence ratio of 1.2 drops extensively, as can be seen in Figure 7.25. The added fuel vapour leads to a decrease in the average heat capacity. Due to the decrease in heat capacity, the change in temperature increases, leading to the extensive drop in temperature. The drop in temperature leads to a drop in pressure, which is apparent in Figure 7.24, where the pressure for an equivalence ratio of 1.2 decreases below that of the equivalence ratio 1.0. As the pressure decreases, dT increases, leading to a divergence of the temperature during the expansion phase. The ratio between the temperature and volume decreases as the expansion phase proceeds, leading to a decrease in pressure and hence damping of the pressure divergence.

7.3.4. Engine Speed

The engine speed has no effect on the peak pressure and peak temperature, as found in Table 7.13, however, a small visual divergence can be seen in Figure 7.27. This divergence is assumed to be due to numerical error and is deemed negligible. There is however a significant influence on the power, as the engine speed determines the time in which the work is done. When the work stays the same, but the engine speed doubles, the time in which the work is done halves and thus the power doubles. A linear relationship between the engine speed and the power is found, which is expected.

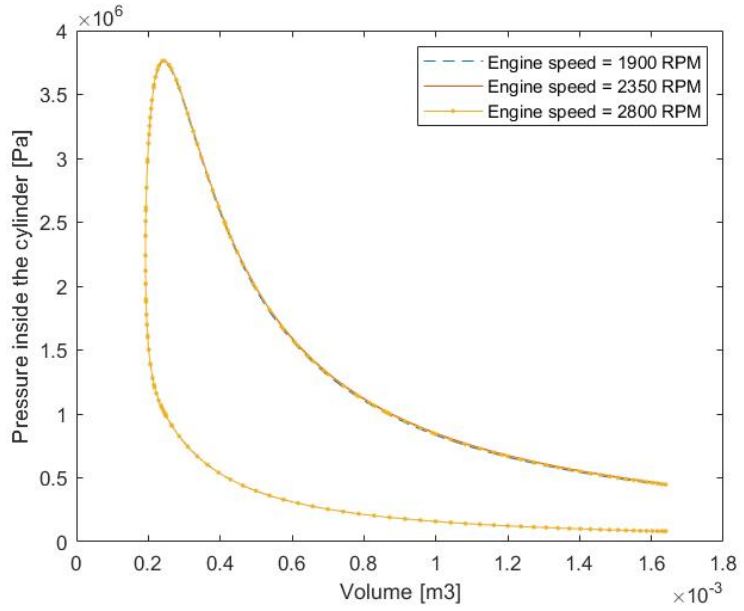

Figure 7.26: P-V diagram with varying engine speed.

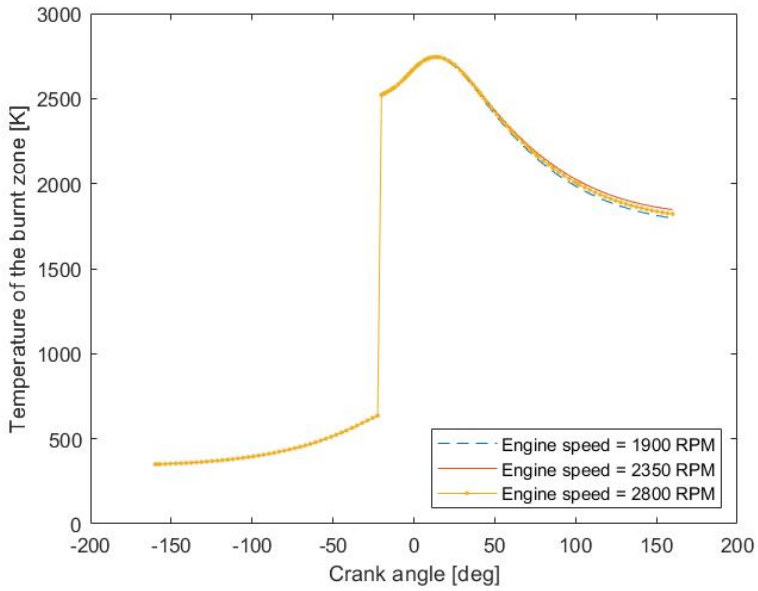

Figure 7.27: Burnt zone temperature profile with varying engine speed.

Table 7.13: Change in power, peak pressure and peak temperature when varying the engine speed.

	Power	**Peak pressure**	**Peak temperature**
-100%	-106.82%	-2.16%*	-1.50%*
+100%	95.40%	-0.86%*	-0.46%*

7.3.5. MAIN TAKEAWAYS

A change in pressure and temperature before compression has a significant effect on the peak pressure and consequently the power, as the amount of fuel-air mixture inside the combustion chamber changes. This change in amount of fuel-air mixture in combination with the change in pressure, gives no significant change in temperature. Both an increase and decrease in equivalence ratio give a decrease in power, pressure and temperature, implying an optimum value of the equivalence ratio. This corresponds with literature. The engine speed has no significant effect on the peak pressure and peak temperature, but as the engine speed increases, the work is performed in a smaller amount of time and the power increases.

7.4. CHANGING THE HEAT TRANSFER PARAMETERS

Eight parameters for the heat transfer coefficient can be varied, each of them given in Table 7.14 with their default values used in the sensitivity analysis. For reference, the heat transfer correlations used are restated in Equation 7.43 and 7.44. Whether a change in 20% is representative is unknown at this point. For low temperatures, where the difference between the temperature inside the combustion chamber and the wall temperature is small, the heat transfer (and hence the heat transfer parameters) does not have a notable effect on the pressure and temperature. This is the case during the compression phase. Then, when the temperature rises, the effect of only one of the heat transfer parameters becomes distinct: the heat transfer parameter b. The heat transfer parameter b could only be decreased by 12.50% before encountering convergence issues.

Table 7.14: Standard heat transfer values.

	a	**b**	**c**	**C11**	**C12**	**C2 [cm/s K]**	$\mathbf{v}_{swirl}/\bar{S}_p$	**Wall temperature [K]**
Value	0.035	0.8	1.0	2.28	0.318	0.324	0.2	500

$$Nu = aRe^b Pr^c \tag{7.43}$$

$$\bar{w} = \left(C_{11} + C_{12}\frac{v_{swirl}}{\bar{S}_p}\right)\bar{S}_p + C_2\frac{VT_0}{p_0 V_0}\left(p - p_{motored}\right) \tag{7.44}$$

Looking at Equations 6.15 and 6.16, it can be deduced that the Reynolds number has an order of magnitude of 1e4, mostly due to the viscosity. Heat transfer parameter a has an order of magnitude of 1e-2 while the last term, Pr^c has an order of magnitude of 1. The Reynolds number, together with its exponent, thus has the highest influence on the heat transfer coefficient. The influence of the heat transfer parameters a and c is thus relatively small. The viscosity has the largest influence on the Reynolds number, explaining why the heat transfer parameters $C11$, $C12$, $C2$ and the swirl velocity do not have a notable influence. However, heat transfer parameter b, the exponent of the Reynolds number, does have a significant influence on the power.

Due to the high Reynolds number, the influence of the exponent of the Reynolds number is amplified. This leads to a significantly higher Nusselt number, and in turn a significantly higher heat transfer coefficient. At high temperatures and at high surface areas (when the volume is high), this leads to a significant heat loss, and a significantly lower temperature, as can be seen in Figure 7.29. The significantly lower temperature in turn leads to a lower pressure, as can be seen in Figure 7.28.

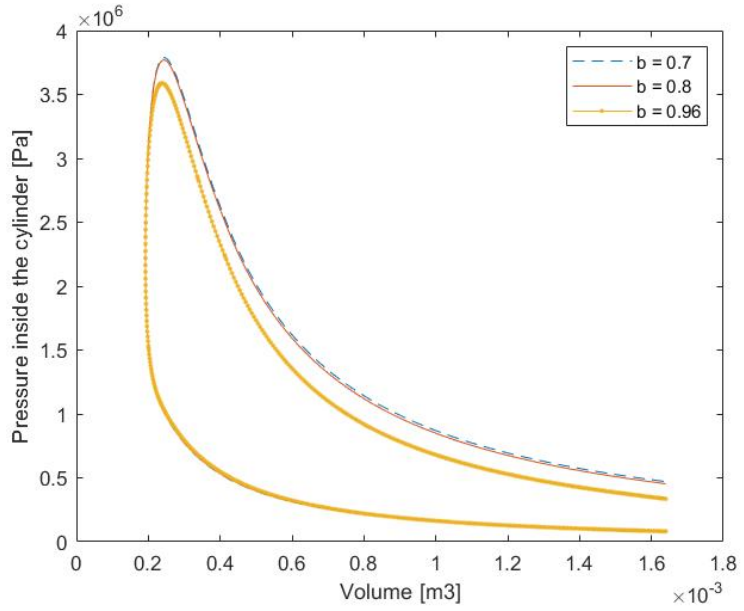

Figure 7.28: P-V diagram with varying heat transfer parameter b.

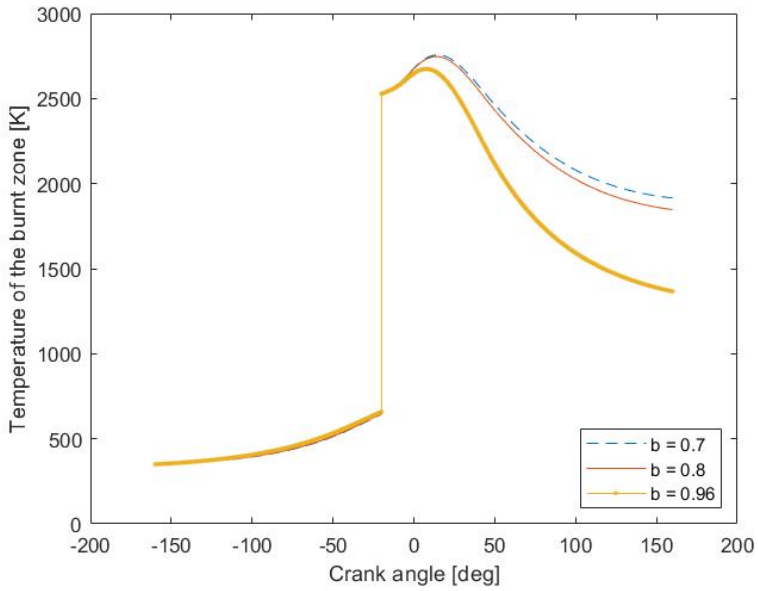

Figure 7.29: Burnt zone temperature profile with varying heat transfer parameter b.

An interesting phenomenon that can be seen in Figure 7.29 is the large divergence during the expansion phase. As mentioned, the heat loss is governed by the heat transfer coefficient, the difference in temperature between the gases and the wall (which decreases as the expansion phase proceeds) and the wall area (which increases as the expansion phase proceeds). It is clear that the increase in wall area is significant, leading to a strong divergence. An increase in heat transfer parameter b has a larger influence than a decrease in heat transfer parameter b. As the heat transfer parameter b is the exponent of the Reynolds number, a 20% deviation in either direction does not lead to a 20% deviation in heat transfer coefficient. A decrease of heat transfer parameter b from 0.8 to 0.7 leads to a decrease in heat transfer coefficient of 60%, while an increase from 0.8 to 0.96 leads to an increase in heat transfer coefficient of 336%. This major difference in heat transfer coefficient then leads to a major difference in heat loss and eventually temperature.

Table 7.15: Change in power, peak pressure and peak temperature when varying heat transfer parameter b.

	Power	**Peak pressure**	**Peak temperature**
-100%	17.02%	3.88%	2.77%
+100%	-90.48%	-24.06%	-13.32%

The wall temperature does not have a notable influence on the peak pressure and temperature. At low gas temperatures, the heat loss is low. Therefore, changing the wall temperature has a low influence. Then, as the gas temperature increases, the relative change in wall temperature decreases. A change of 100 K is more significant when the gas temperature is 500 K, than when the gas temperature is 2000 K. These two effects combined lead to no notable change in the peak pressure, peak temperature and power, when the wall temperature is changed.

It is clear that the only heat transfer parameter which has a significant effect on the results is the heat transfer parameter b. Optimising the heat transfer parameters for each fuel, engine and operating condition is thus not a priority.

7.5. Changing the Burn Profile Parameters

Four parameters for the Wiebe function can be changed, given in Table 7.16 with their default values. For reference, the Wiebe function is restated in Equation 7.45. The Wiebe function starts at the specified timing for start of combustion. The parameters therefore do not have an influence on the compression phase, while all influence on the expansion phase is due to the changes in the combustion phase. A change of 20% of the Wiebe function parameters is representative when using one specific fuel and merely changing the operating conditions. However, when another fuel (such as hydrogen) is used, the burn duration decreases considerably. Additionally, to allow for smooth operation with hydrogen, the start of combustion is delayed considerably. A change of 20% is thus not representative when changing the fuel.

Table 7.16: Standard Wiebe function values.

	n_W	b_W	**Start of combustion [°bTDC]**	**Burn duration [°]**
Value	2	5	20	60

$$W_b = 1 - \exp\left[-b_W\left(\frac{\theta-\theta_0}{\Delta\theta}\right)^{n_W+1}\right] \tag{7.45}$$

7.5.1. Wiebe parameter n and b

The Wiebe parameters n and b are considered together, as they both influence the shape of the burn profile. The Wiebe parameter n cannot be decreased too much due to convergence issues, and hence a decrease of 10.00% is used. Varying the Wiebe parameter b also causes convergence issues, a decrease of 4.00% and an increase of 10.00% is used. As can be seen from Figure 7.30, the Wiebe parameter n has a larger effect on the Wiebe function at the start of combustion, while the Wiebe parameter b has a larger effect on the Wiebe function at the end of combustion. An increase in Wiebe parameter n leads to a slower start of combustion, with a lower Wiebe function (and hence less mass in the burnt zone) for the same crank angle. An increase in the Wiebe parameter b leads to a faster burn at the end of the combustion phase, with a higher Wiebe function for the same crank angle.

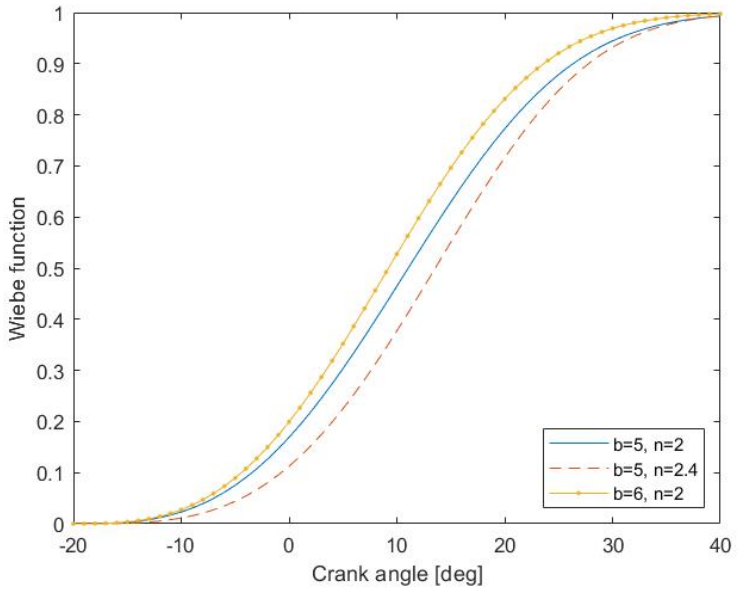

Figure 7.30: Influence of the Wiebe parameters n and b on the Wiebe function.

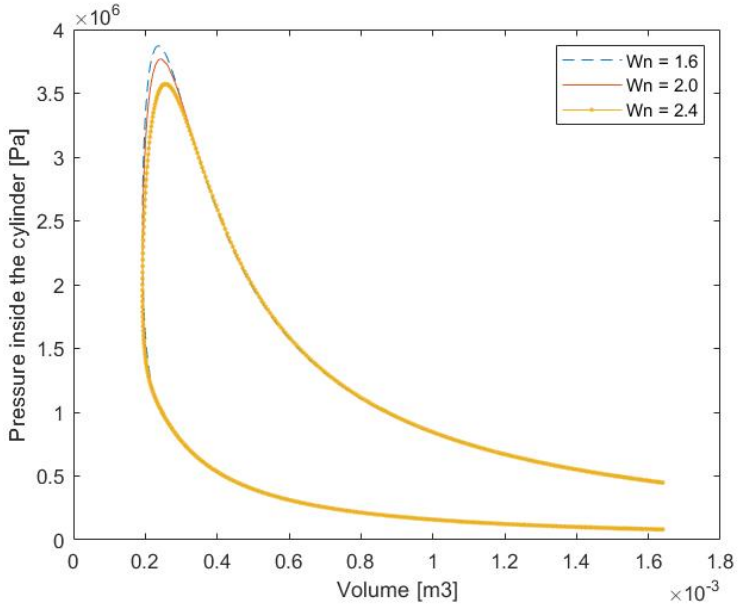

Figure 7.31: P-V diagram with varying Wiebe parameter n.

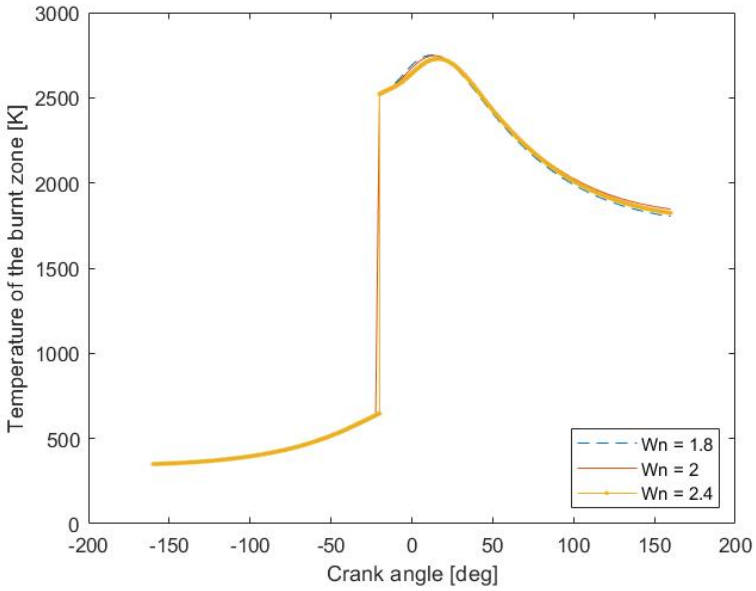

Figure 7.32: Burnt zone temperature profile with varying Wiebe parameter n.

$$m_{b,j+1} C_p \frac{T_{b,j+1} - T_{b,j}}{\Delta t} = -P_{j+1} \frac{dV}{dt} + m_{total} \frac{dW_b}{dt} (h_{in} - h_b) - \dot{\omega} h_b - \dot{Q}_{loss} \tag{7.46}$$

$$P_{j+1} = \frac{m_{b,j+1} R T_{b,j+1}}{V_{b,j+1} M m_b}. \tag{7.47}$$

From Figures 7.31 and 7.32, it can be seen that increasing the Wiebe parameter n leads to a significant decrease of the peak pressure, while leading to a minor decrease in the peak temperature. The lower value for the Wiebe function leads to a lower burnt zone mass, which leads to a lower pressure. The smaller $\frac{dW_b}{dt}$ and lower pressure together give a lower temperature for the first phase of combustion. However, as the combustion proceeds, $\frac{dW_b}{dt}$ increases, and the temperature increases. This eventually leads to a minor decrease in peak temperature for a higher Wiebe parameter n and a delayed temperature response. Although the peak pressure increases with decreasing Wiebe parameter n, the power does not. Small deviations of the pressure throughout the combustion phase could explain this.

Table 7.17: Change in power, peak pressure and peak temperature when varying the Wiebe parameter n.

	Power	**Peak pressure**	**Peak temperature**
-100%	-7.44%	26.83%	1.24%
+100%	-9.80%	-26.16%	-3.35%

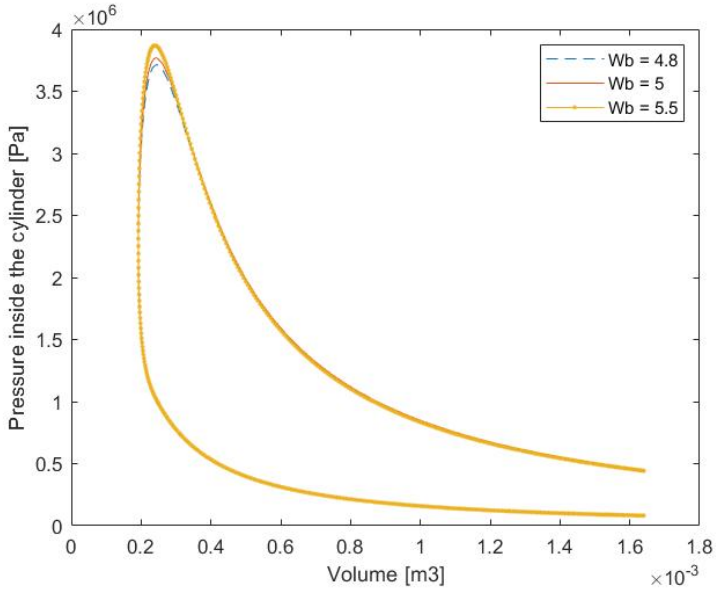

Figure 7.33: P-V diagram with varying Wiebe parameter b.

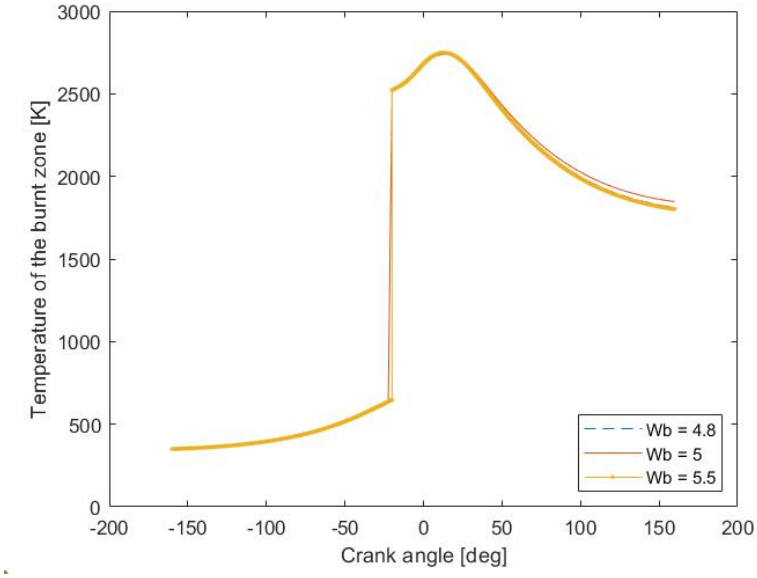

Figure 7.34: Burnt zone temperature profile with varying Wiebe parameter b.

$$m_{b,j+1} C_p \frac{T_{b,j+1} - T_{b,j}}{\Delta t} = -P_{j+1} \frac{dV}{dt} + m_{total} \frac{dW_b}{dt} (h_{in} - h_b) - \dot{\omega} h_b - \dot{Q}_{loss} \tag{7.48}$$

$$P_{j+1} = \frac{m_{b,j+1} R T_{b,j+1}}{V_{b,j+1} M m_b}. \tag{7.49}$$

An increase in pressure is seen as the Wiebe parameter b increases. This can be explained by the higher Wiebe function for the same crank angle, leading to a higher burnt zone mass. However, this does not lead to a change in temperature, as these cancel one another out. As combustion proceeds, $\frac{dW_b}{dt}$ decreases, but this is compensated for by the higher pressure at this point, resulting in no temperature change. Although the peak pressure increases, the power decreases. This can be explained by small deviations of the pressure throughout the combustion phase.

Table 7.18: Change in power, peak pressure and peak temperature when varying the Wiebe parameter *b*.

	Power	**Peak pressure**	**Peak temperature**
-100%	-34.18%	-37.44%	-7.28%
+100%	-7.47%	26.38%	0.62%*

7.5.2. START OF COMBUSTION

The start of combustion angle does not affect the compression phase. However, as the start of combustion angle is increased (advanced), the compression phase ends earlier. This can be seen in Figure 7.36, where the steep increase in temperature occurs at a more advanced crank angle as the start of combustion angle is advanced.

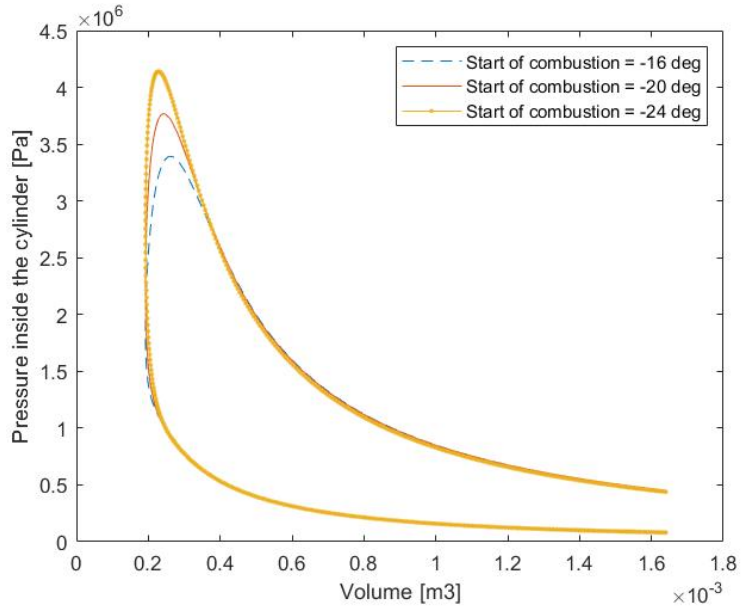

Figure 7.35: P-V diagram with varying start of combustion angle.

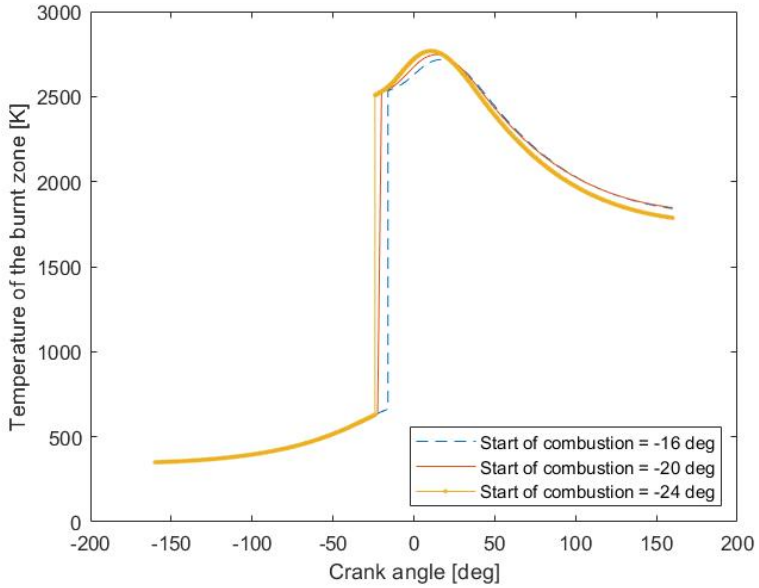

Figure 7.36: Burnt zone temperature profile with varying start of combustion angle.

$$m_{b,j+1} C_p \frac{T_{b,j+1} - T_{b,j}}{\Delta t} = -P_{j+1} \frac{dV}{dt} + m_{total} \frac{dW_b}{dt} (h_{in} - h_b) - \dot{\omega} h_b - \dot{Q}_{loss} \tag{7.50}$$

$$P_{j+1} = \frac{m_{b,j+1} R T_{b,j+1}}{V_{b,j+1} M m_b}. \tag{7.51}$$

As the start of combustion is advanced, the combustion phase starts and ends earlier, and the peak pressure and temperature occur earlier (at a lower volume) as seen in Figures 7.35 and 7.36. Not only do the peak pressure and temperature change in location, they also change in magnitude. As the start of combustion is advanced, the temperature at the start of combustion decreases (as less compression has taken place). This decrease in temperature is not amplified during the first phase of combustion, due to the increase in pressure and $\frac{dW_b}{dt}$. As the combustion phase commences, the pressure increases due to the increase in burnt mass. After the first phase of combustion, the initial decrease in temperature changes to an increase in temperature. $\frac{dW_b}{dt}$ now decreases, but the pressure increase is much more significant, leading to an increase in the change in temperature and hence a higher peak temperature. After the peak temperature has occurred, the decrease in temperature for an advanced start of combustion is higher, as there is no new hot mass entering the burnt zone, as combustion has been terminated.

Table 7.19: Change in power, peak temperature and peak pressure when varying the start of combustion angle.

	Power	**Peak pressure**	**Peak temperature**
-100%	-14.46%	-50.08%	-5.42%
+100%	-0.08%*	49.09%	3.80%

7.5.3. BURN DURATION

$$m_{b,j+1} C_p \frac{T_{b,j+1} - T_{b,j}}{\Delta t} = -P_{j+1} \frac{dV}{dt} + m_{total} \frac{dW_b}{dt} (h_{in} - h_b) - \dot{\omega} h_b - \dot{Q}_{loss} \tag{7.52}$$

$$P_{j+1} = \frac{m_{b,j+1} R T_{b,j+1}}{V_{b,j+1} M m_b}. \tag{7.53}$$

As the burn duration increases, the Wiebe function becomes less steep: the mass flow from the unburnt zone to the burnt zone decreases. This also means that, for a given crank angle, the value for the Wiebe function is lower. This leads to a lower pressure and temperature, and a peak pressure and peak temperature occurring at a higher crank angle (and at a higher volume) as can be seen in Figure 7.37. The increase in burn duration leads to an increase in pressure and temperature during the expansion phase. For a higher combustion duration, combustion is still occurring and the pressure is still increasing, while for the lower combustion duration there is only pure expansion. This effect is also present for the temperature, similarly to Section 7.5.2. This can also be seen for the power, where the large increase in peak pressure for a decreased burn duration only leads to a minor increase in power.

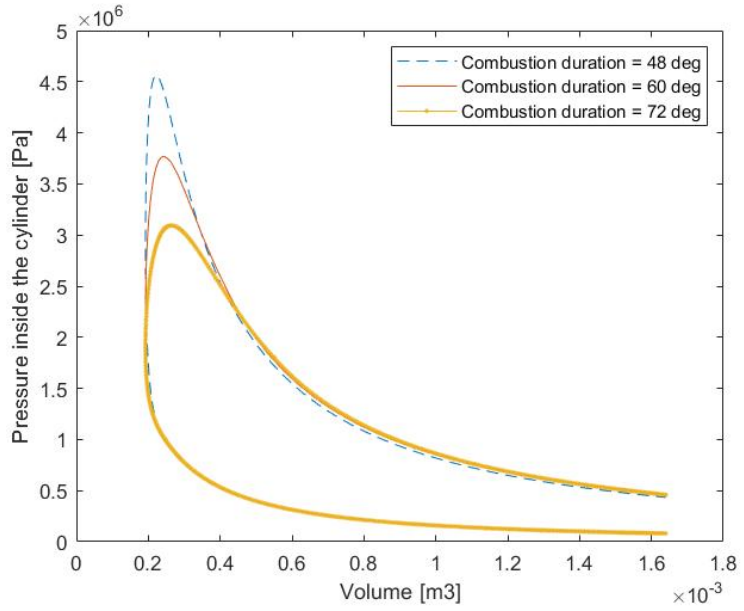

Figure 7.37: P-V diagram with varying burn durations.

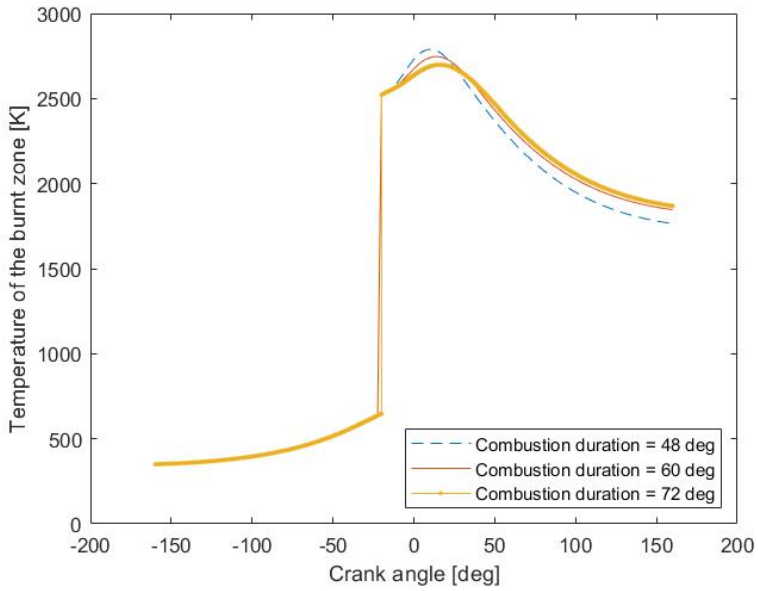

Figure 7.38: Burnt zone temperature profile with varying burn durations.

Table 7.20: Change in power, peak pressure and peak temperature when varying the burn duration.

	Power	**Peak pressure**	**Peak temperature**
-100%	6.50%	104.69%	7.70%
+100%	-25.08%	-89.73%	-8.81%

7.5.4. MAIN TAKEAWAYS

All Wiebe parameters have a significant influence on the peak pressure, and the burn duration has the highest effect. Additionally, the Wiebe parameters change the timing of peak pressure. The peak temperature is barely influenced by the Wiebe parameters, while for the power varying results are found. It is clear that, to obtain accurate results, an accurate burn profile is important. Specifically the start of combustion timing should be matched to the spark timing of the engine and the burn duration should be optimised for the engine, fuel and operating condition.

7.6. CONCLUSIONS OF THE SENSITIVITY ANALYSIS

The method used to compute the power (integrating the P-V diagram using the *trapz* function in Matlab) is not suitable for comparing different values of Inlet Valve Closed or Exhaust Valve Open angle. Only simulations with the same IVC and EVO angle should be compared, or a different method should be found to compute the power.

The Wiebe parameters, which should be optimised for each fuel, engine and operating condition, have a much larger effect on the power, peak pressure and peak temperature than the heat transfer parameters. The combustion duration specifically has a large influence on the peak pressure. Therefore, optimisation of the Wiebe function is essential and has priority over optimisation of the heat transfer parameters.

The effect of the change in input parameters is consistently larger for the peak pressure than for the peak temperature. The engine thus experiences larger changes in peak pressure than in peak temperature when changing the parameters. This does not necessarily mean that the peak pressure limits the operation of the engine. Depending on the safety margins of the engine, the pressure or temperature might be the critical factor.

The qualitative behaviour of Chemkin coincides with practical knowledge of piston engines. However, at this stage, it is unclear whether Chemkin provides accurate quantitative results. To provide a definitive answer on whether Chemkin is a suitable tool, validation in the form of experiments is necessary. When Chemkin is validated, the results can be used to assess the risk of catastrophic engine failure due to an increase in pressure and/or temperature. This poses a dilemma. To evaluate the risk and obtain the permits for the test set-up, experimental validation is needed, while the permits for the test set-up are necessary to perform experimental validation.

Several solutions are possible. The first is to validate Chemkin with a different, certified, test set-up. A second solution is to obtain preliminary results without validation, and use these results (including a certain margin of error) for the risk analysis. The margin of error can be reduced by performing initial validation for Avgas only. As a second, certified, test set-up is not available, this second strategy is chosen.

8
PRELIMINARY PREDICTIONS

Based on the knowledge of the working and assumptions of Chemkin, some preliminary predictions can be made regarding the behaviour of the engine while operating on Avgas and hydrogen. The expected effects of the assumptions on the results can be taken into account, and although an exact quantification of the effects is not yet available (as the validation experiments have to be conducted first), some preliminary conclusions on the differences between Avgas and hydrogen can be formed. Based on these conclusions, a risk analysis (although with a significant margin of error) can be performed. In Section 8.1, the method and results of the predictions for both Avgas and hydrogen is given. In Section 8.2, the subsequent risk of catastrophic failure is evaluated. Finally, in Section 8.3, several strategies for risk mitigation are introduced.

8.1. PREDICTIONS

As the engine will be equipped with both a port fuel injection system and a direct injection system, a comparison is made for both systems. The physical properties of the Lycoming engine (which are kept constant throughout all predictions) are given in Table 8.1.

Table 8.1: Engine parameters for the Lycoming engine.

	Compression ratio	**Bore [cm]**	**Stroke [cm]**	**Connecting rod length [cm]**	**IVC [°bTDC]**	**EVO [°aTDC]**
Value	8.7	13.02	11.11	19.53	160	160

The operating conditions chosen correspond to performance cruise, with an engine speed of 2450 RPM, an assumed equivalence ratio of 1.1 and a power rating of 75% for the actual engine [63, p.3-13]. It is assumed this corresponds to an amount of fuel-air mixture equal to 75% of maximum power conditions, and hence a pressure before compression of 0.75 atm.

8.1.1. AVGAS

The fuel used to represent Avgas is iso-octane. Avgas gives a 2.3% increase in energy release compared to iso-octane, and the equivalence ratio used in Chemkin should be increased to 1.125 to account for this. Furthermore, the burn duration should be decreased by 13%.

For the port fuel injection system, the volumetric efficiency and homogeneity can be assumed equal to that assumed by Chemkin. However, for the direct fuel injection system, this is not the case. The amount of air should be increased, and to obtain the same equivalence ratio, the amount of fuel should also be increased. This can be obtained by increasing the pressure before compression, assuming that the amount of gas present scales linearly with the pressure before compression. The volume of the cylinder before compression is 1.7e-3 m^3. Filling this completely with air (as is the case with direct injection) gives a total of 7.59e-2 mole of air. With an equivalence ratio of 1.1, this leads to an amount of fuel equal to 1.4e-3 mole. Combined, this gives a total of 7.73e-2 mole in the combustion chamber, an increase of 1.84%. To simulate this in Chemkin, the pressure before compression is increased with 1.84%.

The non-homogeneity of the fuel-air mixture for the actual engine can be accounted for by decreasing the equivalence ratio, with an amount which is not quantifiable at this point. A decrease of 0.05 is chosen.

The temperature before compression used in the sensitivity analysis is a standard value, and is better approximated by considering the amount and temperature of the residual gases. Taking the molar weighted average of the temperature of the incoming fresh air (assumed to be at 290 K) and the residual gas (assumed to be at 1800 K for Avgas), a temperature before compression of 415 K is found.

To account for the 27% underestimation of the viscosity during the expansion phase in Chemkin (as specified in Section 6.7.2), Sutherland's temperature can be changed. As this underestimation only occurs during the expansion phase, an average decrease in viscosity of 13.5% over the whole simulation is aimed for. Using the average temperature during the simulation for Avgas combustion, a new Sutherland's temperature of 53.6 K is found.

To account for the overestimation of the pressure throughout the simulation due to the assumption of the ideal gas law, the pressure before compression is decreased. As there is an underestimation of the pressure for hydrogen, the pressure should be decreased further for iso-octane combustion than for hydrogen combustion. A decrease in pressure of 2% is used for the prediction.

The Wiebe function could be approximated using the method as described in Section 6.7.3. However, as this is a comparative study, the standard values for the Wiebe function parameters are taken (given in Section 7.5) and modified to account for the use of iso-octane instead of Avgas.

To account for the heat transfer from the burnt zone to the unburnt zone, the Woschni heat transfer parameters during the combustion phase can be modified. However, as this is a comparative study and the change in Woschni heat transfer parameters cannot be quantified, it is chosen to keep them the same. The heat transfer parameters are kept equal to those given in Section 7.4.

It is assumed that the gas exchange loss and friction loss is similar for Avgas and hydrogen, therefore they are not considered. To account for blowby, the pressure before compression can be decreased. It is known that for hydrogen there is more blowby than for Avgas, but the amount is not quantified. Therefore blowby is assumed zero for Avgas, and a small amount of blowby (and hence a small decrease in pressure before compression) is assumed for hydrogen.

8.1.2. HYDROGEN

The fuel used to represent hydrogen is pure hydrogen, which leads to an overestimation of the energy release. How much is unknown, for now a similar overestimation as for Avgas is assumed. This means that the equivalence ratio used in Chemkin should be decreased to 1.051.

Similarly to Avgas, the difference between port fuel injection and direct injection must be taken into account. In this case, the amount of fuel found to obtain an equivalence ratio of 1.1 is 3.5e-2 moles. Together with the air, this gives a total of 1.11e-1 moles of mixture present after injection. This in an increase of 46%. To simulate this in Chemkin, the pressure before compression is increased with 46%.

To account for the non-homogeneity, the equivalence ratio is to be decreased. As hydrogen is highly dissipative, the mixture is assumed to be more homogeneous and the decrease in equivalence ratio should lower than for Avgas. A decrease of 0.03 is chosen for the prediction.

As the temperature of the residual gases is approximately 150 K higher for hydrogen compared to Avgas (as can be seen in Section 7.2), the temperature before compression is increased to 430 K.

When using hydrogen, the viscosity is underestimated by 41.5% during the expansion phase. Similarly to Avgas, this can be accounted for by changing the Sutherland's temperature to obtain an average increase in viscosity of 20.75%. This leads to a new Sutherland's temperature of 30.2 K.

To account for the ideal gas law, the pressure before compression should be reduced, although less than for Avgas. A decrease of 1.5% is chosen.

The flame speed of hydrogen is higher than for Avgas, which is compensated for by decreasing the burn duration. For iso-octane, a laminar flame velocity of approximately 40 cm/s is found [64] [65], while for hydrogen a laminar flame velocity of 2 m/s is found [66]. This means that hydrogen burns five times faster than Avgas. A burn duration of 1/5th of iso-octane is used for hydrogen.

The ignition delay for hydrogen is smaller than for Avgas, which can be compensated for by decreasing the Wiebe parameter n. A quantification is not available, and hence a decrease of 0.5 is chosen. As the spark timing will most definitely be modified when changing from Avgas to hydrogen, this is also taken into account in the prediction. A retardation of 10-18° compared to Avgas was suggested in Section 2.4. Taking into account the short burn duration for hydrogen, a spark timing of 2° bTDC is chosen.

The heat transfer coefficient is assumed equal for Avgas and hydrogen. However, a higher heat transfer coefficient is expected for the heat transfer to the cylinder walls, due the lower quenching distance. This can be accounted for by increasing the heat transfer parameter a. The change in heat transfer is not quantified, and an increase in heat transfer parameter a of 50% is estimated.

There is a small decrease in pressure before compression to account for blowby, which is estimated to be 2%.

The resulting inputs for the predictive simulations for both Avgas and hydrogen are given in Table 8.2. For each fuel, the input values for the simulation without taking the assumptions into account are given, as well as the input values for port fuel injection and direct injection.

Table 8.2: Input parameters for the predictive simulation in Chemkin.

	Avgas			**Hydrogen**		
	w/o as.	**PFI**	**DI**	**w/o as.**	**PFI**	**DI**
Pre-compression pressure [atm]	0.75	0.735	0.75	0.75	0.724	1.07
Pre-compression temperature [K]	415	415	415	430	430	430
Equivalence ratio	1.1	1.075	1.075	1.1	1.021	1.021
Engine speed [RPM]	2450	2450	2450	2450	2450	2450
Heat transfer parameter a	0.035	0.035	0.035	0.035	0.0525	0.0525
Heat transfer parameter b	0.8	0.8	0.8	0.8	0.8	0.8
Heat transfer parameter c	1.0	1.0	1.0	1.0	1.0	1.0
Woschni heat transfer parameter $C11$	2.28	2.28	2.28	2.28	2.28	2.28
Woschni heat transfer parameter $C12$	0.318	0.318	0.318	0.318	0.318	0.318
Woschni heat transfer parameter $C2$ [cm/s K]	0.324	0.324	0.324	0.324	0.324	0.324
$v_{swirl}/\bar{S}_p$	0.2	0.2	0.2	0.2	0.2	0.2
Wall temperature [K]	500	500	500	500	500	500
Wiebe parameter n	2	2	2	2	1.5	1.5
Wiebe parameter b	2.302	2.302	2.302	2.302	2.302	2.302
Start of combustion [°bTDC]	20	20	20	2	2	2
Burn duration [°]	52	52	52	12	12	12
Sutherland's temperature [K]	111	53.6	53.6	111	30.2	30.2

8.1.3. RESULTS

In Table 8.3, the predicted peak pressure, peak temperature and power is given for each simulation. The figures accompanying these numbers are given in Figures 8.1 to 8.8.

Table 8.3: Overview of the results of the predictions for Avgas and hydrogen combustion.

	Avgas PFI	**Avgas DI**	**Hydrogen PFI**	**Hydrogen DI**
Peak pressure [atm]	28.5	28.3	37.55	55.77
Peak temperature [K]	2763	2757	3134	3170
Power [kW]	23.3	23.7	18.1	27.0

In Figures 8.1 and 8.2, the P-V diagram and temperature profile for Avgas combustion are given. Three scenarios are compared: one where the assumptions as described in Section 8.1.1 are not considered, one where the values for port fuel injection as given in Table 8.2 are used and one where the input values for direct injection are used. The assumptions have a significant effect on the peak pressure, with the burn duration as the main cause. Similar behaviour is found as in Section 7.5.3.

The change in pressure before compression for both port fuel injection and direct injection is minor and the change in equivalence ratio does not impact the pressure and temperature in a significant manner. Sutherland's temperature only plays a significant role in the heat transfer, and as a relatively small change in heat transfer does not play a role in the peak pressure and temperature (as could be seen in Section 7.4), the results do not change. The slightly higher pressure during the expansion phase for direct injection leads to a small increase in power output, as can be seen from Table 8.3.

At a power rating of 75%, one would expect a power per cylinder of approximately 28 kW. This deviates from the results. Some assumptions are not taken into account, as this is a comparative study, such as the blowby, the heat transfer parameters and the Wiebe function parameters. The blowby decreases the power output, and the heat transfer parameters only have a minor impact on the pressure and power. This means that the Wiebe function parameters need optimisation, with the most probable cause of the deviation being an overestimation of the burn duration. Decreasing the burn duration increases the peak pressure and in turn increases the power output.

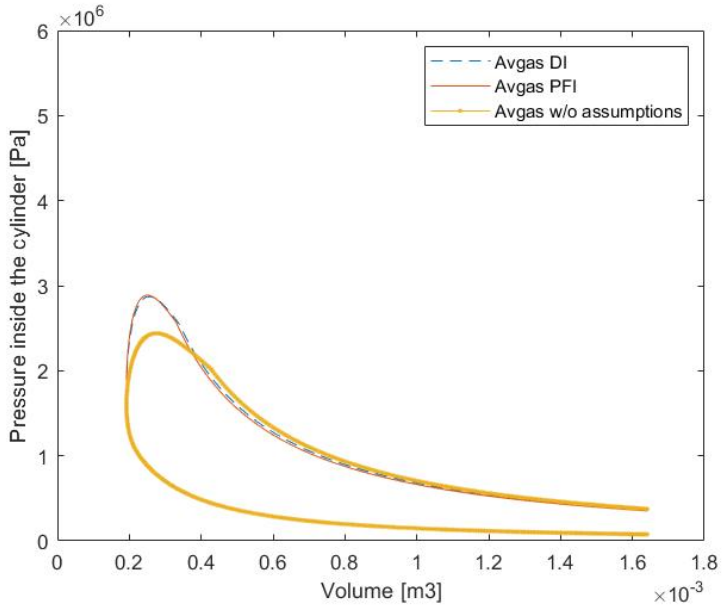

Figure 8.1: Predicted P-V diagram for Avgas with no assumptions and using port fuel injection and direct injection.

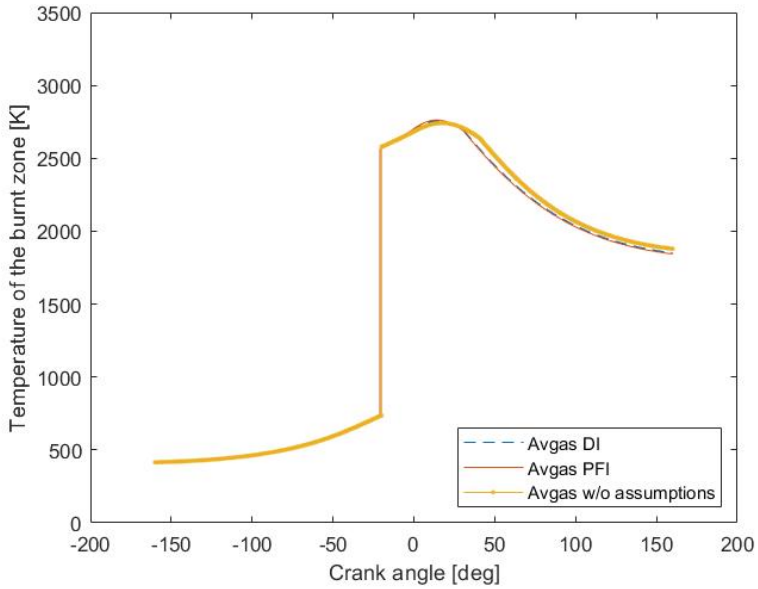

Figure 8.2: Predicted temperature profile for Avgas with no assumptions using port fuel injection and direct injection.

In Figures 8.3 and 8.4 the P-V diagram and temperature profile for hydrogen combustion are given. One scenario uses hydrogen without taking into account the assumptions, one scenario with port fuel injection and one scenario with direct injection.

The pressure results for the scenario without assumptions and the scenario with port fuel injection are similar, while for the temperature results a small deviation can be seen. A higher peak temperature is seen for the scenario without assumptions, which can be attributed to the larger equivalence ratio. A significant difference in pressure can be seen when comparing port fuel injection to direct injection, which can be attributed to the 46% increase in pressure before compression. This leads to a higher amount of combustable mixture and hence a higher peak pressure. This also leads to a higher pressure before combustion is initiated, which does not represent the real life situation. It is therefore expected that the peak pressure for the actual engine is lower. It is interesting to see that the peak pressure approximately doubles compared to Avgas, which is a significant increase and should be further researched.

The increase in peak pressure is not represented in the peak temperature, which is almost similar for port fuel injection and direct injection, as can be seen in Table 8.3. The increase in pressure is cancelled out by the increase in combustable mixture, as can be seen from Equation 6.21.

It was observed that the burn duration used for the Avgas prediction was too high. This means that the burn duration used for hydrogen is also too high, as it is derived from the burn duration for Avgas. This decrease in burn duration will lead to an even higher peak pressure and an increase in power. To accurately quantify the peak pressure, the real burn duration should be quantified.

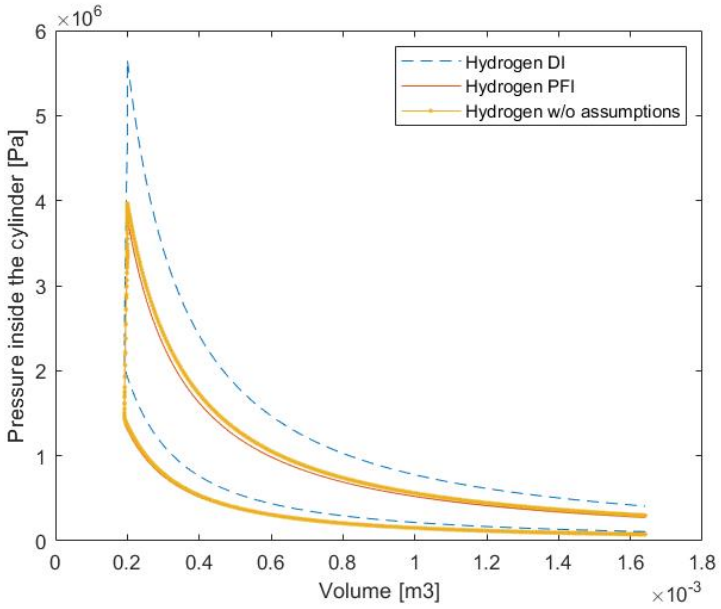

Figure 8.3: Predicted P-V diagram for hydrogen with no assumptions and using port fuel injection and direct injection.

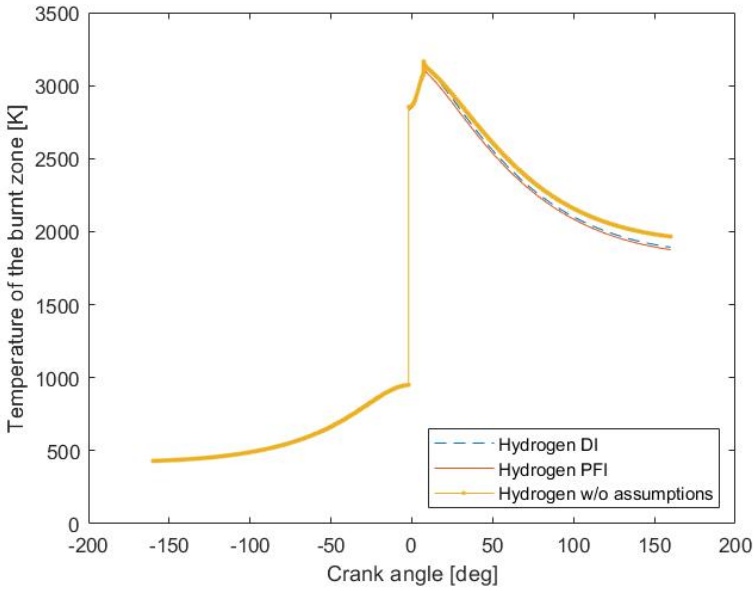

Figure 8.4: Predicted temperature profile for hydrogen with no assumptions and using port fuel injection and direct injection.

Figures 8.5 and 8.6 show the P-V diagram and temperature profile for the engine operating on both fuels with a port fuel injection system. The increase in pressure and temperature for hydrogen is clear, as well as the highly angular profile for hydrogen compared to Avgas. While for Avgas the pressure changes smoothly with volume and the temperature changes smoothly with crank angle, for hydrogen there are sudden changes. These sudden changes could indicate rough operation of the engine, ultimately causing engine failure.

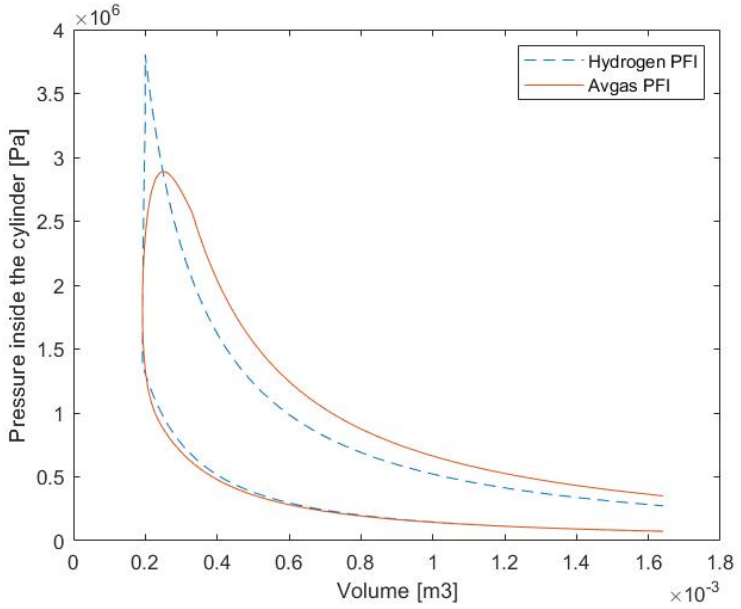

Figure 8.5: Predicted P-V diagram for Avgas and hydrogen combustion using port fuel injection.

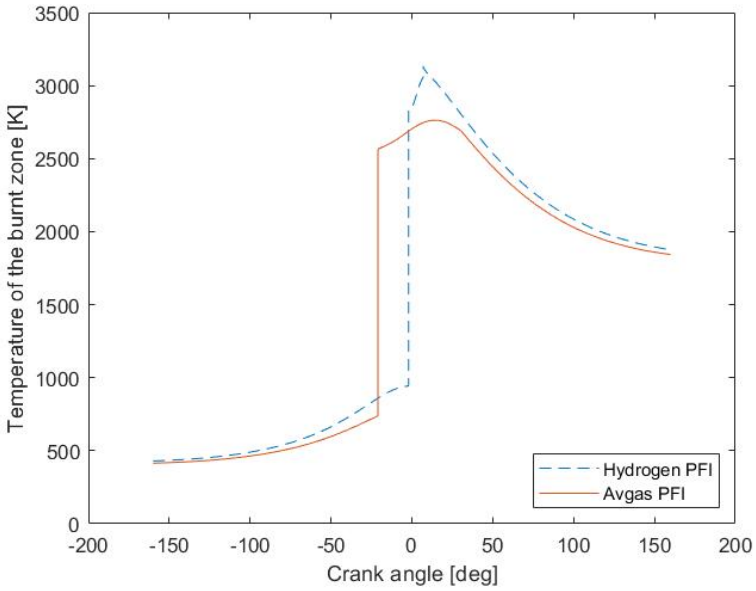

Figure 8.6: Predicted temperature profile for Avgas and hydrogen combustion using port fuel injection.

Figures 8.7 and 8.8 show the same scenarios as above, now with the direct injection system. The difference in peak pressure between Avgas and hydrogen increases, as expected, and changes occur even more suddenly for hydrogen compared to port fuel injection.

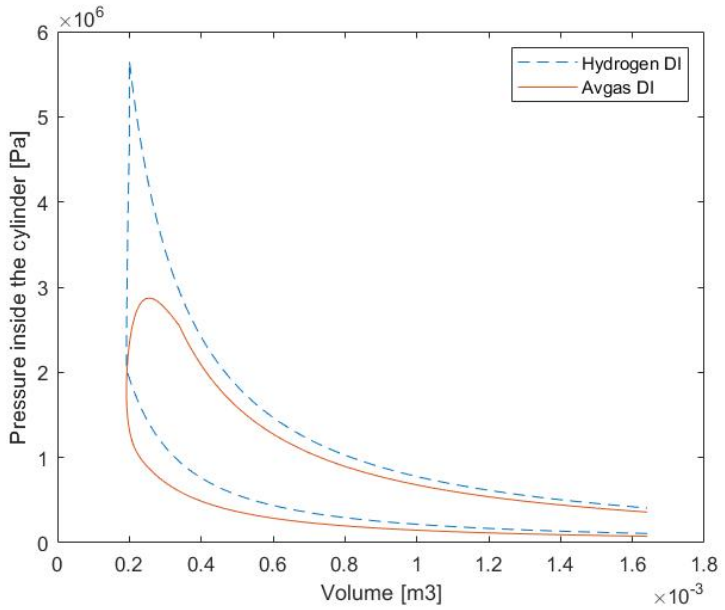

Figure 8.7: Predicted P-V diagram for Avgas and hydrogen combustion using direct injection.

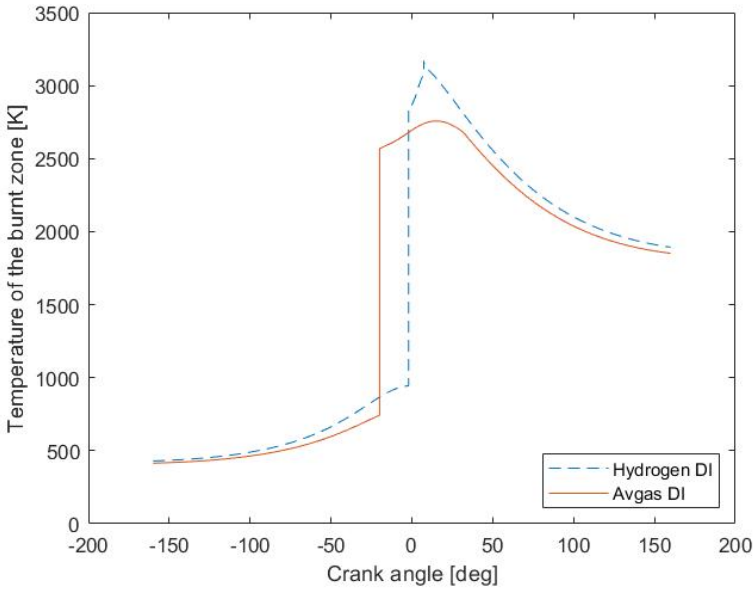

Figure 8.8: Predicted temperature profile for Avgas and hydrogen combustion using direct injection.

8.1.4. COMPARISON TO LITERATURE

To gain better understanding of the accuracy of the results obtained by the preliminary predictions, these predictions are compared to results found in literature.

C.M. White et al. [67] suggests that an engine operating on hydrogen with a carburettor of port fuel injection system compared to an engine operating on gasoline with the same fuel delivery system develops approximately 15% less power. An engine operating on hydrogen with a direct fuel injection system develops approximately 15% more power. The predictions show a power decrease for hydrogen port fuel injection of 22%, and a power increase for hydrogen direct injection of 14%. The power for hydrogen port fuel injection is on the low side, but not unreasonable, which indicates that the results by Chemkin are reliable.

S.J. Lee et al. [68] gives the indicated mean pressure (IMEP) and peak pressure for an engine with port fuel injection, operating on both gasoline and hydrogen. An IMEP of 1.14 MPa is found for gasoline, while an IMEP of 0.92 MPa is found for hydrogen. The IMEP can be used to calculate the power of the engine using the relation as described in Equation 8.1, where n_c is the number of revolutions per power stroke (for a four-stroke engine this is equal to 2), V_d is the displacement volume of the engine and N is the engine speed in revolutions per second. For the engine used by S.J. Lee et al., the displacement volume is 0.488 L and the engine speed is 1500 RPM. This gives a power of 6.96 kW for the engine operating on gasoline and 5.61 kW for the engine operating on hydrogen. This is a decrease of 19% for hydrogen combustion, similar to the Lycoming IO-360-A1B6 engine.

$$IMEP\ [Pa] = \frac{Pn_c}{V_d N} \tag{8.1}$$

For gasoline combustion, a peak pressure of 3.92 MPa is found, while for hydrogen a peak pressure of 5.08 MPa is found. This is an increase of 29.6% for hydrogen combustion. For the Lycoming IO-360-A1B6 engine a similar increase of 31.8% is found, indicating that the results are reliable.

No literature could be found on the pressure for direction injection and the temperature. The accuracy of the peak pressure for hydrogen direct injection thus remains unknown and validation of these results is necessary.

8.2. Risk of Catastrophic Failure

The peak temperature of the gas inside the cylinder does not directly lead to issues. The subsequent temperature of the cylinder wall and cylinder head does. To assess the impact of the increased peak temperature for hydrogen combustion on the cylinder, the cylinder wall and cylinder head temperature should be modelled. This is outside the scope of this research. This does not mean that the results for the peak temperature cannot be used. A higher peak temperature inevitably leads to a higher cylinder wall and cylinder head temperature, especially in combination with the lower quenching distance of hydrogen.

Practical experience shows that an aircraft engine has a safety margin of approximately 2.8 - 3.0. This means that the engine can handle a power 2.8 to 3.0 times as high as the rated power. This is not directly linked to the peak pressure and peak temperature, but does imply that the engine is able to withstand (much) higher pressures and temperatures than originally present. The increase in peak pressure and peak temperature when operating on hydrogen might thus not cause direct issues.

To fully understand the implications of the safety margins on the peak pressure and peak temperature, a new simulation should be performed for the engine operating on Avgas, with a power 2.8 times as high as the current simulations. The increase in power can be achieved with a combination of an increase in pressure before compression and an increase in engine speed. Some iterations will be necessary to obtain the desired power. The subsequent peak pressure and peak temperature can be compared to the peak pressure and peak temperature for hydrogen, and conclusions on whether these lie within the safety margins can be formed.

When operating above the rated power, the lifespan of the engine is shortened. At this stage of the research, the lifespan of the engine is not yet relevant. However, it is important to take this into account when moving towards next research phases.

8.3. Risk Mitigation

At this point, it is unclear whether the peak pressure and peak temperature lie within the safety margins. Therefore, several strategies for decreasing the probability of catastrophic engine failure due to an increase in pressure and/or temperature inside the cylinders are proposed. These strategies can be used to mitigate the risk of catastrophic failure. Two categories of risk mitigation are considered: changing the operating conditions and modifying the engine itself.

8.3.1. Decreasing the power

To decrease the peak pressure and peak temperature, the throttle and/or equivalence ratio can be decreased, subsequently decreasing the power. The operator's manual of the Lycoming engine suggests a power of 65 - 75% of the maximum power to sustain cruise. This means that cruise can be sustained with a decrease in power of 25 - 35%. However, when decreasing the power by this amount, take-off is affected considerably.

The implications on take-off are not as straightforward as for cruise. The consequences of decreasing the power can only be evaluated in combination with an aircraft, not as a stand-alone engine. For the Lycoming IO-360-A1B6 engine, there is no reference aircraft. Therefore, the results are generalised and the Cessna Skymaster is taken as a reference. The Cessna Skymaster has two Continental IO-360-C engines. The Continental IO-360-C engine is a six-cylinder engine with a rated power of 160 kW, which means 320 kW is available for take-off.

Comparing the Cessna Skymaster to other aircraft, such as the Cessna O-2 Skymaster (which is a Cessna Skymaster modified for military purposes), it is found that, with the same engines, a higher MTOW can be realised. The original Skymaster has an MTOW of 1996 kg, while the O-2 has an MTOW of 2449 kg. Massachusetts Institute of Technology [69] suggests a relation between power and thrust as given in Equation 8.2, with P_{shaft} the shaft power, T_f the thrust, r_{prop} the radius of the propeller and η_v the profile propeller efficiency. Given that the thrust must be larger than the drag to allow for acceleration (which is a requirement for take-off), Equation 8.3 can be derived. Here, W_{AC} is the weight of the aircraft, C_D is the drag coefficient and C_L is the lift coefficient.

$$P_{shaft} = \frac{T_f^{3/2}}{\left(2\pi\rho\right)^{1/2}} \frac{1}{r_{prop}} \frac{1}{\eta_v} \tag{8.2}$$

$$P_{shaft} > \frac{\left(W_{AC}\frac{C_D}{C_L}\right)^{3/2}}{\left(2\pi\rho\right)^{1/2}}\frac{1}{r_{prop}}\frac{1}{\eta_v} \tag{8.3}$$

Equation 8.3 shows that the shaft power is related to the weight of the aircraft with a power of 3/2. This means that, for a lower weight, there is a lower required power. Compared to the Cessna O-2, the original Skymaster has a decrease in take-off weight of 18.5% (leaving a total of 81.5%). The minimum required power for take-off thus decreases with $1-\left(81.5^{3/2}\right) = 26.4\%$. This means that, for the Cessna Skymaster, the power during take-off can be decreased to a minimum of 73.6% (giving a power of 118 kW for each engine), for take-off to still be possible. Decreasing the power (and hence the thrust) does mean that the acceleration of the aircraft decreases, and the take-off distance increases.

8.3.2. MODIFICATIONS TO THE ENGINE

When looking at the equation governing convective heat transfer as given in Equation 8.4, there are multiple ways to promote heat loss from the engine to the surroundings. The first is by increasing the surface area of the engine, which can be achieved by changing or increasing the amount of cooling fins on the engine.

The second is by increasing the difference between the engine temperature T_{eng} and the cooling air temperature T_{cool}, which is achieved by decreasing the temperature of the cooling air.

A third method is by increasing the heat transfer coefficient. The heat transfer coefficient is dependent on the Nusselt number, which is in turn dependent on the Reynolds number, given by Equation 8.5, where L is a characteristic length. Changing the cooling medium (which in turn changes the density and viscosity) or increasing the cooling medium velocity, increases the heat transfer coefficient and hence promotes cooling.

$$Q = h_c A\left(T_{eng} - T_{cool}\right) \tag{8.4}$$

$$Re = \frac{\rho L v}{\mu} \tag{8.5}$$

Another method to promote cooling is by increasing the heat loss to the oil. This can either be done by increasing the amount of oil or by changing the oil to one with a higher heat capacity.

A solution which could lead to a decrease in peak pressure in the cylinder, is to inject small amounts of fuel into the cylinder at multiple times. This way, multiple, lower pressure peaks occur, decreasing the peak pressure in the engine. However, this might lead to other issues such as knock. Therefore, more research is needed.

Alternatively, the mechanical strength of the engine can be increased by replacing critical parts, although this is a drastic and impractical solution.

9
EXPERIMENTAL DESIGN FOR CHEMKIN VALIDATION

In Section 7.6 it was mentioned that to validate Chemkin (and perform a subsequent risk analysis) experimental data is needed. It is suggested to perform validation for Avgas only, to increase the accuracy of the predicted peak pressure and peak temperature, and subsequently increase the accuracy of the risk analysis. In this chapter, experiments for validation of the assumptions as given in Section 6.7 are proposed. In a later phase of the project, these experiments can also be used to validate for hydrogen, to allow for the use of Chemkin for other applications such as engine mapping.

For the experiments, standard operating conditions are chosen within the standard flight range, and the throttle and equivalence ratio corresponding to these power outputs are used as inputs. Note that the experiments should be performed in sequence to isolate the effects of the assumptions.

9.1. FUEL INTRODUCTION STRATEGY

The effect of the fuel introduction strategy and homogeneity on the results can be evaluated by comparing the pressure, temperature and power for the engine with a port fuel injection system to the pressure, temperature and power for the engine with a direct fuel injection system. The power is measured by the dynamometer, while the pressure is measured by a pressure sensor. For the measurements with port fuel injection, a pressure sensor can be installed in the pre-existing hole of the second spark plug. For the measurements with direct injection, there are two options. Either another hole is drilled to accommodate the pressure sensor, or the spark plug is replaced by one with a built in pressure sensor (such as provided by Kistler [70]).

Sensors for direct measurement of the gas temperature inside the cylinder are not common. An indication of the gas temperature can be found using three other measurements, the Cylinder Head Temperature (CHT), the Exhaust Gas Temperature (EGT) and the cooling oil temperature. For the CHT and cooling oil temperature, it is important that the engine is run under the same conditions (cooling air temperature, run history) to avoid external factors changing the temperature. Using these methods, only a qualitative comparison can be made for the temperature. By comparing the power, pressure and temperature for both fuel introduction strategies, conclusions can be formed on the influence of the fuel introduction strategy and homogeneity on the pressure, temperature and power.

9.2. RUNNING THE ENGINE WITHOUT HEAT RELEASE

The assumption of the ideal gas law, the heat transfer parameters and the gas exchange loss and friction loss are relatively independent from the combustion phase. The engine is run without heat release to isolate the effects of these assumptions. At low loads (and hence low temperature) the deviation from the ideal gas law, the gas exchange loss and friction loss increases. It is therefore advised to perform the optimisation for the heat transfer parameters at high loads, to minimise the effect of the other assumptions.

Ideally, the heat transfer parameters are optimised for each operating condition. To optimise the heat transfer parameters, the engine should be run for different operating conditions for high load. Ideally, one would measure the temperature profile. Since gas temperature sensors are not common, the pressure profile can be used. The heat transfer parameters are tweaked to obtain the smallest error between the pressure profile as predicted by Chemkin and the actual pressure profile, for different operating conditions. The change in optimum heat transfer parameters with operating condition is monitored to form conclusions on the need to change the heat transfer parameters with operating conditions. As evident from Chapter 7, a change in heat transfer parameters (apart from heat transfer parameter b) does not have a large effect on the power, peak pressure and peak temperature. Therefore, optimisation of the Woschni heat transfer parameters is given a low priority.

Large deviations between the pressure profile as predicted by Chemkin and the real pressure profile at low loads are governed by the gas exchange loss and friction loss. Different operating conditions at low load are chosen and the real pressure profile is compared to the predicted pressure profile to find the gas exchange loss and friction loss. These two are expressed in one single loss.

The ideal gas law governs the relationship between the pressure and temperature inside the cylinder. The deviations in pressure profile have been accounted for with the heat transfer parameters and the gas exchange loss and friction loss. Comparing the temperature profile as predicted by Chemkin (with the heat transfer and losses accounted for) to the real temperature profile, the effect of the ideal gas law on the relationship between the pressure and temperature can be found. Since the temperature profile is not known, the Exhaust Gas Temperature can be used and compared to the predicted gas temperature at the end of the expansion phase.

9.3. Measuring the build up of mass in the crankcase

Blowby is expected to occur during two phases, the compression stroke and the power stroke. During the compression stroke, the content of the blowby is mostly air and fuel, while during the power stroke this is combustion products, air and fuel. The amount of fuel lost due to blowby is of interest. Assuming that the composition of the blowby is equal to the composition of the cylinder content, the amount of fuel lost due to blowby can be determined by measuring the amount of O_2 in the crankcase ventilation using the gas analyser as elaborated upon in Section 4.5.1.

9.4. Determination of the Wiebe function

The Wiebe function governs the mass transfer from the unburnt to the burnt zone during combustion and the parameters should ideally be optimised for each operating condition. As can be seen in Chapter 7, the Wiebe parameters have a large influence on the power, peak pressure and peak temperature. The optimisation of these parameters is thus essential. Ideally, one would measure the mass of the burnt zone to determine the ratio of burnt zone mass to total mass. This is not possible, and hence another method must be found to determine the Wiebe function parameters. The Wiebe function parameters can be modified such that the pressure profile during combustion as predicted by Chemkin matches the real pressure profile in the cylinder, as suggested by Y. Shiao and J.J. Moskwa [71]. This process is tedious and requires running Chemkin often to find the optimum Wiebe function parameters.

Instead of separately determining the ignition delay, the spark timing can be used as the start of combustion in the Wiebe function and the ignition delay can be incorporated into the other Wiebe function parameters, as suggested by F. Lindström et al. [72].

When determining the Wiebe function parameters by matching the predicted pressure profile during the combustion phase to the real pressure profile, the heat transfer from the burnt zone and the unburnt zone is indirectly incorporated. As the temperature of the burnt zone decreases due to the heat transfer, so does the pressure, which is in turn expressed in the Wiebe function parameters. When a different method is found to determine the Wiebe function parameters, the effect of the heat transfer on the pressure profile can be found by comparing the predicted pressure profile (with the optimised Wiebe function) to the experimental pressure profile. This effect can then be translated to an effect on the temperature through the governing equations of the combustion phase.

9.5. EXPERIMENTAL OVERVIEW

An overview of the parameters which are needed for the validation together with the parameters which can actually be measured during experiments is given in Table 9.1. x indicates the parameters which are needed and can be measured. o indicates which alternatives can be used to indirectly measure the effect of the assumption on the results. The most critical experiments are highlighted in green.

Table 9.1: Overview of the parameters to be measured for the validation experiments.

		P	**p**	**EGT**	**CGT**	T_{oil}	**Blowby**
Fuel introduction & homogeneity	P	x					
	p		x				
	T			o	o	o	
Ideal gas law	p		x				
	T			o			
Heat transfer	T		o				
Gas exchange and friction loss	P	x					
	p		x				
Blowby	Blowby						x
Wiebe function	T		o				

10
CONCLUDING REMARKS PART II

Changing the fuel from Avgas to hydrogen comes with many challenges. The second part of this thesis focused on the modelling of the engine for both fuels and the effect of the change in fuel on the pressure and temperature inside the cylinders.

10.1. CONCLUSIONS

Chemkin is used to model the engine and to predict the peak pressure, peak temperature and power of the engine for Avgas, hydrogen, for both port fuel injection and direct injection.

In Chemkin the combustion chamber is modelled as a two-zone model, consisting of an unburnt and a burnt zone. The mass transfer between the unburnt and burnt zone is governed by the Wiebe function and the heat transfer to the cylinder walls is governed by the Woschni heat transfer correlation. Both the Wiebe function and heat transfer parameters need optimisation for the specific lay-out of the engine, the fuel and the operating conditions. From the sensitivity analysis, it is clear that most of the heat transfer parameters have little or no effect on the power, peak pressure and peak temperature. The engine lay-out (except the compression ratio) and engine speed have little effect on the peak pressure, and the only operating parameter with a significant influence on the peak temperature is the equivalence ratio. Optimisation of the Wiebe parameters, most notably the burn duration, has a high priority.

Due to the assumptions Chemkin makes, deviations of the results from the actual engine are inevitable. To ensure accurate results from Chemkin (and hence perform a risk analysis necessary for certification), these deviations must be quantified with validation experiments. However, to perform the experiments, certification is needed. Therefore, preliminary predictions, based on the estimated effects of the assumptions, are made. The uncertainty of these predictions is incorporated into the risk analysis.

Preliminary predictions are made for Avgas and hydrogen, using both port fuel injection and direct injection. The power output of the predictions for Avgas is too low (23 kW where 28 kW is expected), which can be attributed to the Wiebe function which is not optimised at this point. The effect of the assumptions on the results is significant, which can probably be attributed to the change in burn duration.

When changing the fuel to hydrogen, significant changes are seen. With port fuel injection, hydrogen gives a peak pressure increase of 32%, a peak temperature increase of 13% and a power decrease of 22% compared to Avgas. The difference between port fuel injection and direct injection is much larger than for Avgas, with an increase in peak pressure of 97%, an increase in peak temperature of 15% and an increase in power of 14% compared to Avgas. The sharp increase in pressure can be explained by the increase in pressure before compression, which is applied to account for the increase in volumetric efficiency when using direct injection. The increase in pressure before compression also leads to an increase in pressure during the compression phase, which is not the case in the actual engine. Therefore the real peak pressure will probably be lower. As the Wiebe function is not optimised, this might change the peak pressure considerably. Hydrogen combustion shows sudden changes in pressure and temperature, which could indicate rough operation of the engine, and could lead to engine failure.

The safety margins of the engine allow for an increase in temperature and pressure inside the cylinder. At this point, catastrophic failure seems unlikely. However, the exact implications are unknown at this point. To fully understand the implications of the safety margins on the peak pressure and peak temperature, a new simulation in Chemkin is proposed. The power of the engine operating on Avgas should be increased to 2.8 times the power found during the simulations, and the subsequent peak temperature and peak pressure can be assumed to be the maximum pressure and temperature for this engine.

To mitigate the risk of catastrophic failure, two strategies are proposed: decreasing the power and modifying the engine. The power can be decreased with a maximum of 26.4% to still allow for take-off. However, decreasing the power increases the take-off distance. If this is not desirable, several modifications to the engine can be made, such as changing the cooling fins, decreasing the temperature of the cooling air, changing the cooling medium or increasing the heat transfer to the oil. The peak pressure can be decreased by introducing multi-injection, although adverse effects are expected and should be further researched.

To increase the accuracy of the risk analysis, validation can be performed for the engine operating on Avgas. Additionally, validation can be performed for the engine operating on hydrogen in a later phase of the project, to allow for the use of Chemkin for other applications, such as engine mapping. Four experiments are proposed. The first experiment is the comparison between port fuel injection and direct injection. Chemkin assumes a homogeneous fuel-air mixture to be present from the start of the compression phase, which is not accurate, especially for direct injection. For the second experiment, the engine is run without initiating ignition, to assess the effect of the heat transfer parameters, the ideal gas law and the gas exchange and friction loss on the pressure, temperature and power. The third experiment covers the measuring of blowby and the fourth experiment covers the determination of the Wiebe function parameters.

10.2. RECOMMENDATIONS

The final step in determining the risk of catastrophic failure is to perform a final simulation in Chemkin. The Lycoming IO-360-A1B6 engine should be modelled for Avgas, with a power 2.8 times as high as the current simulation. The increase in power can be achieved with a combination of an increase in pressure before compression and an increase in engine speed. The subsequent peak pressure and peak temperature can be assumed to be the maximum pressure and temperature for this engine.

To further increase the accuracy of the risk analysis, Chemkin can be validated for Avgas using the experiments as proposed in Chapter 9. Specifically the effect of the fuel introduction strategy and the gas exchange and friction loss should be quantified, and the Wiebe function should be optimised. The same experiments can be used to validate for hydrogen in later phases of the project. Then, Chemkin can be used for different purposes, such as engine mapping or full engine modelling in Ansys forte.

When modelling the engine in Ansys Forte, some of the assumptions made by Chemkin can also be modelled, such as the effect of the fuel introduction strategy and the gas exchange loss. However, the Wiebe function still governs the combustion phase, and thus has to be optimised to obtain accurate results from the engine model.

In this thesis, the focus lies on the power, pressure and temperature. While the pressure is a direct indicator of the forces inside the cylinders, the gas temperature is not a direct indicator of the temperature of the engine structure. To obtain useful conclusions as to the effect of the transition to hydrogen on the structural integrity of the engine, temperature modelling of the engine must thus be performed with an accurate heat transfer coefficient. Ansys Forte can be used to this purpose.

With the above-mentioned recommendations, the current research question (What is the effect of the transition to hydrogen on the pressure and temperature inside the cylinders of the Lycoming IO-360-A1B6 engine?) can be answered. The next step in the project would be to further research the high impact events as mentioned in Chapter 3, to gain a larger understanding of the risks associated with testing. This is essential for the project, as permits will not be issued without adequate risk identification and mitigation.

BIBLIOGRAPHY

[1] International Civil Aviation Organization. *Future of Aviation*. Retrieved 9-6-2020 from https://www.icao.int/Meetings/FutureOfAviation/Pages/default.aspx.

[2] United Nations. *What is the Paris Agreement?* Retrieved 9-6-2020 from https://unfccc.int/process-and-meetings/the-paris-agreement/what-is-the-paris-agreement.

[3] W. Frijters. "A Flying Test Bed for Sustainable Aviation: Hydrogen Propulsion". Delft University of Technology, 2021.

[4] L. Ferreira Bessa Babo. "Simulation and Optimization of a Hydrogen Internal Combustion Engine". Universidade do Porto, 2016.

[5] H.L. Yip et al. "A Review of Hydrogen Direct Injection for Internal Combustion Engines: Towards Carbon-Free Combustion". In: *Applied Sciences* 9 (2019). https://doi.org/10.3390/app9224842.

[6] K. Sapru et al. *Development of Advanced Small Hydrogen Engine*. Tech. rep. Energy Conversion Devices, Inc., 2010.

[7] T. Drennen et al. "Conversion of a Gasoline Internal Combustion Engine into a Hydrogen Engine". In: *American Society for Engineering Education* (2012).

[8] C. Harper and J.J. Liccione. *Toxicological Profile for Gasoline*. Tech. rep. U.S. Department of Health and Human Services, 1995.

[9] P.J. Landrigan. *The Worlwide Problem of Lead in Petrol*. Tech. rep. World Health Organization, 2002.

[10] T.I. Yacovitch et al. *Exhaust Emissions from In-use General Aviation Aircraft*. Tech. rep. Airport Cooperative Research Program, 2016.

[11] Exxon Mobil Corporation. *ExxonMobil Avgas*. 2019.

[12] S. Verhelst and T. Wallner. "Hydrogen-fueled Internal Combustion Engines". In: *Progress in Energy and Combustion Science* 35 (2009). https://doi.org/10.1016/j.pecs.2009.08.001.

[13] Dutch Electric Aviation Centre. *Cessna Skymaster*. Retrieved 29-10-2020 from https://deac-teuge.nl/diensten/.

[14] W. W. Pulkrabek. *Engineering Fundmentals of the Internal Combustion Engine*. Prentice Hall.

[15] S. Dannana. *What is Valve Timing Diagram in Four-stroke Engines?* Retrieved 30-7-2020 from https://extrudesign.com/valve-timing-diagram-in-four-stroke-engines/.

[16] College of the Desert. *Hydrogen Fuel Cell Engines and Related Technologies*. Tech. rep. Office of Energy Efficiency and Renewable Energy, 2001.

[17] Y.S.H. Najjar. "Hydrogen safety: The road toward green technology". In: *International Journal of Hydrogen Energy* 38 (2013). https://doi.org/10.1016/j.ijhydene.2013.05.126.

[18] "Advances in Internal Combustion Engine Research". In: https://doi.org/10.1007/978-981-10-7575-9_6. Springer, 2018. Chap. Hydrogen-Enriched Comperessed Natural Gas: An Alternate Fuel for IC Engines.

[19] A. Beerbower and D.F. Greene. "The Behavior of Lubricating Oils in Inert Gas Atmospheres". In: *Tribology Transactions* 4.1 (2008). https://doi.org/10.1080/05698196108972422.

[20] Lycoming. *IO-360-A1B6*. Retrieved 16-11-2020 from https://www.lycoming.com/node/17361.

[21] B. Nagalingam et al. "Performance Study Using Natural Gas, Hydrogen-supplemented Natural Gas and Hydrogen in AVL Research Engine". In: *International Journal of Hydrogen Energy* 8.9 (1983). https://doi.org/10.1016/0360-3199(83)90181-7.

[22] A.P. Singh et al. *Alternative Fuels and Their Utilization Strategies in Internal Combustion Engines*. Springer, 2020.

[23] N. Sharma. "Knock Model Evaluation – Gas Engine". KTH Royal Institute of Technology, 2018.

[24] Rijksoverheid. *Arbeidsomstandighedenbesluit*. Retrieved 20-11-2020 from https://wetten.overheid.nl/BWBR0008498/2020-07-01.

[25] Shell Trading Canada. *Safety Data Sheet Avgas 100LL*. 2020.

[26] Linde Inc. *Hydrogen, Compressed: Safety Data Sheet*. 2020.

[27] MoTeC. *GPRDI*. Retrieved 28-10-2020 from https://www.motec.com.au/gprdi-m1/gprdi-m1-ov/.

[28] Bosch. *Gasoline Port Fuel Injection*. Retrieved 24-11-2020 from https://www.bosch-mobility-solutions.com/en/products-and-services/passenger-cars-and-light-commercial-vehicles/powertrain-systems/gasoline-port-fuel-injection/.

[29] Skill-Lync. *How does Common Rail Direct Injection (CRDI) work?* Retrieved 24-11-2020 from https://www.youtube.com/watch?v=0ZYtDkn0b9g.

[30] Skill-Lync. *Magneto Ignition System*. Retrieved 24-11-2020 from https://www.youtube.com/watch?v=N-wA4iBDr9o.

[31] NASA Earth Observatory. *Effects of Changing the Carbon Cycle*. Retrieved 25-11-2020 from https://earthobservatory.nasa.gov/features/CarbonCycle/page5.php.

[32] T.F. Stocker et al. *Climate Change 2013: The Physical Science Basis*. Tech. rep. IPCC, 2013.

[33] Bridge Analyzers Inc. *Model 900503 Product Description and Specifications*. 2016.

[34] Figaro Engineering Inc. *Operating Principle NDIR Type*. Retrieved 02-12-2020 from https://www.figaro.co.jp/en/technicalinfo/principle/ndir-type.html.

[35] Figaro Engineering Inc. *Operating Principle Electrochemical Type*. Retrieved 02-12-2020 from https://www.figaro.co.jp/en/technicalinfo/principle/electrochemical-type.html.

[36] ElectricalGang. *What is Eddy Current Dynamometer?* Retrieved 22-04-2021 from https://electricalgang.com/eddy-current-dynamometer/.

[37] H.J. Dadt. *Technical Specification Eddy-Current Dynamometer W Series*. Schenck Pegasus GmbH. 2001.

[38] Waternet. *Tap water hardness in and around Amsterdam*. Retrieved 02-12-2020 from https://www.waternet.nl/en/service-and-contact/tap-water/tap-water-hardness/.

[39] R.J. Kee et al. *Chemkin-III: A FORTRAN Chemical Kinetics Package for the Analysis of Gas-phase Chemical and Plasma Kinetics*. Sandia National Laboratories. 1996.

[40] *ANSYS Chemkin Theory Manual 17.0*. Reaction Design. 2015.

[41] G. Woschni. "A Universally Applicable Equation for the Instantaneous Heat Transfer Coefficient in the Internal Combustion Engine". In: *SAE Transactions* 76 (1968).

[42] J.I. Ghojel. "Review of the Development and Applications of the Wiebe Function: a Tribute to the Contribution of Ivan Wiebe to Engine Research". In: *International Journal of Engine Research* 11 (2010). https://doi.org/10.1243/14680874JER06510.

[43] J. Serras-Pereira et al. "An Analysis of the Combustion Behavior of Ethanol, Butanol, Iso-Octane, Gasoline, and Methane in a Direct-Injection Spark-Ignition Research Engine". In: *Combustion Science and Technology* 185 (2013). https://doi.org/10.1080/00102202.2012.728650.

[44] *Handbook of Aviation Fuel Properties*. Coordinating Research Council. 1983.

[45] X. Cheng et al. "A Review of PEM Hydrogen Fuel Cell Contamination: Impacts, Mechanisms, and Mitigation". In: *Journal of Power Sources* 165 (2007). https://doi.org/10.1016/j.jpowsour.2006.12.012.

[46] P. Dimitriou. "Air-fuel Homogeneity Effects on Direct Injection Diesel Engine Performance and Emission". University of Sussex, 2015.

[47] F.M. White. *Viscous Fluid Flow*. 3rd ed. McGraw Hill, 2006.

[48] S. Chapman and T.G. Cowling. *The Mathematical Theory of Non-Uniform Gases*. Cambridge University Press, 1970.

[49] Brown et al. *Real Gases - Deviation from Ideal Behaviour*. Retrieved 22-03-2021 from https://chem.libretexts.org/@go/page/21767. 2021.

[50] Brown et al. *van der Waal's Constants for Real Gases*. Retrieved 22-03-2021 from https://chem.libretexts.org/@go/page/15729. 2020.

[51] C.H. Marchi and L.K. Araki. “Evaluation of Chemical Equilibrium and Non-Equilibrium Properties for LOX/LH2 Reaction Schemes”. In: *Journal of Aerospace Technology and Management* 7 (2015). https://doi.org/10.5028/jatm.v7i1.426.

[52] G.A. Lavoie et al. “Experimental and Theoretical Study of Nitric Oxide Formation in Internal Combustion Engines”. In: *Combustion Science and Technology* 1 (1970). https://doi.org/10.1080/00102206908952211.

[53] C.D. Rakopoulos et al. “Development and Validation of a Comprehensive Two-zone Model for Combustion and Emissions Formation in a DI Diesel Engine”. In: *International Journal of Energy Research* 27 (2003). https://doi.org/10.1002/er.939.

[54] R.S. Benson et al. “A Simulation Model Including Intake and Exhaust Systems for a Single Cylinder Four-Stroke Cycle Spark Ignition Engine”. In: *International Journal of Mechanical Sciences* 17 (1975). https://doi.org/10.1016/0020-7403(75)90002-8.

[55] F. Bonatesta et al. “Burn Angles and Form Factors for Wiebe Function Fits to Mass Fraction Burned Curves of a Spark Ignition Engine with Variable Valve Timing”. In: *International Journal of Engine Research* 11 (2010). https://doi.org/10.1243/14680874JER05009.

[56] N. Septivani and B.W. Riyandwita. “Spark Ignition Engine Modeling for in-Cylinder Pressure and Temperature Prediction Using Simulink”. In: *MATEC Web of Conferences* 204 (2018).

[57] The Engineering ToolBox. *Air - Prandtl Number*. Retrieved 23-03-2021 from `https://www.engineeringtoolbox.com/air-prandtl-number-viscosity-heat-capacity-thermal-conductivity-d_2009.html`.

[58] The Engineering ToolBox. *Carbon dioxide - Prandtl Number*. Retrieved 23-03-2021 from `https://www.engineeringtoolbox.com/carbon-dioxide-prandtl-number-viscosity-heat-capacity-thermal-conductivity-d_2024.html`.

[59] The Engineering ToolBox. *Water - Prandtl Number*. Retrieved 23-03-2021 from `https://www.engineeringtoolbox.com/water-steam-Prandtl-number-d_2059.html`.

[60] The Engineering ToolBox. *Nitrogen - Prandtl Number*. Retrieved 23-03-2021 from `https://www.engineeringtoolbox.com/nitrogen-N2-Prandtl-number-temperature-pressure-d_2102.html`.

[61] J. Stokes et al. “A Gasoline Engine Concept for Improved Fuel Economy -The Lean Boost System”. In: *International Fuels & Lubricants Meeting & Exposition* (2000). https://doi.org/10.4271/2000-01-2902.

[62] Z. Zhao et al. “Correlations for the Ignition Delay Times of Hydrogen/Air Mixtures”. In: *Chinese Science Bulletin* 56 (2011). https://doi.org/10.1007/s11434-010-4345-3.

[63] *Operator’s Manual Lycoming*. Lycoming. 2005.

[64] S.G. Davis and C.K. Law. “Laminar Flame Speeds and Oxidation Kinetics of iso-Octane-Air and n-Heptane-Air Flames”. In: *Symposium on Combustion* 27 (1998). https://doi.org/10.1016/S0082-0784(98)80442-6.

[65] Q. Li et al. “Laminar Flame Characteristics of C1–C5 Primary Alcohol-Isooctane Blends at Elevated Temperature”. In: *Energies* 9 (2016). https://doi.org/10.3390/en9070511.

[66] C. Dong et al. “On the Laminar Flame Speed of Hydrogen, Carbon Monoxide, and Natural Gas Mixtures with Air: Insights for a Dual-fuel Polygeneration System”. In: *Energy Sources, Part A: Recovery, Utilization, and Environmental Effects* 36 (2014). https://doi.org/10.1080/15567036.2010.538806.

[67] C.M. White et al. “The hydrogen-fueled internal combustion engine: a technical review”. In: *International Journal of Hydrogen Energy* 31 (2006). https://doi.org/10.1016/j.ijhydene.2005.12.001.

[68] S.J. Lee et al. “Combustion Characteristics of Intake Port Injection Type Hydrogen Fueled Engine”. In: *International Journal of Hydrogen Energy* 20 (1995). https://doi.org/10.1016/0360-3199(94)00052-2.

[69] Massachusetts Institute of Technology. *Flight Thrust, Power, and Energy Relations*. Retrieved 05-05-2021 from `https://web.mit.edu/16.unified/www/SPRING/systems/Lab_Notes/airpower.pdf`.

[70] Kistler. *New Measuring Spark Plug with miniature Pressure Sensor*. Retrieved 29-3-2021 from `https://www.kistler.com/en/product/type-611xc/?application=7`.

[71] Y. Shiao and J.J. Moskwa. “Cylinder Pressure and Combustion Heat Release Estimation for SI Engine Diagnostics Using Nonlinear Sliding Observers”. In: *IEEE Transactions on Control Systems Technology* 3 (1995). https://doi.org/10.4271/2000-01-2902.

[72] F. Lindström et al. “An Empirical SI Combustion Model Using Laminar Burning Velocity Correlations”. In: *2005 SAE Brasil Fuels & Lubricants Meeting* (2005). https://doi.org/10.4271/2005-01-2106.

A
SAFETY DOCUMENTS

A.1. Safety Analysis Report

Delft University of Technology

Safety Considerations for Developing an H2ICE for Aviation Applications

Thesis

Safety Document

Avgas/Hydrogen test set-up

Authors:
Lina Hosking
Advisors:
Ir. J.A. Melkert
Prof.dr.ir. L.L.M. Veldhuis
V. Klein

May 14, 2021
Conceptual Version

1 Introduction

General introduction of the project.

2 General Project Information

Who is involved, who is responsible for what, who are allowed to be working on the project.

3 Description of the Test Set-Up

General description of the lay-out of the test set-up with some nice technical drawings. Probably also a division into systems.

4 Activity Process Flow Charts

What activities will take place and how?

5 Project Planning

What is the span of the project? When will the experiments take place and for how long?

6 Risk Assessment

Tables with risks and hazards for each system.

7 Measures Taken

The measures taken as given in the Risk Assessment chapter categorised per phase (design, preparation, execution).

A.2. Explosion Safety Report

Delft University of Technology

Safety Considerations for Developing an H2ICE for Aviation Applications

Thesis

ATEX

Avgas/Hydrogen test set-up

Authors:
Lina Hosking
Advisors:
Ir. J.A. Melkert
Prof.dr.ir. L.L.M. Veldhuis
V. Klein

May 14, 2021
v1.1

1 Introduction

This Explosion Safety Document, or ATEX report, is written for the test set-up built as part of the project 'A Flying Test Bed for Sustainable Aviation'. The purpose of the project is to convert one of the engines of a Cessna Skymaster to operate on hydrogen. As a proof of concept, first a Lycoming IO-360-A1B6 engine is converted. The goal of the test set-up is to first test this engine as is (operating on Avgas), after which the engine will be converted to hydrogen and tested again. The goal of this document is to ensure safe operation and mitigate explosion risks. This document will be mostly focused on operation with Avgas, and some recommendations will be done for hydrogen.

In Chapter 2 the physical lay-out of the test set-up is described. Then, in Chapters 3 and 4 the performed activities and used dangerous materials are described. Chapter 6 then gives an assessment of the explosion risk, after which Chapter 5 covers the division of the test set-up into ATEX zones. Finally, Chapter 7 outlines the measures taken to mitigate the risks.

2 Description of the Test Set-Up

3 Description of the Activities

The main activity taking place in the test cell is the testing of the engine. During testing, nobody is present inside the test cell. All testing is done remotely from the control cabin. Other activities, which only take place when the fuel and electricity supply have been shut off, are the placement and removal of the engine, the replacement of fuel and/or oil and inspections of the engine or other testing equipment.

4 Description of Dangerous Materials

The main materials used in the test cell are Avgas, hydrogen and lubricant. Relevant properties of these materials are given below.

4.1 Avgas

Avgas is a blue liquid, consisting of 4-8% alkanes, 2-5% alkenes, 3-7% cycloalkanes, 1-4% cycloalkenes and 20-50% aromatics [2, p.107]. Tetraethyllead is added to increase the octane number. Table 1 gives the most relevant properties of Avgas.

4.2 Hydrogen

Hydrogen is a colourless, odourless gas, stored in compressed state. Platinum is a catalyst for hydrogen combustion. Table 1 gives the most relevant properties of hydrogen.

4.3 Lubricant

Table 1: Properties of the materials present in the test cell. a: Retrieved from [1], b: Retrieved from [4], c: Retrieved from [3], d:.

Property	Unit	Avgas[(a)]	Hydrogen[(c)]	Lubricant[(d)]
Boiling point	°C	24-170	-259.2	
Freezing point	°C	<-58	n.a.	
Flash point	°C	<-37	n.a.	
Autoignition temperature	°C	440	566	
Minimum Energy of Ignition	mJ	0.24[(b)]	0.02[(b)]	
Explosive limit	vol%	1.5-7.6	4-77	
Vapor density (relative to air)	-	>1	0.07	
Storage volume	m^3			

5 Division into Zones

The test set-up can be divided into two parts: the test cell and the control cabin. The ATEX zone classification is given in Table 2. The frequency indicates during what amount of time the formation of an explosive mixture is possible.

Table 2: Overview of ATEX zoning.

Zone	Type of explosion	Frequency
Zone 1	Gas explosion	>10% of time
Zone 2	Gas explosion	0.1 - 10% of time
Zone 3	Gas explosion	<0.1% of time

5.1 Test cell

The test cell is the critical part of the test set-up. The flash point of Avgas is <-37°C, which means vapour can form at any time, with the potential of reaching the lower explosive limit. In the case of a leak, either in the fuel tank, the fuel lines or the engine itself, vapour could escape to the engine surroundings and form an explosive mixture in the test cell. A spark, created by static electricity, could provide enough energy for this mixture to combust. Keeping in mind the narrow explosive window for Avgas and the high m minimum energy of ignition, the test cell is classified as Zone 2.

When Avgas is replaced with hydrogen, a few things change. Due to the higher chance of fuel leaks (due to the higher volatility of hydrogen), the broader explosive limit and the much lower minimum energy of ignition, the test cell is classified as Zone 3.

5.2 Control cabin

The control cabin does not contain any explosive material, and thus zoning is not required.

6 Explosion Risk Assessment

For the explosion risk assessment, the test cell is divided into three parts: the fuel tank, the engine and the other equipment.

6.1 Fuel Tank

The fuel tank is connected to the engine with a fuel line, and contains Avgas.

6.2 Engine

The engine is the main part of the test set-up. It is most prone to risk.

6.3 Other Equipment

7 Measures Taken

References

[1] Phillips 66 Company. *Aviation Gasoline, 100LL: Safety Data Sheet*. 2018.

[2] C. Harper and J.J. Liccione. *Toxicological Profile for Gasoline*. Tech. rep. U.S. Department of Health and Human Services, 1995.

[3] Linde Inc. *Hydrogen, Compressed: Safety Data Sheet*. 2020.

[4] Explosions Solutions. *Minimum Ignition Energy*. Retrieved 29-10-2020 from http://explosionsolutions.co.uk/110411020.pdf.

B
ADDITIONAL SENSITIVITY ANALYSIS RESULTS

In this appendix, the results of the sensitivity analysis not presented in Chapter 7 are given. This specifically applies to the results of the heat transfer parameters, which are omitted in Section 7.4. For each parameter, the P-V diagram, temperature profile and change in power, peak pressure and peak temperature is given.

B.1. HEAT TRANSFER PARAMETER *a*

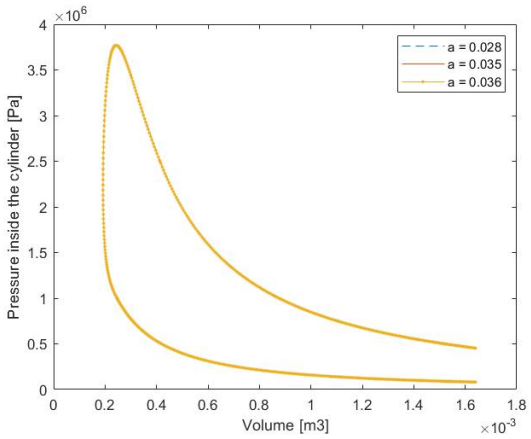

Figure B.1: P-V diagram with varying heat transfer parameter *a*.

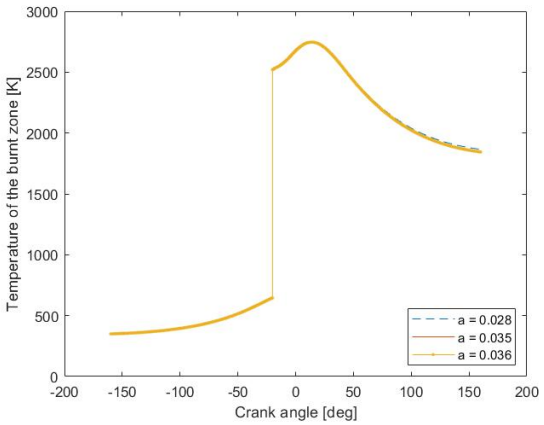

Figure B.2: Burnt zone temperature profile with varying heat transfer parameter *a*.

Table B.1: Change in power, peak pressure and peak temperature when varying heat transfer parameter *a*.

	Power	**Peak pressure**	**Peak temperature**
-100%	2.95%*	0.64%*	0.47%*
+100%	-2.70%*	-0.82%*	-0.38%*

B.2. HEAT TRANSFER PARAMETER *c*

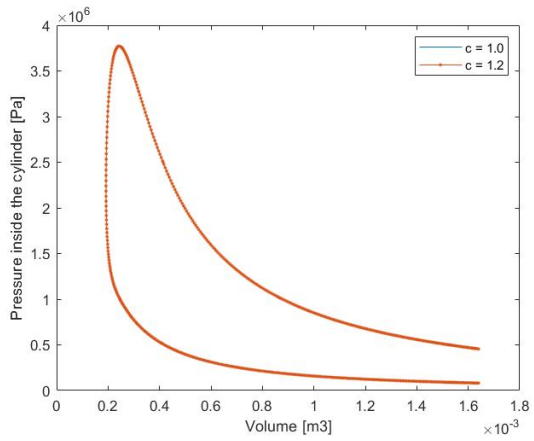

Figure B.3: P-V diagram with varying heat transfer parameter *c*.

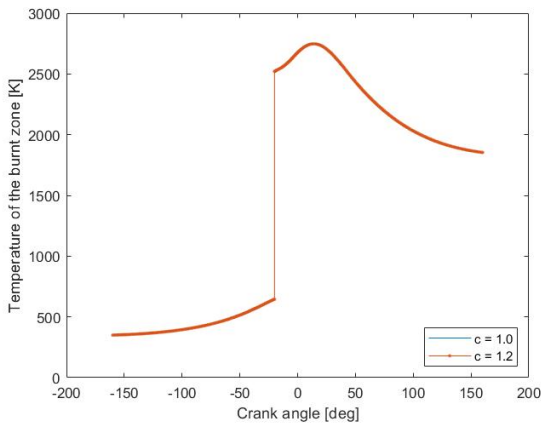

Figure B.4: Burnt zone temperature profile with varying heat transfer parameter *c*.

Table B.2: Change in power, peak pressure and peak temperature when varying heat transfer parameter *c*.

	Power	Peak pressure	Peak temperature
+100%	1.04%*	0.21%*	0.16%*

B.3. WOSCHNI PARAMETER *C*11

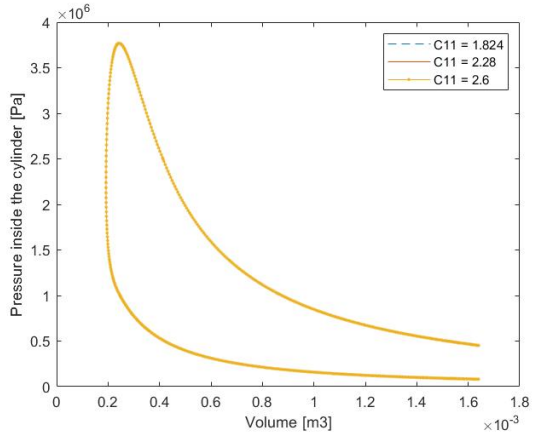

Figure B.5: P-V diagram with varying Woschni parameter *C*11.

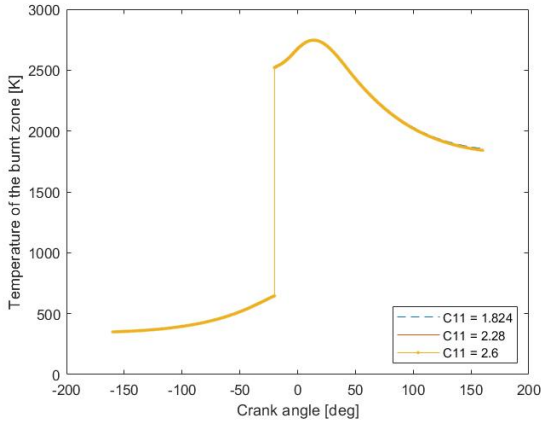

Figure B.6: Burnt zone temperature profile with varying Woschni parameter *C*11.

Table B.3: Change in power, peak pressure and peak temperature when varying Woschni parameter *C*11.

	Power	Peak pressure	Peak temperature
-100%	1.17%*	0.20%*	0.18%*
+100%	-1.05%*	-0.25%*	-0.16%*

B.4. WOSCHNI PARAMETER $C12$

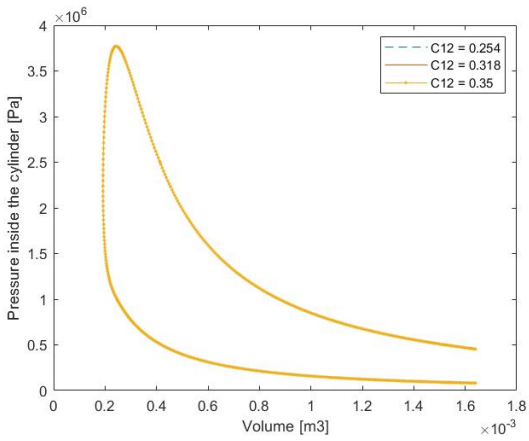

Figure B.7: P-V diagram with varying Woschni parameter $C12$.

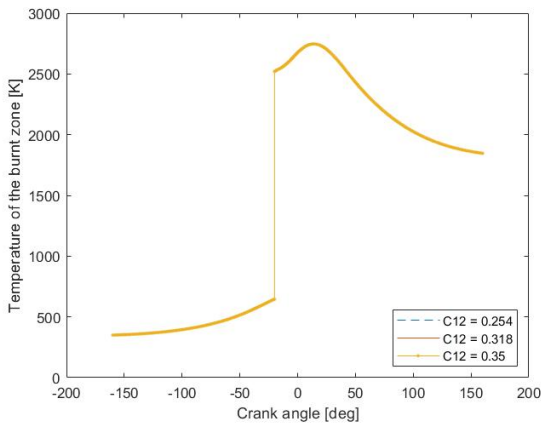

Figure B.8: Burnt zone temperature profile with varying Woschni parameter $C12$.

Table B.4: Change in power, peak pressure and peak temperature when varying Woschni parameter $C12$.

	Power	**Peak pressure**	**Peak temperature**
-100%	0.07%*	-0.02%*	0.02%*
+100%	0.03%*	-0.05%*	0.00%*

B.5. WOSCHNI PARAMETER $C2$

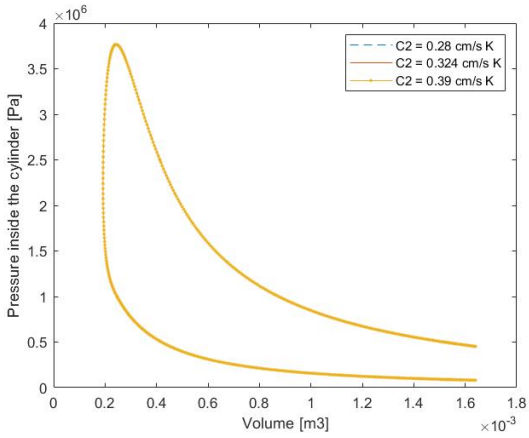

Figure B.9: P-V diagram with varying Woschni parameter $C2$.

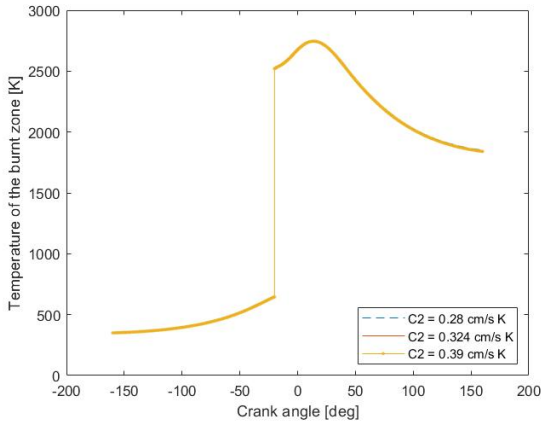

Figure B.10: Burnt zone temperature profile with varying Woschni parameter $C2$.

Table B.5: Change in power, peak pressure and peak temperature when varying Woschni parameter $C2$.

	Power	**Peak pressure**	**Peak temperature**
-100%	1.23%*	0.27%*	0.21%*
+100%	-1.12%*	-0.32%*	-0.18%*

B.6. SWIRL VELOCITY

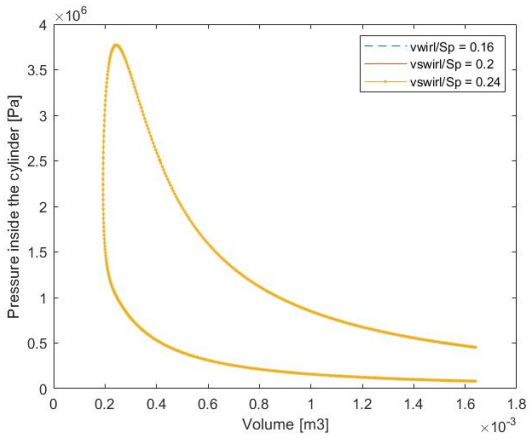

Figure B.11: P-V diagram with varying swirl velocity to piston velocity ratio.

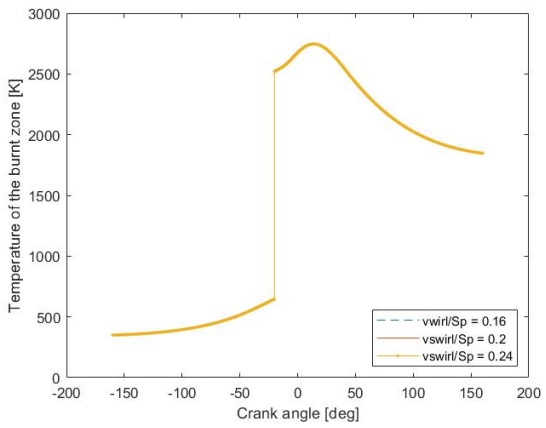

Figure B.12: Burnt zone temperature profile with varying swirl velocity to piston velocity ratio.

Table B.6: Change in power, peak pressure and peak temperature when varying the swirl velocity to piston velocity ratio.

	Power	Peak pressure	Peak temperature
-100%	0.07%*	-0.02%*	0.02%*
+100%	0.00%*	-0.03%*	0.00%*

B.7. WALL TEMPERATURE

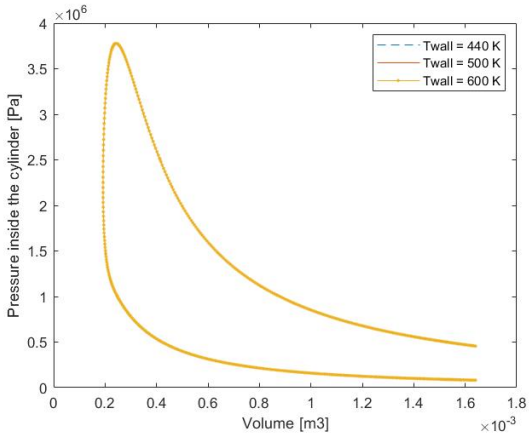

Figure B.13: P-V diagram with varying wall temperature.

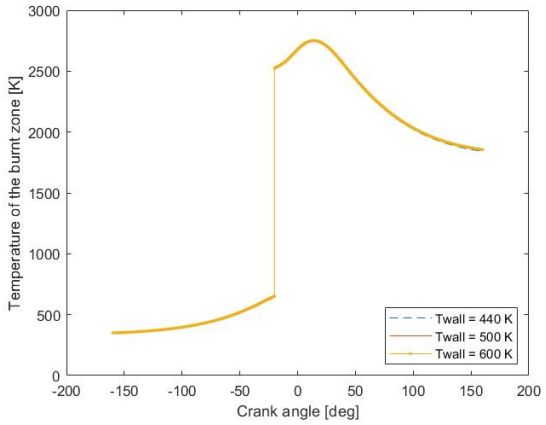

Figure B.14: Burnt zone temperature profile with varying wall temperature.

Table B.7: Change in power, peak pressure and peak temperature when varying the wall temperature.

	Power	Peak pressure	Peak temperature
-100%	-0.78%*	-1.15%*	-0.64%*
+100%	0.98%*	1.09%*	0.66%*